

Lehrstuhl für Computerunterstützte Klinische Medizin  
der Medizinischen Fakultät Mannheim, Universität Heidelberg  
Direktor: Prof. Dr. rer. nat. Lothar R. Schad

# **Simulation and development of RF resonators for preclinical and clinical $^1\text{H}$ and X-nuclei MRI**

Inauguraldissertation  
zur Erlangung des Doctor scientiarum humanarum (Dr. sc. hum.)  
der  
Medizinischen Fakultät Mannheim  
der Ruprecht-Karls-Universität  
zu  
Heidelberg

vorgelegt von  
Matthias Malzacher

aus  
Karlsruhe

2018



Dean: Prof. Dr. med. Sergij Goerd  
Supervisor: Prof. Dr. Lothar R. Schad



## **Simulation and development of RF resonators for preclinical and clinical $^1\text{H}$ and X-nuclei MRI**

Magnetic resonance imaging (MRI) is a unique imaging modality since it provides high soft tissue contrast without ionizing radiation. MRI hardware technology has evolved towards high channel receive (Rx) systems and highly efficient and homogeneous transmit (Tx) coils both increasing image quality and reducing measurement time. Radio frequency (RF) systems for MRI are designed to provide highest signal-to-noise ratio (SNR) while keeping the specific absorption rate (SAR) as low as possible. Due to the complexity of today's RF systems for MRI there are still some unsolved issues, such as preamplifier coupled noise, double resonant clinical coil performance and SAR simulation accuracy. This thesis consists of three main parts: First, the improvement of the SNR of Rx systems by evaluating new matching strategies; second, the development of RF setups for clinical sodium MRI applications; and third, the evaluation of the accuracy of SAR calculations and electromagnetic (EM) simulations. In the first part a transmit-only receive-only (ToRo) coil setup was built for  $^{35}\text{Cl}$  MRI at 9.4 T. The effect of SNR degradation due to coil coupling was verified for the Rx array consisting of three Rx coils. A 15 -17% SNR improvement could be achieved using different matching methods compared to the conventional matching strategy. The combined SNR of the Rx array was up to 4.5 higher compared to the reference SNR image acquired with the volumetric Tx coil. In the second part, two different double resonant RF setups for clinical sodium and proton MRI of the abdomen and the head were realized. A 16 channel abdominal sodium Rx array was simulated and built to be used with an asymmetric whole-body sodium coil. The setup was additionally equipped with a local proton transceiver coil. Sodium SNR was improved about a factor 3 to 6 in phantom measurements compared to the volume coil. The feasibility of the double resonant setup was proven by an *in-vivo* sodium and proton scan. The head RF setup comprised 8 sodium and 8 proton Rx coils. The findings from the  $^{35}\text{Cl}$  setup for the avoidance of SNR degradation due to coupled coils were also applied for this setup. The performance of the coil was compared to commercial sodium and proton setups using phantom measurements. Comparable SNR results to the commercial options were achieved in sodium measurements (Rx array/commercial = 1.14) and comparable SNR (Rx array/commercial = 1.09) as well as parallel imaging performance (Rx array/commercial: mean g-factor = -7% to +6%; maximum g-factor = -21% to 33%) in proton measurements. Finally, the feasibility of the coil was proven by *in-vivo* sodium and proton measurements. In the third part, the impact of Rx arrays on SAR calculations was evaluated by modeling a clinical setup at 3T and a research setup at 7T. The clinical setup comprised a large Birdcage Tx coil and different Rx arrays tailored for the head (24 elements), the abdomen (36 elements) and the spine (32 elements). The research setup consisted of a head Birdcage coil and a 32 element Rx array. SAR simulations were performed with and without the Rx arrays. Mean SAR differences were found to be between -4% and 2% for the 3T setup and up to 11% for the 7T setup. Maximum SAR differences were found to be between -10% and +6% for the 3T setup and up to -8% for the 7T setup. As a last step, the accuracy and performance of the two most common approaches for solving EM fields for MR RF setups were evaluated. Therefore a whole-body Birdcage coil at 3T, a head Birdcage coil at 7T and an 8 channel Tx array at 9.4T, 10.5T and 11.7T were modeled. Each setup was simulated using the time domain (TD) and the frequency domain (FD) method. Finally, the resulting S-parameter, B-fields and SAR were compared. A difference below 20% was achieved for all these results which was already reported in earlier studies of a single specialized setup. The FD solver was found to be up to 12 times faster than the TD solver.



## Simulation und Entwicklung von HF Resonatoren für die präklinische und klinische $^1\text{H}$ und X-Kern MRT

Die Magnetresonanztomographie (MRT) ist eine einzigartige Bildgebungsmethode, da sie einen hohen Weichteilkontrast ohne ionisierende Strahlung bietet. Die MRT Hardwaretechnologie hat sich in Richtung Hochkanal Empfangssysteme (Rx) als auch hocheffiziente und homogene Übertragungsspulen (Tx) entwickelt, die sowohl die Bildqualität erhöhen als auch die Messzeit verkürzen. Hochfrequenzsysteme (HF) für die MRT sind so konzipiert, dass sie das höchste Signal-Rausch-Verhältnis (SNR) bieten und gleichzeitig die spezifische Absorptionsrate (SAR) so niedrig wie möglich halten. Aufgrund der Komplexität der heutigen HF Systeme für die MRT gibt es noch einige ungelöste Probleme, wie z.B. vorverstärkergekoppeltes Rauschen, Performanz von doppelresonanten klinischen Spulen und SAR Simulationengenauigkeit. Diese Arbeit besteht aus drei Hauptteilen: Erstens die Verbesserung des SNR von Rx Systemen durch Evaluierung neuer Anpassungsstrategien, zweitens die Entwicklung von HF Setups für klinische Natrium MRT Anwendungen und drittens die Evaluierung der Genauigkeit von SAR Berechnungen und elektromagnetischen (EM) Simulationen. Im ersten Teil wurde eine Transmit-only Receive-only (ToRo) Setup für  $^{35}\text{Cl}$ -MRT bei 9,4 T gebaut. Der Effekt der SNR-Degradation durch Spulenkopplung wurde für das aus drei Rx Spulen bestehende Rx Array verifiziert. Eine Verbesserung des SNR um 15 -17% konnte mit verschiedenen Anpassungsmethoden im Vergleich zur herkömmlichen Anpassungsstrategie erreicht werden. Das kombinierte SNR des Rx Arrays war bis zu 4,5 höher als das mit der volumetrischen Tx-Spule aufgenommene Referenz SNR Bild. Im zweiten Teil wurden zwei verschiedene doppelresonante HF Setups für die klinische Natrium- und Protonen MRT des Abdomens und des Kopfes realisiert. Ein 16-Kanal Abdomen Natrium Rx Array wurde simuliert und für den Einsatz mit einer asymmetrischen Ganzkörper Natriumspule gebaut. Der Aufbau wurde zusätzlich mit einer lokalen Protonen Sende-Empfangsspule ausgestattet. Natrium SNR wurde bei Phantommessungen um den Faktor 3 bis 6 gegenüber der Volumenspule verbessert. Die Machbarkeit des doppelresonanten Setups wurde durch einen *in-vivo* Natrium- und Protonenscan nachgewiesen. Das Kopf HF Setup bestand aus 8 Natrium und 8 Proton Rx Spulen. Die Erkenntnisse aus dem  $^{35}\text{Cl}$  Setup zur Vermeidung von SNR Degeneration durch gekoppelte Spulen wurden auch für dieses Setup genutzt. Die Leistung der Spule wurde mit handelsüblichen Natrium- und Protonenaufsetups mittels Phantommessungen verglichen. Vergleichbare SNR Ergebnisse zu den kommerziellen Optionen wurden bei Natrium Messungen (SNR Rx array/commercial = 1,14) und vergleichbares SNR (SNR Rx array/commercial = 1,09) sowie parallele Bildgebungsleistung (Rx array/commercial: mean g-factor = -7% bis +6%) bei Protonenmessungen erzielt. Schließlich wurde die Machbarkeit der Spule durch *in-vivo* Natrium- und Protonenmessungen nachgewiesen. Im dritten Teil wurde der Einfluss von Rx Arrays auf SAR Berechnungen durch die Modellierung eines klinischen Setups bei 3T und eines Forschungssetups bei 7T bewertet. Das klinische Setup umfasste eine große Birdcage Tx Spule und verschiedene Rx Arrays, die auf den Kopf (24 Elemente), den Bauch (36 Elemente) und die Wirbelsäule (32 Elemente) zugeschnitten waren. Das Forschungssetup bestand aus einer Kopf Birdcage Spule und einem 32-Element Rx Array. SAR-Simulationen wurden mit und ohne Rx Arrays durchgeführt. Die durchschnittlichen SAR Unterschiede lagen zwischen -4% und 2% für das 3T Setup und bis zu 11% für das 7T Setup. Die maximalen SAR Unterschiede lagen zwischen -10% und +6% für das 3T Setup und bis zu -8% für das 7T Setup. In einem letzten Schritt wurden die Genauigkeit und Leistungsfähigkeit der beiden gängigsten Ansätze zur Lösung von EM Feldern für MR HF Setups evaluiert. Dazu wurden eine Ganzkörper Birdcage Spule bei 3T, eine Kopf Birdcage Spule bei 7T und ein 8-Kanal Tx Array bei 9,4T, 10,5T und 11,7T modelliert. Jedes Setup wurde mit der Zeitbereich (TD) und dem Frequenzbereich (FD) Methode simuliert. Schließlich wurden die resultierenden S-Parameter, B-Felder und SAR verglichen. Bei all diesen Ergebnissen wurde eine Differenz von weniger als 20% erreicht. So eine Abweichung wurde bereits in einer früheren Studie eines einzigen spezialisierten Setups berichtet. Der FD-Solver war bis zu 12 mal schneller als der TD-Solver.





# Contents

---

<b>1</b>	<b>Introduction and outline</b>	<b>1</b>
1.1	Introduction . . . . .	1
1.2	Outline . . . . .	3
1.3	Citation of previous publications . . . . .	4
<b>2</b>	<b>Background</b>	<b>5</b>
2.1	MRI physics . . . . .	5
2.2	RF background . . . . .	7
2.3	EM simulation background . . . . .	20
2.4	X-nuclei background . . . . .	25
<b>3</b>	<b>“Reducing signal-to-noise ratio degradation due to coil coupling in a receiver array for <sup>35</sup>Cl MRI at 9.4 Tesla: A comparison of matching and decoupling strategies” <i>Concept Magn Reson B, DOI: 10.1002/cmr.b.21383</i></b>	<b>29</b>
3.1	Introduction . . . . .	29
3.2	Material and methods . . . . .	30
3.3	Results . . . . .	35
3.4	Discussion . . . . .	36
3.5	Statement of contribution . . . . .	39
<b>4</b>	<b>“Feasibility study of a double resonant (<sup>1</sup>H/<sup>23</sup>Na) abdominal RF setup at 3T” <i>Z Med Phys, submitted (06.08.2018)</i></b>	<b>41</b>
4.1	Introduction . . . . .	41
4.2	Material and methods . . . . .	42
4.3	Results . . . . .	47
4.4	Discussion . . . . .	48
4.5	Conclusion . . . . .	50
4.6	Statement of contribution . . . . .	50
<b>5</b>	<b>“Feasibility study of a double resonant <sup>1</sup>H/<sup>23</sup>Na 16-channel receive-only head coil at 3T” <i>Magn Reson Imaging, submitted (20.08.2018)</i></b>	<b>51</b>
5.1	Introduction . . . . .	51
5.2	Material and methods . . . . .	52
5.3	Results . . . . .	55
5.4	Discussion and conclusion . . . . .	56
5.5	Statement of contribution . . . . .	59

<b>6</b>	<b>“Evaluating the effects of receive-only arrays in specific absorption rate simulations at 3 and 7 T” <i>Magn Reson Imaging, DOI: 10.1016/j.mri.2018.06.011</i></b>	<b>61</b>
6.1	Introduction . . . . .	61
6.2	Methods . . . . .	62
6.3	Results . . . . .	66
6.4	Discussion . . . . .	70
6.5	Statement of contribution . . . . .	72
<b>7</b>	<b>“A comparison of Time Domain and Frequency Domain methods for the simulation of RF systems for MRI applications at 3 to 11.7 T” <i>PLOS ONE, submitted (25.07.2018)</i></b>	<b>73</b>
7.1	Introduction . . . . .	73
7.2	Background . . . . .	74
7.3	Material and methods . . . . .	76
7.4	Results . . . . .	79
7.5	Discussion . . . . .	80
7.6	Conclusion . . . . .	83
7.7	Statement of contribution . . . . .	84
<b>8</b>	<b>Summary</b>	<b>85</b>
<b>9</b>	<b>Outlook</b>	<b>91</b>
	<b>Bibliography</b>	<b>95</b>
	<b>Publications</b>	<b>103</b>
	<b>Curriculum Vitae</b>	<b>107</b>
	<b>Acknowledgements</b>	<b>109</b>





## 1.1 Introduction

Magnetic resonance imaging (MRI) is an indispensable diagnostic tool in the clinical practice. Since it was proposed by Lauterbur and Mansfield in 1973 it gained significance in the clinical diagnostic and is one of the leading imaging modalities.

Contrary to Computed Tomography or Proton Emission Tomography, MRI provides tomographic *in-vivo* images without ionizing radiation. MRI is based on the interaction of nuclear spins within the subject of investigation with electromagnetic (EM) fields. A typical MR experiment starts with the excitation of the nuclei using an externally applied radio frequency (RF) field. After the excitation the nuclei precess while relaxing back to their equilibrium state. During this mechanism tissue characteristic RF signals are emitted by the nuclei. The RF fields are generated and detected by near-field antennas which are commonly called coils. In addition to improvements of imaging sequences and post-processing the development of optimized hardware enormously improved the imaging quality in recent years.

Today's clinical MR scanners are equipped with up to 8 transmit (Tx) channels and up to 128 receive (Rx) channels. State of the art systems usually comprise a volumetric transmit coil, which encircles the object of investigation, in order to produce a homogeneous Tx field for excitation. Signal reception is commonly achieved by a combination of multiple Rx coils, referred to as arrays, which are placed in the immediate vicinity of the volume of interest. This is done to increase the signal-to-noise ratio (SNR) of the signal. These Rx arrays are tailored for each part of the body, for example head coils, spine coils, knee coils and so forth. The combination of separate Tx and Rx coils is called transmit-only receive-only (ToRo) (Barberi et al., 2000).

The most commonly utilized nucleus in clinical applications is the  $^1\text{H}$ -proton nucleus due to the vast abundance in the human body and its beneficial spin properties. However, other nuclei such as  $^{23}\text{Na}$ -sodium or  $^{35}\text{Cl}$ -chlorine, which are also called X-nuclei, can provide valuable additional diagnostic information about tissue viability and vitality (Schepkin et al., 2006, 2005). Their resonance frequencies, determined by their intrinsic gyromagnetic ratio and the external static magnetic field, are always lower than the proton resonance frequency.

Due to this difference in resonance frequencies the hardware setup for excitation and reception has to be adapted individually to each nucleus. X-nuclei hardware designs are comparable to common proton designs (Brown et al., 2016a; Malzacher et al., 2016a; Shajan et al., 2016). However, the low frequency and the low *in-vivo* MR sensitivity (sodium  $\approx 10\,000$  times lower than proton and chlorine  $\approx 20$  times lower than sodium (Baier et al., 2014)) poses special requirements and additional challenges for the design of the respective coils.

Noise sources are the MR coil itself and the sample of investigation. In contrast to most proton applications, noise in most X-nuclei applications is coil dominated. However, proton coils, which are not placed in the immediate vicinity of the sample due to the hardware design, e.g. the upper coils of head/knee arrays or remote body arrays (Sodickson et al., 2014), are also coil noise dominated. In this case coupling between Rx coils can decrease SNR. Whereas adjacent coils can be directly decoupled using the coil geometry non-adjacent coils are commonly decoupled using preamplifier decoupling (Roemer et al., 1990). Nevertheless, recent studies (Brown et al., 2016a; Malzacher et al., 2018, 2016b; Vester et al., 2012) have shown that in the case of low loaded coils SNR is decreased despite preamplifier decoupling. This effect is called preamplifier noise coupling.

The first aim of this thesis was to investigate the effect of preamplifier noise coupling and to evaluate methods, which mitigate this effect. This was done by developing a ToRo setup for  $^{35}\text{Cl}$  MRI at 9.4 T. In a next step these findings were used to develop optimized coil setups suitable for both sodium and proton MRI of the abdomen and the head at a clinical 3T scanner. For the head application special focus was on providing high sodium sensitivity while preserving full proton performance.

In addition to coil sensitivity optimization the safety assessment of the RF hardware setup is of major importance. The Tx coil deposits energy within the body during the transmit pulse, which causes heating and can be dangerous for the patient. The regulation limits for the transmission energy are expressed in the specific absorption rate (SAR). SAR is commonly determined for each Tx setup using electro-magnetic (EM) simulations. This safety assessment has to be performed by vendors as well as researches in order to get the approval for *in-vivo* measurements and is crucial to patient safety.

EM simulations for SAR calculations aim for a representation of the measurement setup as detailed as possible. This has been realized in numerous studies by improving the human body models and the solver methods. Especially a good knowledge of the utilized solver method and appropriate adjustments of it is important to obtain accurate and fast results. In recent years mainly two methods have been used for the EM simulations of coil setups. These are the Frequency Domain (FD) and the Time Domain (TD) method. Both methods have advantages and disadvantages regarding the coil setup and the frequency of interest.

Despite the research, which has been performed to provide as much detail as possible, the impact of Rx arrays on the SAR simulation has hardly ever been taken into account.

Thus, the second aim of this work was to investigate the impact of Rx arrays on SAR simulations. Therefore various clinical setups and one research setup were modeled for simulation evaluating the impact of the Rx arrays by performing simulations with

and without the Rx arrays. Additionally, the FD and the TD method were compared by modeling in different setups, at different field strengths and by comparing the resulting EM fields and the solver performance.

## 1.2 Outline

This work is written cumulatively. Every Chapter from 3 to 7 is a self-contained scientific study. Each of these studies comprises an introduction to the topic, a description of the material and methods, the presentation of the results and a discussion. Additionally at the end of each of these chapters a statement of contribution is given.

Chapter 2 aims to provide a short physical background to the technique of MRI and the basic processes. An introduction to MR coils and RF systems is given as well as the fundamental mathematical description used for EM simulations. Finally, a brief introduction to X-nuclei MRI is provided.

In chapter 3, different matching and decoupling approaches, which mitigate SNR degradation arising from coil coupling, are compared. A complete RF setup consisting of a Birdcage transmit coil and a 3 channel Rx array for  $^{35}\text{Cl}$  MRI at 9.4T was built. The array coils were measured using preamplifier decoupling, transformer decoupling, broadband matching and mode matching. These approaches are compared in terms of their ability to recover lost SNR due to coil coupling.

In chapter 4, the feasibility of a double resonant  $^1\text{H}/^{23}\text{Na}$  RF setup for abdominal MRI at 3T is evaluated. The RF setup comprises a volumetric sodium transmit coil, a 16-channel sodium Rx array and a local proton transceiver coil. The setup was modeled for EM simulations and built for MRI measurements. Sensitivity increase (3 to 6 fold) of the array compared to the volumetric coil was found using phantom simulations and measurements. Safety assessment of the proton coil was performed using EM simulations. The feasibility of such a setup was finally proven with an *in-vivo* scan of a healthy volunteer.

Chapter 5 presents the feasibility evaluation of a double resonant ( $^1\text{H}/^{23}\text{Na}$ ) 16-channel Rx head coil at 3T. This work aims to provide good sodium performance while maintaining proton performance comparable to commercial coils without the need of coil exchange. The coil comprises an 8 channel sodium degenerate Birdcage and an 8 channel proton array, decoupled via overlap. The coil was designed using EM simulations and built for MRI measurements. The coil performance is compared with commercial setups using phantom measurements. Finally, *in-vivo* scans of a healthy volunteer were performed.

In chapter 6 the impact of Rx arrays on the simulated SAR distribution of different RF setups is investigated. A whole-body Tx coil for a clinical alike setup at 3 T and a head Tx coil for 7 T were modeled for EM simulations. Additionally, different Rx arrays (head, spine and abdomen) for 3 T and a head Rx array for 7 T were modeled. EM simulations were performed with and without the Rx arrays at 3 positions for the 3 T setup and one position at the 7 T setup. Finally, the SNR distributions are compared within these simulations and differences are discussed.

Chapter 7 aims to provide a comparison of the Frequency Domain and Time Domain approach to solve Maxwell's equation for RF setups in MRI applications. Different simulation setups were modeled for 3 T, 7 T, 9.4 T, 10.5 T and 11.7 T. The EM fields of these setups were simulated with the FD and TD method. The resulting fields, S-parameters and the solver performance are compared within these results and the advantages and disadvantages of the two approaches for different setups and field strengths are discussed.

Chapter 8 gives a total overview of the thesis as well as a detailed overview of the results of the scientific studies presented in chapters 3 through 7.

Chapter 9 provides an outlook on future research perspectives and the relevance of the presented work for RF engineers in the field of MRI.

### 1.3 Citation of previous publications

The chapter 3 to 7 of this thesis have been published elsewhere or are currently submitted for publication. The citations of these chapters are:

**Chapter 3:** M. Malzacher, R. Hu, J. Chacon-Caldera and L. Schad. Reducing signal-to-noise ratio degradation due to coil coupling in a receiver array for  $^{35}\text{Cl}$  MRI at 9.4 Tesla: A comparison of matching and decoupling strategies. *Concept Magn Reson B*, in press (2018)

**Chapter 4:** M. Malzacher, J. Chacon-Caldera, N. Paschke and L. Schad. Feasibility study of a double resonant ( $^1\text{H}/^{23}\text{Na}$ ) abdominal RF setup at 3T. *Z Med Phys*, submitted, Date of submission: 06.08.2018

**Chapter 5:** M. Malzacher, J. Chacon-Caldera, N. Paschke and L. Schad. Feasibility study of a double resonant  $^1\text{H}/^{23}\text{Na}$  16-channel receive-only head coil at 3T. *Magn Reson Imaging*, submitted, Date of submission: 20.08.2018

**Chapter 6:** M. Malzacher, M. Davids, L. R. Schad, and J. Chacon-Caldera. Evaluating the effects of receive-only arrays in specific absorption rate simulations at 3 and 7 T. *Magn Reson Imaging*, 53, p. 7-13 (2018)

**Chapter 7:** M. Malzacher, J. Chacon-Caldera and L. Schad. A comparison of Time Domain and Frequency Domain methods for the simulation of RF systems for MRI applications at 3 to 11.7 T. *PLOS ONE*, submitted, Date of submission: 25.07.2018



## 2.1 MRI physics

The basis of magnetic resonance is the nuclear spin. The spin is the intrinsic angular momentum  $\vec{S}$  of elementary particles. This momentum is associated with the magnetic momentum  $\vec{\mu}$  by

$$\vec{\mu} = \gamma \vec{S} \quad (2.1)$$

with  $\gamma$  the gyromagnetic ratio which is characteristic for each nucleus. By applying a static magnetic field  $B_0$  the energy ground states of a nucleus split into  $(2S + 1)$  energy levels  $E_m$

$$E_m = -\gamma \hbar m B_0 \quad (2.2)$$

with  $m$  the quantum number and  $\hbar$  the reduced Planck constant.

The most often utilized nucleus in the clinical practice is the proton ( $^1H$ ) nucleus which has a spin  $S = \frac{1}{2}$ . Therefore two energy levels  $E_{+\frac{1}{2}}$  ( $m = +\frac{1}{2}$ ) and  $E_{-\frac{1}{2}}$  ( $m = -\frac{1}{2}$ ) arise in presence of a static magnetic field. This means the nuclei either align parallel or anti-parallel with the  $B_0$ . The energy difference  $\Delta E$  between these two states is given by

$$\Delta E = E_{-\frac{1}{2}} - E_{+\frac{1}{2}} = \gamma \hbar m B_0 = \hbar \omega_0 \quad (2.3)$$

Depending on the spin of the nucleus more energy levels are possible, e.g. four energy levels for sodium ( $^{23}Na$ )  $S = \frac{3}{2}$ .

The Larmor frequency  $\omega_0$

$$\omega_0 = \gamma B_0 \quad (2.4)$$

is proportional to the energy difference.

The distribution ratio in the thermal equilibrium is given by the Boltzmann equation

$$\frac{N_{upper}}{N_{lower}} = e^{\frac{-\Delta E}{kT}} \quad (2.5)$$

with  $N_{upper}$  the quantity of nuclei in the higher and  $N_{lower}$  the quantity of nuclei in the lower energy state,  $k$  the Boltzmann constant and  $T$  the absolute temperature in Kelvin. This ratio is very low (about 0.999998 for protons at 3T).

Since most physical samples consist of many atoms a macroscopic magnetization  $\vec{M}$  can be introduced

$$\vec{M} = \frac{1}{V} \sum_i \vec{\mu}_i \quad (2.6)$$

with  $\mu_i$  the individual magnetic moments within the volume  $V$ . The net magnetization can be calculated using the Boltzman statistics

$$M_0 = \frac{N \gamma^2 \hbar^2 S(S+1) B_0}{3kT} \quad (2.7)$$

with  $N$  the number of magnetic moments within the volume  $V$ . This means the magnetization is proportional to the gyromagnetic ratio and the field strength. As all other nuclei than proton have a lower magnetic ratio moving to higher field strengths can compensate the loss in magnetization to a certain extent for these other nuclei.

The behavior of the net magnetization can be expressed as

$$\frac{d}{dt} \vec{M}(t) = \gamma \vec{M}(t) \times \vec{B}_0 \quad (2.8)$$

by assuming that the spins do not interact with the environment. This equation describes the precession of the magnetization around the magnetic field.

A transverse magnetization can be created by applying an external RF field  $B_1$  perpendicular to the static field  $B_0$  with

$$\vec{B}_1(t) = B_1 \begin{pmatrix} \cos(\omega_1 t) \\ \sin(\omega_1 t) \\ 0 \end{pmatrix} \quad (2.9)$$

The motion of the macroscopic magnetization can best be described by assuming a particular frame of reference.. This reference frame is rotating around the direction of the static field  $B_0$  with the Larmor frequency (equation 2.4). Additionally the magnetic fields  $\vec{B}_0$  and  $\vec{B}_1$  can be combined to an effective field  $B_{eff}$ . Then the motion can be described as

$$\frac{d}{dt} \vec{M}'(t) = \gamma \vec{M}'(t) \times \begin{pmatrix} B_1 \\ 0 \\ B_0 - \frac{\omega_1}{\gamma} \end{pmatrix} = \gamma \vec{M}'(t) \times B_{eff} \quad (2.10)$$

If the frequency of the RF pulse is corresponding to the Larmor frequency the resulting effective field is  $\vec{B}_{eff} = (B_1, 0, 0)$ . This field causes a rotation of the magnetization away from the direction of the static field. The nutation angle by which the magnetization is flipped is depending on the magnitude of the field  $B_1$  and the duration  $\tau$  of the pulse. The flip angle  $\alpha$  is calculated by

$$\alpha = \int_0^\tau B_1(t) dt \quad (2.11)$$

After the pulse is switched off the precessing magnetization in the transversal plane can be measured by a so called coil by determining the voltage which is induced into the coil. A detailed description of MR coils is given in paragraph 2.2.

The precession of the magnetization back to its equilibrium state can be described by the Bloch equations

$$\frac{d}{dt}M_x = \gamma(\vec{M}(t) \times \vec{B}(t))_x - \frac{M_x(t)}{T_2} \quad (2.12)$$

$$\frac{d}{dt}M_y = \gamma(\vec{M}(t) \times \vec{B}(t))_y - \frac{M_y(t)}{T_2} \quad (2.13)$$

$$\frac{d}{dt}M_z = \gamma(\vec{M}(t) \times \vec{B}(t))_z - \frac{M_z(t) - M_0}{T_1} \quad (2.14)$$

with  $T_1$  the longitudinal relaxation time and  $T_2$  the transversal relaxation time.

The solution of equation 2.14 can be expressed as

$$M_z(t) = M_{z,0} - (M_{z,0} - M_z(0))e^{-\frac{t}{T_1}} \quad (2.15)$$

The time constant  $T_1$  characterizes the rate by which the magnetization component parallel to the static field  $B_0$  reaches the thermodynamic equilibrium.

The solution of equation 2.12 and 2.13 with the initial value  $M_{x,y}(0)$  can be expressed as

$$M_{x,y}(t) = M_{x,y}(0)e^{-\frac{t}{T_2}} \quad (2.16)$$

The time constant  $T_2$  describes the decay of the macroscopic magnetization in the plane perpendicular to the static field  $B_0$ .

## 2.2 RF background

### 2.2.1 MR system overview

The MR system is composed of many hardware elements. In order to have a short overview the main components of an MR scanner are depicted in Figure 2.1. First of all the complete system is surrounded by an electromagnetic compatibility (EMC) chamber (Figure 2.1, 1). This is done because the resonance frequency of  $^1\text{H}$  at 3T is in the same frequency band as the national broadcast. The EMC chamber protects the MR signal from the broadcast signal and it cancels also any interaction of the MR transmit signal with the broadcast antennas.

The outer layer of the scanner is a cryo-cooled superconductor (Figure 2.1, 2). This superconductor is realized as a solenoid. Current in this superconductor generates the main static field  $B_0$ .

The next layer contains the gradient coils (Figure 2.1, 3). These coils superimpose a spatially varying magnetic field to the static field for spatial encoding. These coils are usually switched with frequencies in the kHz range.

The last layer which is covered by the bore cover is the body coil (Figure 2.1, 4). Commonly, in state of the art clinical MRI systems this is a large volumetric coil which produces a homogeneous transmit  $B_1^+$ -field.

The local coils (Figure 2.1, 5) are placed in the immediate vicinity of the patient. These coils are usually realized as array coils. Such arrays are composed of many individual single coils. The local coils receive the weak MR signal. Depending on the region of interest the local coils are shaped to the given anatomical properties, e.g. head coils, knee coils, flexible coils, spine coils and so forth.

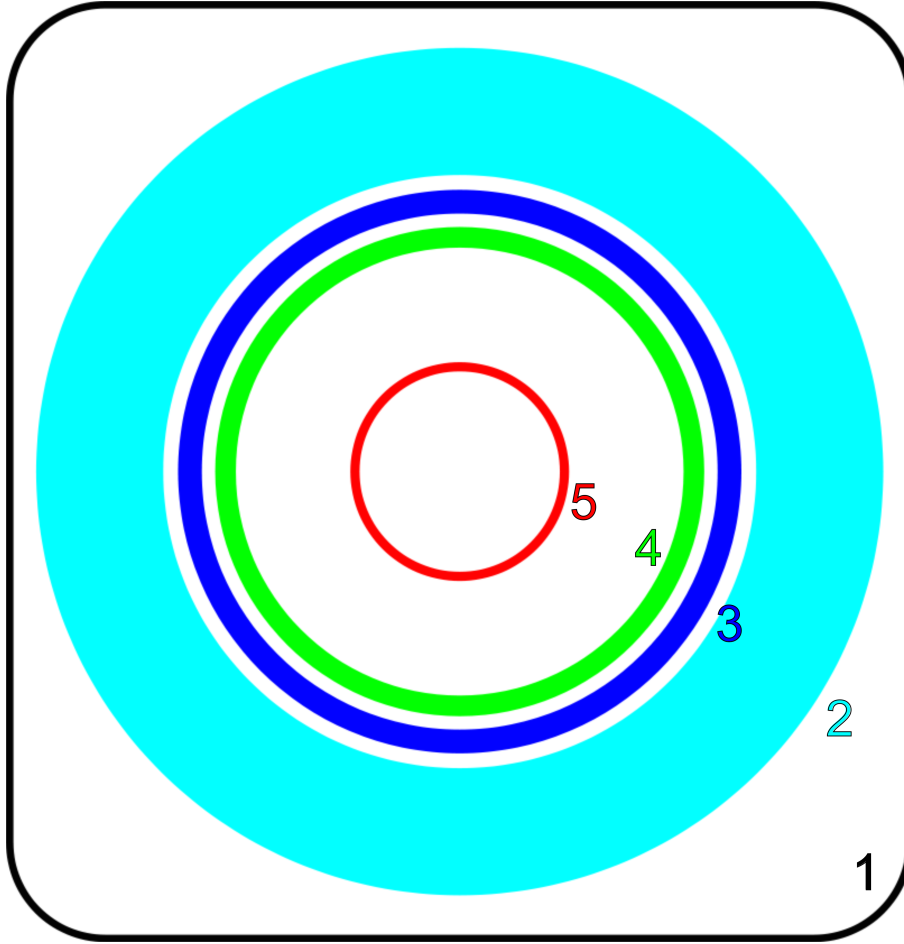


**Figure 2.1:** Basic overview of the hardware components of a clinical MR system.

## 2.2.2 MR coils and coil systems

### 2.2.2.1 RF coil

The RF coil is a near-field antenna sensitive to the magnetic field. The purpose of these coils is to generate an oscillating magnetic field (transmit field  $B_1^+$ ). In the same way the coil detects the induced electromagnetic force by the precessing sample magnetization using the law of reciprocity (receive field  $B_1^-$ ). These two components of the  $B_1$  field are counter rotating. The  $B_1^+$  component rotates along the precession of the magnetic moment and  $B_1^-$  rotates in the negative sense. Both components can be described as

$$\vec{B}_1^+ = \frac{(\vec{B}_x + i\vec{B}_y)}{2} \quad (2.17)$$

and

$$\vec{B}_1^- = \frac{(\vec{B}_x - i\vec{B}_y)^*}{2} \quad (2.18)$$

The magnetic field  $B$  can be calculated by Ampere's law

$$\oint B dl = \mu_0 \int J ds \quad (2.19)$$

with  $J$  the total current density.

The basic coil is made of an inductor and a capacitor resulting in a narrowband electrical resonant circuit. This circuit is tuned to the Larmor frequency of the nucleus of interest. This is done to maximize the sensitivity of the coil at this special frequency. The resonant frequency is determined by:

$$f_{res} = \frac{1}{2\pi\sqrt{LC}} \quad (2.20)$$

with  $L$  and  $C$  the equivalent inductance and capacitance of the coil.

The geometry, and therefore the inductance, of the coil is given by its purpose. In general, Tx coils are built as volumetric coils and Rx coils are built as surface coils adapted to the geometry of the object of interest.

The quality factor (Q-factor) of a coil is used as a figure of merit to characterize the performance of a coil. It can be expressed as:

$$Q = 2\pi f_{res} \frac{\text{energy stored}}{\text{power loss}} = \frac{\omega L}{R} \quad (2.21)$$

with  $R$  the total losses. Depending on the loading of the coil the sample losses or the coil losses are dominating. In order to determine which losses are dominating the  $Q_{ul}$  to  $Q_l$  ratio is calculated with  $Q_{ul}$  the Q-factor measured without the sample and  $Q_l$  the Q-factor measured with the sample. This ratio determines the impact of the sample:

$$\frac{Q_{ul}}{Q_l} = \frac{\frac{\omega L}{R_C}}{\frac{\omega L}{R_C + R_S}} = \frac{R_C + R_S}{R_C} \quad (2.22)$$

with  $R_C$  the coil losses and  $R_S$  the sample losses. As a consequence for  $\frac{Q_{ul}}{Q_l} \gg 1$  the sample losses are dominating and for  $\frac{Q_{ul}}{Q_l} = 1$  the coil losses are dominating. In the latter case decreasing the coil losses is crucial. In general, this is the case at very low frequencies or for very small coils.

In order to increase the coil's Q-factor the resistive losses can be decreased. These losses result from the coil conductor, capacitors, PIN diodes and solder joints. Common materials used as conductor are copper ( $\sigma = 59 \cdot 10^6$  S/m) or silver ( $\sigma = 63 \cdot 10^6$  S/m). The choice of conductive material is limited to non-magnetic ones. Additionally, the skin effect forces the current to the outer surface of the conductor which increases the effective resistance of the conductor. The skin depth  $\delta$  is calculated by

$$\delta = \sqrt{\frac{2}{\sigma\omega\mu}} \quad (2.23)$$

with  $\sigma$  the conductivity,  $\omega$  the angular frequency and  $\mu$  the product of the relative magnetic permeability of the conductor and the permeability of free space. As can be derived by this formula the skin depth is a larger problem at high frequencies.

There are different loss mechanisms which add noise to the coil and decrease the Q-factor. These are for example the conductor losses, the equivalent series resistance (ESR)

of the capacitors or in actively detunable coils the ESR of the PIN diodes.

Another effect which decreases the coil's Q-factor is the voltage distribution on the conductor. A simplified coil with one capacitor is depicted in Figure 2.2. Additionally, the voltage magnitude along the coil is given. It can be observed that the differences in voltage along the coil vary a lot. This unequal voltage distribution on the coil results in an inhomogeneous H-field as well as larger stray electric fields. This can be avoided by splitting the coil more often, e.g. in four parts (Figure 2.2). In this case the voltage is distributed more equally and the maximum voltage is a quarter compared to the coil with one capacitor. A rule of thumb is to keep the maximum conductor length at least below  $\frac{\lambda}{10}$ .

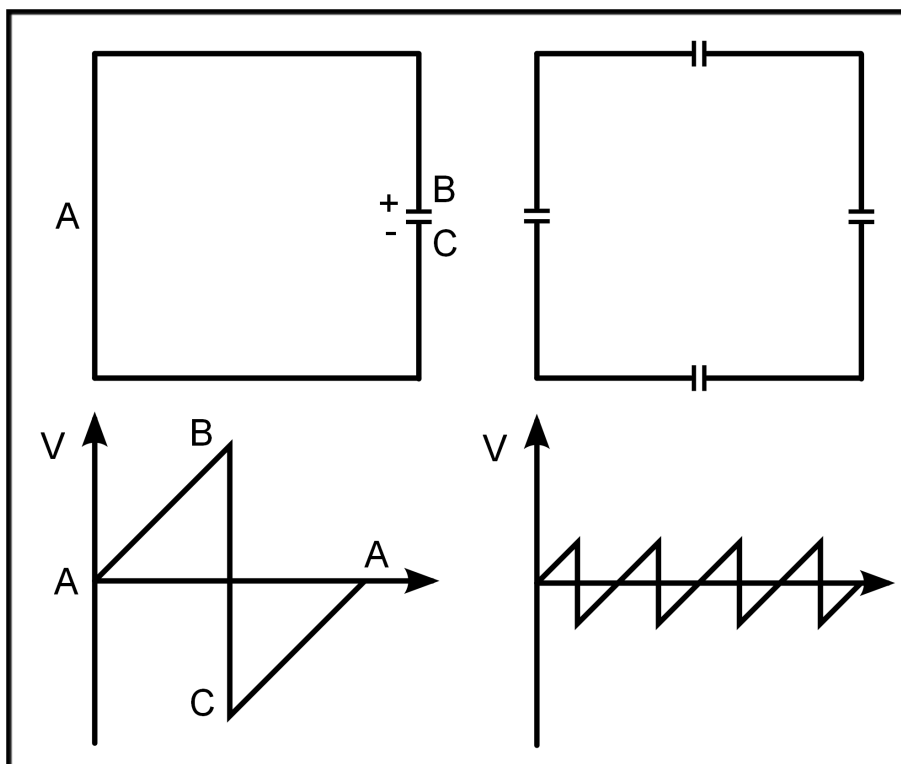


**Figure 2.2:** Simplified circuit diagram and the respective voltage distribution of a coil separated by one and by four capacitors.

### 2.2.2.2 Signal-to-noise ratio

The derivation of the SNR of an exemplary MR coil is mainly based on Schnell et al. (Schnell et al., 2000). Considering the MR coil as a series electrical circuit made of the coil resistance  $R_c$ , the sample resistance  $R_s$  and the voltage  $U_s$  induced by the magnetization  $M$  within the volume  $V$  at a certain point  $r$ . The voltage  $U_s$  is then calculated using

$$U_s(t) \propto \omega B M V \cos(\omega t) \quad (2.24)$$

with  $B$  the magnetic field transverse to the main  $B_0$  field and  $\omega$  the angular frequency. This formula can be transformed into

$$U_s(r) = -j\omega V M \frac{B(r)}{I} \quad (2.25)$$

using the principle of reciprocity (Hoult and Richards, 1976). The effective noise voltage is expressed by the thermal noise of the coil resistance  $R_c$  and the sample resistance  $R_s$ :

$$U_{n_{eff}} = \sqrt{4kT\Delta f(R_c + R_s)} \quad (2.26)$$

with  $k$  the Boltzmann constant,  $\Delta f$  the receiver bandwidth and  $T$  the temperature of the coil and the sample.

The resulting SNR is calculated as the ratio of the signal and  $\sqrt{2}$  times the effective noise:

$$\begin{aligned} \frac{S}{N}(r) &= \frac{|U_s(r)|}{\sqrt{2}U_{n_{eff}}} \\ &= \frac{|\omega VM \frac{B(r)}{I}|}{\sqrt{8kT\Delta f(R_a + R_l)}} \\ &= \frac{\omega V |MB(r)|}{\sqrt{8kT\Delta f(R_a |I|^2 + R_l |I|^2)}} \\ &= \frac{\omega V |MB(r)|}{\sqrt{16kT\Delta f(P_a + P_l)}}. \end{aligned} \quad (2.27)$$

### 2.2.2.3 Coil coupling

This subchapter is mainly based on (Reykowski, 1998).

If two coils are placed in the vicinity of each other signal can spill over from one coil to the other. This effect is called coupling. As depicted in Figure 2.3 this effect can be described as mutual complex impedance  $Z_{12} = R_{12} + jX_{12}$  of the two ports.

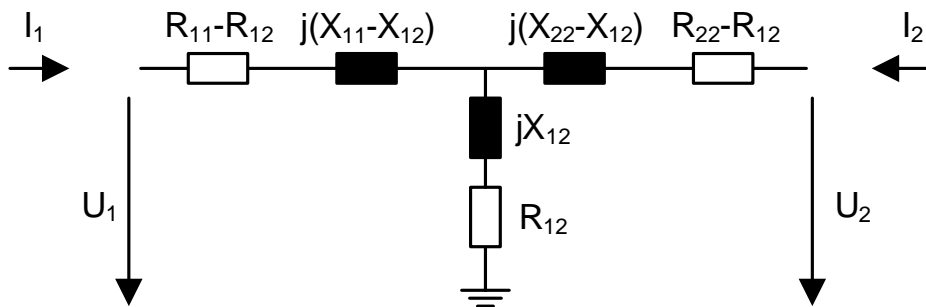


**Figure 2.3:** Equivalent circuit diagram of a coupled two port system.

This mutual impedance can be derived from the relation of the currents and the voltages of the two ports. The relation of the ports can be expressed as:

$$\begin{bmatrix} U_1 \\ U_2 \end{bmatrix} = \begin{bmatrix} Z_{11} & Z_{12} \\ Z_{21} & Z_{22} \end{bmatrix} \cdot \begin{bmatrix} I_1 \\ I_2 \end{bmatrix} \quad (2.28)$$

with

$$Z_{11} = R_{11} + jX_{11} \quad (2.29)$$

$$Z_{22} = R_{22} + jX_{22} \quad (2.30)$$

$$Z_{12} = Z_{21} = R_{12} + jX_{12}. \quad (2.31)$$

This results in the mutual resistance

$$Z_{12} = Z_{21} = \frac{U_1}{I_2} \Big|_{I_1=0} = \frac{U_2}{I_1} \Big|_{I_2=0} \quad (2.32)$$

The coupling can also be expressed as the ratio of the power  $P_L$  to  $P_T$  with  $P_L$  the power which is delivered to the load and  $P_T$  the generated power  $P_G$  without the reflected power  $P_R$ :

$$C = \frac{|P_L|}{|P_T|} = \frac{P_G \cdot |S_{21}|^2}{P_G} = |S_{21}|^2 \quad (2.33)$$

which is equal to the transmission S-parameter of the two ports which are also called coupling parameter.

If coupling appears in Tx arrays power is transmitted from one channel to the other channel and therefore is lost. In Rx arrays coupling can have a negative effect on the SNR. Nevertheless, coupling is also used, e.g. for double resonant coils or detuning circuits.

### Mutual impedance

The mutual impedance can be calculated by feeding one port with a known current and measure the voltage at the other port. The total power which is flowing in both coils then can be written as:

$$\begin{aligned} P_{total} &= V_1 I_1^* + V_2 I_2^* \\ &= Z_{11} |I_1|^2 + Z_{12} I_1^* I_2 + Z_{21} I_1 I_2^* + Z_{22} |I_2|^2. \end{aligned} \quad (2.34)$$

The total power can also be expressed using the total electric field  $\mathbf{E}$  and the total current density  $\mathbf{J}$ :

$$P_{total} = - \iiint \mathbf{E} \cdot \mathbf{J}^* dv = - \iiint (\mathbf{E}_1 + \mathbf{E}_2) \cdot (\mathbf{J}_1 + \mathbf{J}_2)^* dv \quad (2.35)$$

The four impedances of equation 2.35 can be written as:



$$\begin{aligned}
Z_{11} &= -\frac{1}{|I_1|^2} \iiint \mathbf{E}_1 \cdot \mathbf{J}_1^* dv \\
Z_{22} &= -\frac{1}{|I_2|^2} \iiint \mathbf{E}_2 \cdot \mathbf{J}_2^* dv
\end{aligned} \tag{2.36}$$

and

$$Z_{12} = Z_{21} = -\frac{1}{I_1 I_2^*} \iiint \mathbf{E}_1 \mathbf{J}_2^* dv = -\frac{1}{I_1^* I_2} \iiint \mathbf{E}_2 \mathbf{J}_1^* dv. \tag{2.37}$$

Equation 2.37 can be simplified to

$$Z_{12} = \int \mathbf{E}_1 dr_1. \tag{2.38}$$

by assuming a constant current  $I_1 = 1$  and an infinitely thin wire.

If the mutual impedance is not zero a current in one port causes a voltage at the other port. The real part of the complex mutual impedance is causing a noise correlation at the coil ports.

The mutual impedance can be described by three different effects which are described in the following.

### Mutual inductance

MR coils are antennas which are sensitive to the electric more than the magnetic field. Therefore the main source of coupling is inductive coupling if no resistive load is present. Using equation 2.38 the mutual inductance can be expressed as

$$Z_{12} = j\omega M_{12} = - \oint \mathbf{E}_1 dr_2 = j\omega \oint \mathbf{A}_1 dr_2 \tag{2.39}$$

with A the magnetic vector potential

$$A_1 = \frac{\mu_0}{4\pi} \oint \frac{dr_1}{|r_2 - r_1|} \tag{2.40}$$

and the magnetic coupling coefficient

$$M_{12} = \frac{\mu_0}{4\pi} \oint \oint \frac{dr_1 dr_2}{|r_2 - r_1|} \tag{2.41}$$

whereas  $|r_2 - r_1|$  is the distance between the observing point on the coil two to the point of integration on coil one.

### Mutual capacitance

Capacitive coupling appears at points where two conductors cross each other. At these points they form a plate capacitor with a capacitance of

$$C = \epsilon \frac{A}{d} \quad (2.42)$$

with A the area of the plate capacitor, d the distance of the conductors and  $\epsilon$  the dielectric constant.

Additionally, capacitive coupling increases with the frequency.

In order to reduce capacitive coupling the conductor at overlapping points should be as small as possible. The current which flows over this capacitance can also be reduced if the overlapping is placed at so called 'null' points where the electrical potential on the conductor is almost zero.

### Mutual resistance

If two coils are placed over a conductive sample a current induced into the sample will induce a current by itself in the other coil. Using these currents the mutual noise resistance can be calculated:

$$\begin{aligned} R_{12} &= \frac{1}{I_1 I_2^*} \iiint \mathbf{E}_1 \cdot \mathbf{J}_2^* dv \\ &= \frac{1}{I_1 I_2^*} \iiint \mathbf{E}_1 \cdot \sigma \mathbf{E}_2^* dv \\ &= \frac{\omega^2}{I_1 I_2^*} \iiint \sigma \mathbf{A}_1 \cdot \mathbf{A}_2^* dv \end{aligned} \quad (2.43)$$

#### **2.2.2.4 Transmit-only receive-only system**

A common approach for many MR coil systems is the so called Transmit-only Receive-only (ToRo) (Barberi et al., 2000) system. In most clinical scanners and for many research systems this approach is realized. In the ToRo approach one coil is used for transmitting the signal and a different coil is used for receiving the signal.

The Tx coil is most often a large volumetric coil encircling the object of interest. It is often realized as a so called Birdcage (BC) coil (Hayes et al., 1985). This is done to produce a homogeneous  $B_1^+$ -field which is necessary to achieve an equal flip angle within the excitation volume.

The Rx coil is usually a small coil placed in the immediate vicinity of the sample. This is done for two reasons. First, the sensitivity of a coil increases with decreasing size. Second, due to the principle of reciprocity the SNR increases with decreasing distance of the coil to the sample.

In order to minimize inductive coupling in between the Tx and the Rx coil the Tx coil has to be made electrically off resonant during the Rx phase and vice versa. This has to be done for two reasons. First, to protect the Rx coil and Rx chain during the high power Tx pulse. Second, to reduce noise due to mutual inductance of the Tx and the Rx coil during the Rx phase.

The process of making a coil off resonant is also called detuning. This is realized using RF switches. Switches can be, e.g. microelectromechanical systems (MEMS) or PIN diodes. PIN diodes are most often used since they can stand high voltages. PIN diodes present an electrical short if they are biased by a current and an electrical open if a negative voltage is applied. This direct current (DC) signal has to be synchronized with the Tx and Rx phase of the sequence. Commonly the DC supply is fed via inductors with a high inductance. This prevents the alternating current (AC) MR signal to flow into the DC path.

In case of a common BC coil PIN diodes are placed in series with the conductors. During transmit the PIN diodes are forward biased and the coil is resonant. During receive negative voltage is applied to the PIN diodes and the coil is off resonant.

The same approach could be applied for Rx coils but a PIN diode inhabits an ESR which increases the coil noise. Additionally, the PIN diode may brake during the transmit phase if too much power of the Tx coil is coupled into the Rx coil. Therefore another approach is utilized. A sketch of an exemplary Rx coil is given in Figure 2.4. The active detuning circuit consists of a PIN diode and an inductor. This inductor is selected in a way that it forms a resonance circuit at the Larmor frequency together with the capacitor in parallel. If the PIN diode is biased this resonance circuit is coupled with the Rx coil. Due to the coupling the resonance of the Rx coil will split and two resonances will appear but none of them at the Larmor frequency. Therefore the coil is detuned.

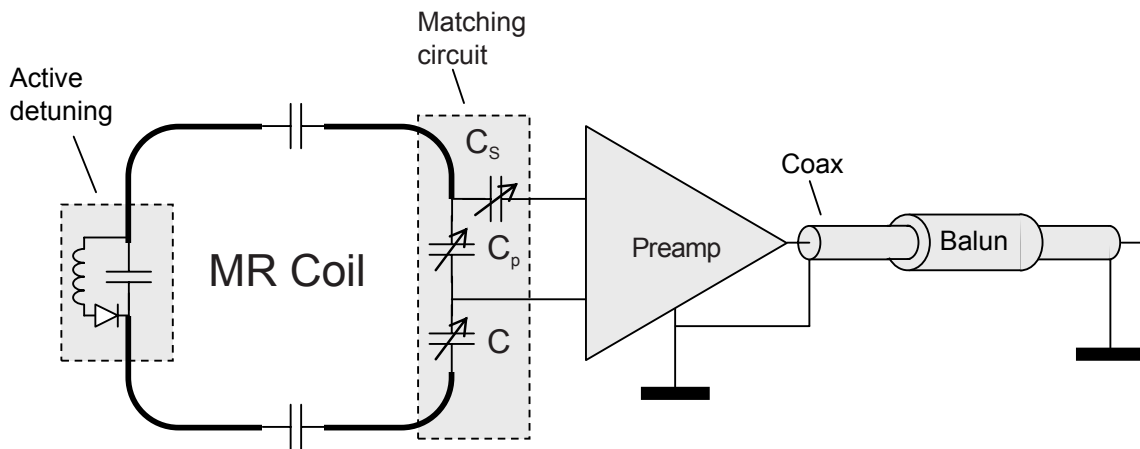


**Figure 2.4:** Sketch of an Rx coil (Reykowski, 2006).

Depending on the design of the coil and the sample load the input impedance of the coil is defined. In order to achieve the lowest possible noise figure of the preamplifier the input impedance of the coil has to be matched to  $50 \Omega$ . This is done by a capacitive matching circuit comprised of a parallel ( $C_p$ ) and a serial ( $C_s$ ) capacitor.

Finally after the Rx signal is amplified it is directed to the MR system's receiver via a coaxial cable. In order to suppress sheath waves a cable trap or a so called Balun (balanced-unbalanced) is added. Sheath waves can occur when a balanced circuit (the Rx coil) is connected to an unbalanced circuit (the coaxial cable). This will add common mode noise to the Rx signal. Additionally, sheath waves can occur during transmission if the length of the Rx cable is near  $\frac{\lambda}{4}$  of the Larmor frequency. This can heat up the cable and endanger the patient.

Baluns are most often manufactured by winding the coaxial cable to an inductor and bridge it with a capacitor. This resulting parallel circuit is then tuned to the Larmor frequency.

### 2.2.2.5 Receive array

The sensitivity of the Rx coils is increased by designing them as small coils which limits their sensitivity volume. In order to extend the high sensitivity of small coils over a large volume multiple Rx coils are combined to a so called Rx array. This is done in a way that this array covers the body part of interest. That leaves two problems. First, the Rx coils couple with each other and second the resulting individual images have to be combined in a way to produce the best SNR image. These problems are addressed in the following.

#### Decoupling

There are different ways to decouple adjacent coils. One method proposed by Roemer et al (Roemer et al., 1990) is overlap decoupling. Due to the mutual inductance of two coils current in one coil induces a current in the other coil and vice versa. If these two coils are overlapped to a certain extent the field which are produced by the currents which are induced by the mutual inductance cancel out. The coils are decoupled.

Another way to decouple adjacent loops is the common conductor method. This is done by designing two coils in a way that they share at one position the same conductor. The coupling impedance  $Z$  can then be removed by adding a capacitor to this common conductor. This capacitor can be adjusted in a way that it cancels out the mutual inductance  $M$ :

$$Z = j\omega M - j\frac{1}{\omega C} = 0 \quad (2.44)$$

In order to decouple non-adjacent coils two methods are commonly used. The transformer decoupling method is very similar to the overlapping method. The non-adjacent coupled coils are cut at one position. At this position the coil is extended with a conductive loop. This conductive loop is placed over the conductive loop of the second coil. The coupling fields are then canceled out. Since the area of these loops is usually too small to decouple the coils the loops are wound to form inductors. This increases the resulting fields. These coupled inductors are practically a transformer.

Another way to decouple two non-adjacent coils is the so called preamplifier decoupling (Roemer et al., 1990). The amplifying element of a preamplifier is usually a field-effect transistor (FET). One can select a FET with a low impedance which presents almost a short to the ground. By adding an inductor in front of the FET this inductor forms a quasi parallel circuit with the capacitor of the matching circuit of the coil. The matching circuit can now be adjusted in a way that the coil input impedance is matched to  $50 \Omega$  and at the same time the input impedance of the preamplifier is a parallel circuit tuned to the Larmor frequency. This presents a quasi open for the coil which reduces the current flow in the coil and therefore reduces mutual inductance.

Nevertheless, in recent years this method was found to be inefficient to preserve SNR despite coil coupling in some circumstances. This effect is described in detail in paragraph 2.2.2.6.

### Maximum available SNR

Each coil of an Rx array produces its own SNR image. These individual SNR images have to be combined into a single MR image. There are different approaches to combine the individual images. One approach was presented which produces the maximum available combined SNR image (Schnell et al., 2000). This method is based on the common matched filter approach. A schematic of the basic principle of the method is depicted in figure 2.5.

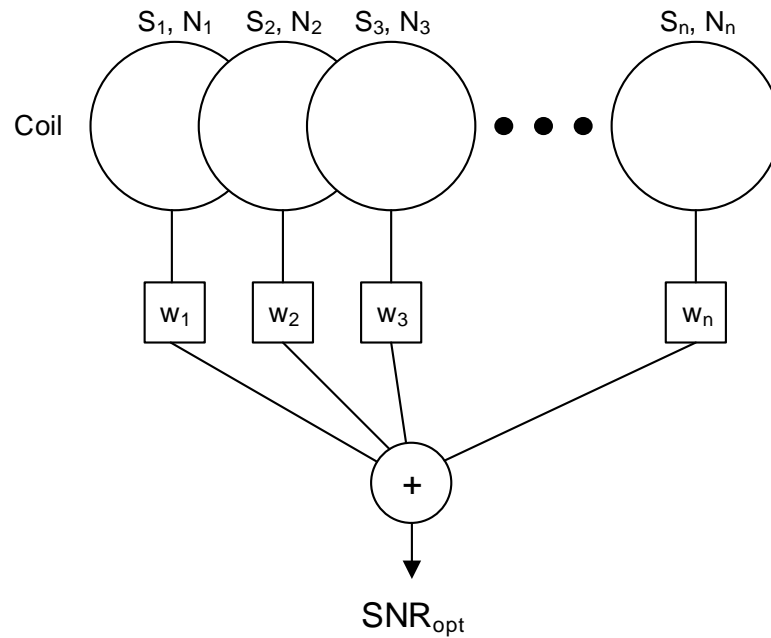


**Figure 2.5:** Schematic of the channel combination algorithm.

Each pixel of the individual SNR images is weighted with its individual weighting factor  $w$ . This results in the maximum available SNR for each pixel. The weighting factors are calculated by the inverse noise correlation matrix  $\mathbf{R}$  multiplied with the conjugate complex signal intensities  $\mathbf{S}^*$ :

$$\mathbf{W}_n^{opt}(r) \propto [\mathbf{R}_n(r)]^{-1} \mathbf{S}_n^*(r) \quad (2.45)$$

The noise correlation is defined as:

$$\mathbf{R} = \begin{bmatrix} \langle |U_{R,1}(t)|^2 \rangle & \langle |U_{R,1}(t)U_{R,2}(t)^*| \rangle & \dots & \langle |U_{R,1}(t)U_{R,N}(t)^*| \rangle \\ \langle |U_{R,2}(t)U_{R,1}(t)^*| \rangle & \langle |U_{R,2}(t)|^2 \rangle & \dots & \langle |U_{R,2}(t)U_{R,N}(t)^*| \rangle \\ \vdots & \vdots & \ddots & \vdots \\ \langle |U_{R,N}(t)U_{R,1}(t)^*| \rangle & \langle |U_{R,N}(t)U_{R,2}(t)^*| \rangle & \dots & \langle |U_{R,N}(t)|^2 \rangle \end{bmatrix} \quad (2.46)$$

with  $U$  the different noise voltages and  $\langle |\cdot| \rangle$  the notation for the time average. Finally, the combined maximum available SNR is calculated using:

$$SNR_{opt}(r) = \frac{\omega MW}{\sqrt{8k_B T \Delta f}} \sqrt{\mathbf{S}^T \mathbf{R}^{-1} \mathbf{S}^*}. \quad (2.47)$$

### 2.2.2.6 Pre-amplifier coupled noise

As described in chapter 2.2.2.5 a common approach to decouple non-adjacent coils is preamplifier decoupling. Depending on the setup SNR degradation can be found despite preamplifier coupling. This effect is called preamplifier coupled noise. The amount of SNR degradation - if SNR degradation is present due to coil coupling - depends on the product of the coupling factor  $k$  and the Q-factor  $Q$ . If  $kQ = 1$  usually no SNR degradation is expected but if  $kQ \gg 1$  SNR degradation is expected depending on the amount of  $kQ$  (Vester et al., 2012).

The coupling factor can be calculated from the frequencies of the common mode  $f_c$  and the odd mode  $f_o$  which appear if two coils are coupled:

$$k = \frac{|f_o - f_c|}{\sqrt{f_o \cdot f_c}} \quad (2.48)$$

The Q-factor is calculated as in equation 2.21.

First we introduce a slightly different equivalent circuit diagram for two coupled coils compared to figure 2.3. This circuit diagram is given in Figure 2.6, **A**) with the following expressions:

$$Q = \frac{X_L}{R} \quad (2.49)$$

$$M = k \cdot L = jX_L \cdot k \quad (2.50)$$

with  $X_L$  the reactance and  $M$  the mutual inductance.

In a first step the circuit diagram can be simplified **B**) if one considers that the reactance of an inductor is the same as the negative reactance of a capacitor if both coupled coils are resonant at the same frequency. Now the resistance can be normalized using equation 2.49. The resulting circuit diagram is the equivalent of a quarterwave line **C**).

In a coupled case a noise current  $i_{n1}$  of one preamplifier induces a noise voltage  $u_{n2}^*$  at the second preamplifier. Since the coupled coils are connected via a quasi quarterwave line this noise coupling does only appear in the diagonal of the noise correlation matrix since the noise currents and noise voltages have a relative phase of  $\mp 90^\circ$  to each other. Entries

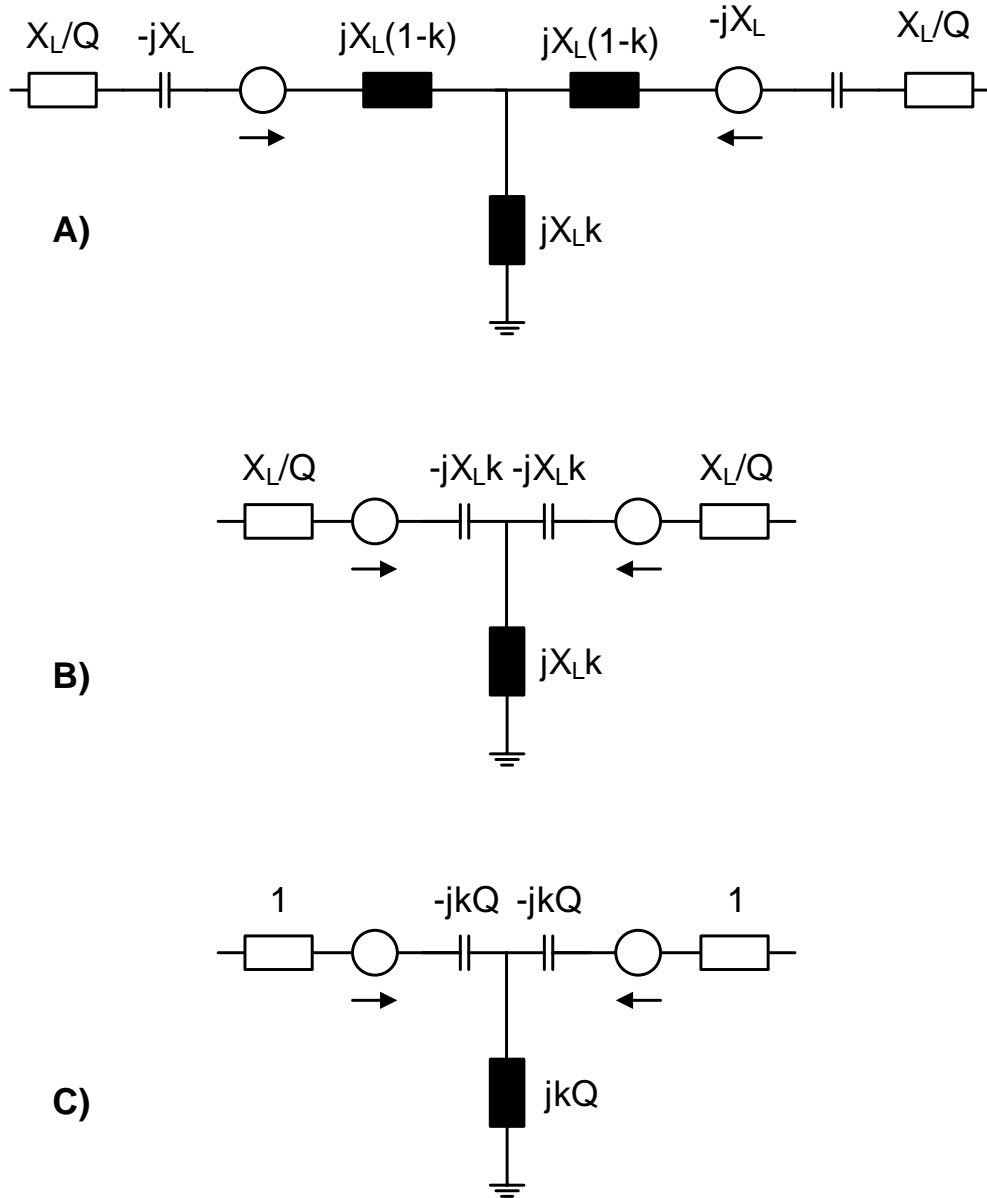


**Figure 2.6:** Equivalent circuit diagram of two coupled coils and its simplification.

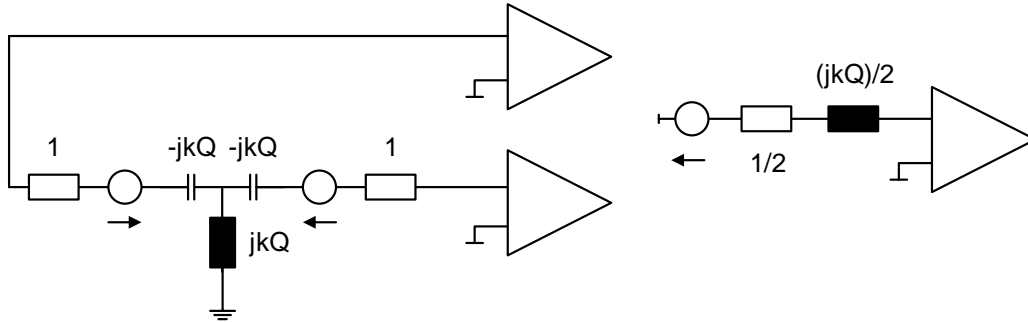
in the diagonal of the noise correlation matrix can not be used for SNR regeneration. Therefore SNR can be degraded by coupled coils despite preamplifier decoupling.

In order to quantify this effect Vester et al (Vester et al., 2012) described it using two coupled preamplifiers. The respective equivalent circuit diagrams are given in Figure 2.7.

The circuit diagrams of the two modes (common and odd mode) which appear if two coils are coupled connect the two preamplifiers of the two coils. For each mode the optimum input impedance  $Z_{opt}$  and the real input impedance  $Z_{real}$  can be calculated by merging the two preamplifiers to one. The resulting impedance for the common mode is:

$$Z_{opt} = \frac{1}{2} \quad Z_{real} = \frac{1 + jkQ}{2} \quad (2.51)$$

Common mode



Odd mode

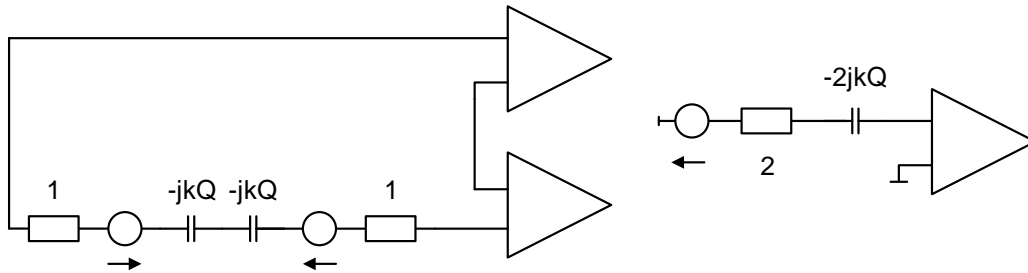


**Figure 2.7:** Equivalent circuit diagram of two coupled preamplifiers at the two occurring modes.

and for the odd mode:

$$Z_{opt} = 2 \quad Z_{real} = 2 \cdot (1 - jkQ). \quad (2.52)$$

The resulting reflection factor  $r$  can be expressed as

$$|r| = \sqrt{\frac{(kQ)^2}{4 + (kQ)^2}} \quad (2.53)$$

Since a nonzero reflection factor will cause SNR degradation the amount of SNR penalty is determined by  $kQ$ . In order to reduce this reflection factor two methods were suggested (Vester et al., 2012). The first is broadband matching. Here the input impedance is changed in a way that the reflection circle in the smithchart encircles the middle and therefore is more sensitive to both occurring impedances. The second is mode matching. Here a single mode can be selected which is found to be the most sensitive mode in the region of interest.

A detailed discussion of the resulting noise figures as well as engineering details are given in chapter 3.

## 2.3 EM simulation background

In the previous paragraphs it was shown that electromagnetic fields play a key role in MRI. The EM fields we are focusing on in this work are the Tx and Rx RF fields of the different RF resonators used for MRI.



In order to measure these fields and optimize the performance of an RF system concerning its EM field properties using measurements, one would need to build the RF setups on the workbench and evaluate each optimizing step via MR measurements. Such an optimization process is expensive and time consuming.

A powerful tool to avoid this excessive optimization process are EM field simulations. Using this tool one can acquire all important EM fields, which are necessary for the optimization process. Additionally, within the same simulation other results as S-parameters or field properties, which cannot easily be measured, e.g. SAR distribution, are processed. The use of such simulations dramatically speeds up the engineering process of coil developing.

EM simulations discretize a defined simulation volume in small parts, the so called mesh cells, and solve Maxwell's equations in these cells. This allows all EM fields and S-parameters to be calculated.

Especially for simulations in the field of RF setups for MRI two solvers are widely used. These are the Time Domain (TD) solver and the Frequency Domain (FD) solver. The solvers use both different mesh strategies and different implementations of Maxwell's equations. There are multiple criteria, which have to be considered when selecting the appropriate solver. In the following paragraphs Maxwell's equation will be formulated and two standard methods for the TD and FD solver will be described. A detailed comparison and consideration of these two solvers regarding RF problems in an MRI environment is given in Chapter 7.

### 2.3.1 Maxwell's equation

Maxwell's equations are a set of partial, linear, coupled 1st order differential equations. Commonly EM solvers use these equations to solve the EM fields in the simulation volume. The Maxwell's equations in their differential form in SI units are:

$$\nabla \cdot E = \frac{\rho}{\epsilon_0} \quad (2.54)$$

$$\nabla \cdot B = 0 \quad (2.55)$$

$$\nabla \times E = -\frac{\partial}{\partial t} B \quad (2.56)$$

$$\nabla \times B = \mu_0 \left( J + \epsilon_0 \frac{\partial}{\partial t} E \right) \quad (2.57)$$

with E the electrical field strength,  $\rho$  the electrical charge density,  $\epsilon$  the electric permittivity, B the magnetic flux density, and J the electrical current density.

The first of Maxwell's equations is also called Gauss's law. It states that the electric flux through a closed surface is proportional to the total electric charge enclosed by this surface. The second equation is also called Gauss's law for magnetism. It says that the total magnetic flux through a closed surface must be zero. The third equation is also called Faraday's law of induction. It states that a time varying magnetic field induces an electric field. The last equation is also called Ampere's law. It says that a time varying electric field and an electric current generate a magnetic field.

Furthermore it is that the magnetic flux density is related to the magnetic field strength via the magnetic permeability  $\mu$

$$B = \mu H \quad (2.58)$$

and the electrical displacement is related to the electrical field strength via the electric permittivity  $\epsilon$

$$D = \epsilon E. \quad (2.59)$$

and the electrical current density is related to the electrical field strength in conductive media via the conductivity  $\sigma$

$$J = \sigma E \quad (2.60)$$

In the following, two common methods for implementing and solving Maxwell's equations within an EM simulation volume are described.

### 2.3.2 Time domain solver

There are two common approaches implementing the TD solver for EM problems. One is the Finite-Difference Time Domain (FDTD) method (Yee, 1966) and the other is the Finite Integration Technique (FIT) method (Weiland, 1977). The actual implementation is depending on the software package used. In this work the software package Microwave Studio (MWS) from CST (CST, Computer Simulation Technology GmbH, Darmstadt, Germany) is used. CST is implementing the FIT approach. Therefore this approach will be described in the following.

Unlike other methods such as the FDTD approach, the FIT approach is utilizing the integral form of Maxwell's equations:

$$\oint_{\partial V} \vec{D} \cdot d\vec{A} = \int_V \rho \cdot dV \quad (2.61)$$

$$\oint_{\partial V} \vec{B} \cdot d\vec{A} = 0 \quad (2.62)$$

$$\oint_{\partial A} \vec{E} \cdot d\vec{s} = - \int_A \frac{\partial}{\partial t} \vec{B} \cdot d\vec{A} \quad (2.63)$$

$$\oint_{\partial A} \vec{H} \cdot d\vec{s} = \int_A \left( \frac{\partial}{\partial t} \vec{D} + \vec{J} \right) \cdot d\vec{A} \quad (2.64)$$

In order to solve these equations the simulation volume has to be subdivided into small parts, the so called mesh cells or grid cells. For the TD approach the simulation volume has to be meshed into hexahedral elements. As it is shown in Figure 2.8 a second mesh is set up orthogonally to the first one. The second grid is shifted spatially half a grid size. The solver discretizes Maxwell's equations on these grids. As indicated in Figure 2.8 Maxwell's equations are formulated on each facet of the different cells with  $\mathbf{e}$  the electric voltage,  $\mathbf{h}$  the magnetic voltage,  $\mathbf{b}$  the magnetic flux and  $\mathbf{d}$  the electric flux.

The implementation of Faraday's law is exemplarily shown in Figure 2.9. The left side of the equation is the sum of the voltages ( $e_{i-1}$ ) on one facet of one grid. Therefore



$$\mathbf{C} \mathbf{e} = -\frac{d}{dt} \mathbf{b} \quad (2.67)$$

$$\tilde{\mathbf{C}} \mathbf{h} = \frac{d}{dt} \mathbf{d} + \mathbf{j} \quad (2.68)$$

The last thing to do is to introduce the material properties. This is done by approximating the integral values of the relations between voltages and fluxes over the grid edges and cell areas. The resulting coefficients are summarized in matrices again:

$$\vec{\mathbf{D}} = \epsilon \vec{\mathbf{E}} \rightarrow d = M_\epsilon e \quad (2.69)$$

$$\vec{\mathbf{B}} = \mu \vec{\mathbf{H}} \rightarrow b = M_\mu h \quad (2.70)$$

$$\vec{\mathbf{J}} = \sigma \vec{\mathbf{E}} + \vec{\mathbf{J}}_s \rightarrow j = M_\sigma e + j_s \quad (2.71)$$

Finally, the update formulation for the loss-free case can be expressed by substituting the time derivatives by central differences:

$$e^{n+\frac{1}{2}} = e^{n-\frac{1}{2}} + \Delta t M_\epsilon^{-1} [\tilde{\mathbf{C}} M_\mu^{-1} b^n + k_s^n] \quad (2.72)$$

$$b^{n+\frac{1}{2}} = b^n - \Delta t C e^{n+\frac{1}{2}} \quad (2.73)$$

In order to calculate the unknown calculation variables  $\mathbf{e}$  and  $\mathbf{b}$ , which are located alternately in time, the leap-frog scheme is used as indicated in Figure 2.10.

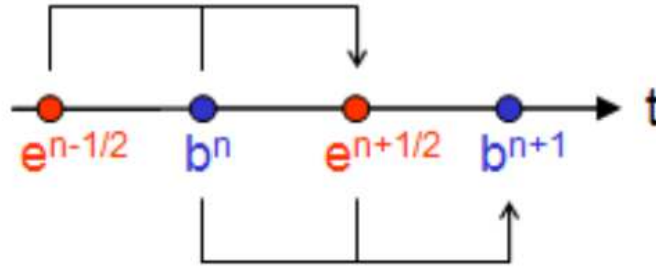


**Figure 2.10:** Exemplary leap-frog scheme. Courtesy to CST studio 2017 help.

For example, the magnetic flux  $\mathbf{b}$  at  $t = n + 1$  is calculated by the magnetic flux at  $t = n$  and the electric voltage  $\mathbf{e}$  at  $t = n + \frac{1}{2}$ .

Additionally, the stability limit for the computation is given by the Courant-Friedrichs-Levy criterion:

$$\Delta t \leq \frac{\sqrt{\epsilon \mu}}{\sqrt{\left(\frac{1}{\Delta x}\right)^2 + \left(\frac{1}{\Delta y}\right)^2 + \left(\frac{1}{\Delta z}\right)^2}} \quad (2.74)$$

with  $\Delta x$ ,  $\Delta y$  and  $\Delta z$  the grid size.

### 2.3.3 Frequency domain solver

The second approach of solving Maxwell's equation in a simulation volume is the Frequency Domain solver. Compared to the TD solver the FD solver can be used in any grid. One commonly used mesh type is the tetrahedral mesh, which divides the simulation volume in pyramidal cells. In contrast to the hexahedral mesh, which extends small local meshes over the whole simulation volume, the tetrahedral mesh provides a local fine mesh only at places where it is required.

In order to implement the FD method Maxwell's equations have to be reformulated. Ampere's law in the macroscopic formulation can be expressed as

$$\nabla \times H = J + \frac{\partial}{\partial t} D \quad (2.75)$$

$$\epsilon \frac{\partial}{\partial t} E = \nabla \times H - J \quad (2.76)$$

and Faraday's law can be expressed as

$$\nabla \times H = -\frac{\partial}{\partial t} B \quad (2.77)$$

$$\mu \frac{\partial}{\partial t} H = -\nabla \times E. \quad (2.78)$$

These two equations can be combined into a single equation

$$\nabla \times \frac{1}{\mu} \nabla \times E + \epsilon \frac{\partial^2}{\partial t^2} E = -\frac{\partial}{\partial t} J. \quad (2.79)$$

In order to solve the equation in the FD, the time derivatives  $\frac{\partial}{\partial t}$  are replaced by the harmonic dependence given by  $\exp(i\omega t)$  with  $\omega$  the angular frequency at which the system is solved. This transforms equation 2.79 to

$$\nabla \times \frac{1}{\mu} \nabla \times E - \epsilon \omega^2 E = -i\omega J. \quad (2.80)$$

In order to solve this problem, the concept of the variational method is applied. This means that a 'test function'  $F$  is multiplied and an integration over the physical volume  $\Omega$  is applied. This leads to

$$\int_{\Omega} (\nabla \times E) (\nabla \cdot F) - \omega^2 \int_{\Omega} \epsilon E \cdot F = i\omega \int_{\Omega} J \cdot F. \quad (2.81)$$

Now  $F$  is approximated numerically to find the best solution to the equation.

## 2.4 X-nuclei background

### 2.4.1 Physiological background

The sodium and the chloride nuclei are the most abundant non-organic cations and anions in the human body. The intra/extra-cellular concentration of sodium is 12-20/145 mmol/l (Hilal et al., 1988) and of chlorine 5/99-109 mmol/l (Dorland, 1915). The resulting difference of potential between the intra/extra-cellular space is between 5 and 100mV

(Silbernagl and Despopoulos, 2007). The concentration gradient of the ions is maintained by passive and active transport mechanisms. One of the most important active transport mechanisms is the sodium-potassium pump ( $\text{Na}^+ - \text{K}^+$ -ATPase). This mechanism maintains the electric and chemical potential by pumping three sodium ions out of the cell while pumping two potassium ions inside the cell (Figure 2.11,(Silbernagl and Despopoulos, 2007)).

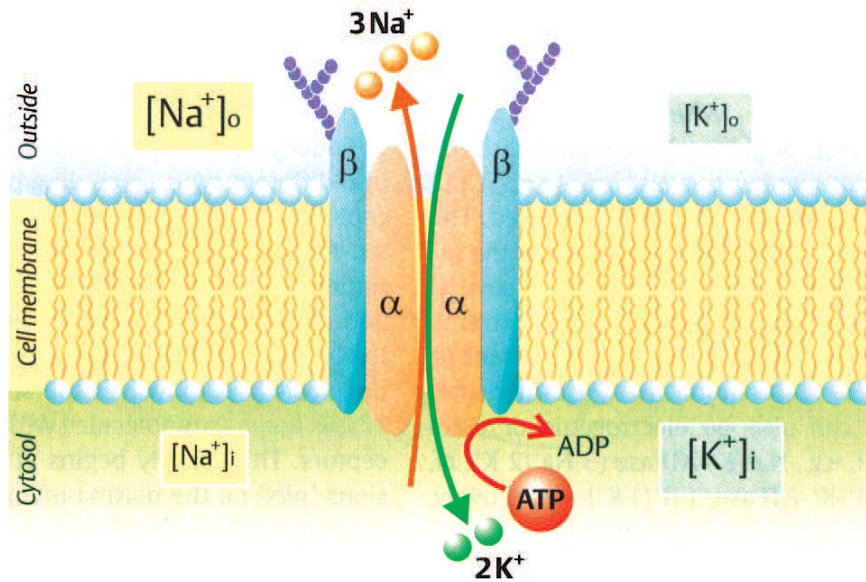


**Figure 2.11:** Schematic of the  $\text{Na}^+ - \text{K}^+$ -pump (Silbernagl and Despopoulos, 2007).

The necessary energy for this transport mechanism is obtained by the conversion of adenosine triphosphate to adenosine diphosphate. In case of pathological processes, e.g. ischemia or hypoxia, an adenosine triphosphate deficiency may occur. This causes a degradation of the  $\text{Na}^+ - \text{K}^+$ -ATPase. In case of breakdown of the  $\text{Na}^+ - \text{K}^+$ -ATPase, sodium flows from the extra- to the intra-cellular space due to the concentration gradient. Since this happens faster than potassium can flow into the extra-cellular space. This results in liquid flowing into the cell following the osmotic gradient which causes the cell to burst. During this process the extra-cellular space increases which results in a higher sodium and chlorine concentration. This increase in concentration can be measured using MRI. Therefore the sodium as well as the chlorine concentration is sensitive intrinsic markers of tissue vitality and viability (Baier et al., 2014; Schepkin et al., 2006, 2005) in MRI measurements.

## 2.4.2 X-nuclei MRI

The relaxation times of the  $^{23}\text{Na}$  and  $^{35}\text{Cl}$  nuclei are short compared to the relaxation times of  $^1\text{H}$ . This is due to the coupling between the electric quadrupole moment and the surrounding electric field gradient (Werbelow, 2007). In order to avoid signal loss due to the fast relaxation times of  $^{23}\text{Na}$  and  $^{35}\text{Cl}$  sequences with very short echo times should be used. One such sequence uses a radial readout of the k-space. Compared with common sequences with a cartesian readout, the radial sequence starts in the k-space center. Therefore the echo time is only limited by the pulse length and the time the system needs to switch from the Tx pulse to the readout. An example of a 2D radial readout is given in Figure 2.12.

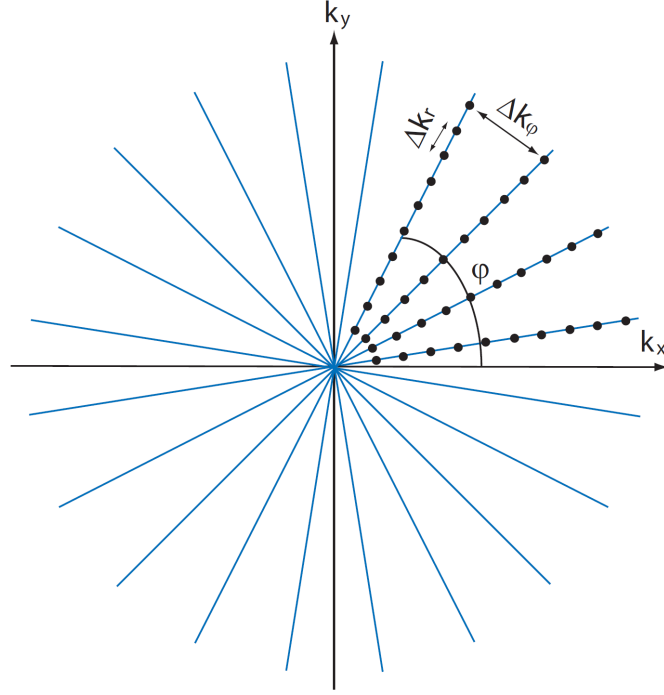


**Figure 2.12:** Example of the trajectory of a 2D radial readout (Konstandin, 2012).

The same sampling can be performed for 3D. In order to fulfill the Nyquist criterion, the distances  $\Delta k_r$  and  $\Delta k_\phi$  must be smaller than the inverse of the FoV.

The number of projections for a fully sampled k-space is calculated using

$$N_{proj} = 4\pi \left( \frac{N_y}{2} \right)^2 \quad (2.82)$$

with  $N_y$  the matrix size. The matrix size is calculated by dividing the FoV by the resolution.

In density-adapted radial sampling, k-space center is sampled more densely than its periphery. In general a non-uniformly sampled k-space decreases SNR. Therefore Nagel et. al (Nagel et al., 2009) introduced the density-adapted sampling scheme. This sequence modifies the gradients in a way the sampling points of each projection are sparser near to the k-space center which results in a uniform sampled k-space. An example of such a gradient form and the comparison to the conventional gradient form is given in Figure 2.13.

For the conventional radial readout the gradient magnitude remains constant during the readout time. In case of the density-adapted approach the gradient is initially kept at a certain magnitude. Afterwards the gradient magnitude is decreased which results in a tighter sampling in the periphery of the k-space. Therefore a more uniform k-space sampling is achieved.

In the final step the k-space data is re-gridded onto a cartesian grid and Fourier transformed is performed to obtain the final image.

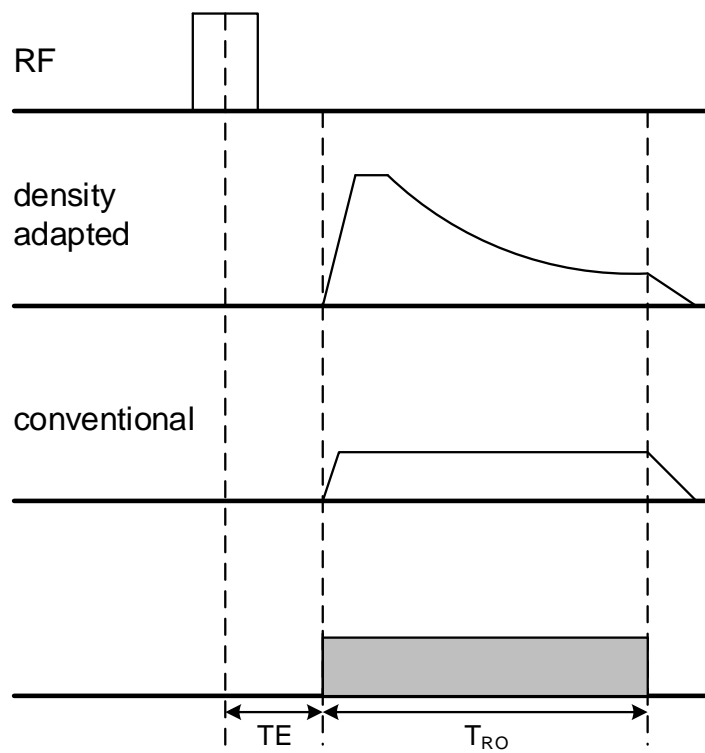


**Figure 2.13:** Comparison of a density-adapted to a non density-adepted gradient for a 3D radial readout.



# “Reducing signal-to-noise ratio degradation due to coil coupling in a receiver array for $^{35}\text{Cl}$ MRI at 9.4 Tesla: A comparison of matching and decoupling strategies”

*Concept Magn Reson B, DOI: 10.1002/cmr.b.21383*

3

## 3.1 Introduction

Conventional magnetic resonance imaging (MRI) is performed using the signal that originates from hydrogen ( $^1\text{H}$ ) nuclei. Yet, the use of non-hydrogen or so-called X-nuclei is of increasing interest for both preclinical and clinical studies (Baier et al., 2014; Kirsch et al., 2010; Nagel et al., 2014). In X-nuclei MRI, sodium ( $^{23}\text{Na}$ ) is the most commonly studied nucleus given its higher Signal-to-Noise Ratio (SNR) in comparison to other X-nuclei. This is due to its higher natural abundance and gyromagnetic ratio. However, other nuclei such as chlorine ( $^{35}\text{Cl}$ ) are of interest despite their lower SNR ( $^{35}\text{Cl}$  provides approximately 20 times less signal than  $^{23}\text{Na}$  and  $^{23}\text{Na}$  12.000 times less signal than  $^1\text{H}$  (Baier et al., 2014)) due to the additional diagnostic information they can provide. Next to different spectroscopic methods (Brown et al., 2016b; Neuberger et al., 2017),  $^{35}\text{Cl}$  MRI has been found in previous preclinical and clinical studies to provide further insights into cellular metabolism (Baier et al., 2014; Kirsch et al., 2010; Nagel et al., 2014; Schepkin et al., 2014). Although the SNR limitation has been mitigated in several studies by the use of ultra-high field scanners (21T (Schepkin et al., 2014), 9.4T (Baier et al., 2014; Kirsch et al., 2010), 7T (Nagel et al., 2014)), further gains can be obtained from using purpose-built radio frequency (RF) setups.

The accuracy and feasibility of most imaging techniques rely on homogeneous excitation fields and high receiver (Rx) sensitivity. The most efficient method to combine homogeneous excitation with high receiver sensitivity is to use a volumetric coil for transmission (Tx) only and multiple receiver channels (Rx array) for signal reception. Such a transmit-only receive-only (TORO, (Barberi et al., 2000)) system faces technical challenges. In particular, its implementation for preclinical systems and low frequencies adds complexity because of two factors. First: the reduced bore size which limits the number and position of the elements. Second: the high reactive near-field coupling which results in interferences amongst the Rx coils of the array.

In general, coil coupling might reduce the combined SNR of the Rx array and the single channel SNR of the coupled coil elements. Moreover, at lower frequencies (resonance

frequency of  $^{35}\text{Cl}$  at 9.4T is 39.2MHz), the noise is usually coil-dominated (Hoult and Richards, 1976). In this regime, the use of capacitive and inductive decoupling networks might increase the losses in the Rx channels due to the additional electronic components. Likewise, preamplifier decoupling has been shown to be inefficient in terms of SNR loss reduction if coils are strongly coupled and lightly loaded (Malzacher et al., 2016b). To mitigate SNR degradation due to coil coupling despite preamplifier decoupling, additional approaches such as broadband matching and mode matching have been presented before (Brown et al., 2016a; Vester et al., 2012; Wiggins et al., 2012).

In this work we implemented a TORO approach for  $^{35}\text{Cl}$  imaging for the first time to our knowledge (Malzacher et al., 2017). This TORO implementation consisted of a volumetric Birdcage (BC) transmit coil and a 3 element Rx coil array. The Rx array was composed of coils with high and low coupling. We examined the effect of coil coupling on SNR and compared the SNR performance of different decoupling and matching strategies. Finally, the SNR performance of the Rx array was evaluated using the volumetric transmitter coil as reference.

## 3.2 Material and methods

### 3.2.1 Measurement setup

#### 3.2.1.1 Transmit coil

In order to excite the chlorine nuclei, an 8 legged low-pass birdcage coil (Hayes et al., 1985) was designed (Figure 3.1).



**Figure 3.1:** Photograph of the 8-legged low-pass Birdcage coil without the shield.

The Birdcage coil was mounted on a fiberglass reinforced plastic (FRP) tube with an inner diameter of 74.2 mm. The coil structure was shielded using a "Swiss roll" configuration by wrapping copper foil around the coil. The overlapping regions of the copper coil were separated using a thin dielectric material (FR-4) acting as a high capacitance. The total capacitance was calculated to be 4.38 nF using

$$C = \epsilon_0 \epsilon_r \frac{A}{d} \quad (3.1)$$

with  $\epsilon_r = 5.5$ ,  $A = (150 \times 60) \text{ mm}^2$  and  $d = 0.1 \text{ mm}$ .

The shield was mounted on two support rings made of polyvinyl chloride with an outer diameter of 100.2 mm. Variable tuning and matching capacitors were added to a third support ring. The entire coil was covered by an outer FRP tube with an outer diameter of 112 mm which fitted tightly into the gradient insert of the MRI scanner.

The circuit diagram of the Tx 8 leg low-pass BC is depicted in Figure 3.2. This low-pass design was chosen considering the low resonance frequency of interest, since the homogeneous excitation is given by the lowest mode of the coil's spectrum. Moreover, the capacitors were placed at alternating ends of the legs to distribute the current as evenly as possible. The coil was connected to the coaxial cable via a ground ring (Streif et al., 2003) and split matching capacitors in order to balance the coil and to avoid the usage of cable traps.

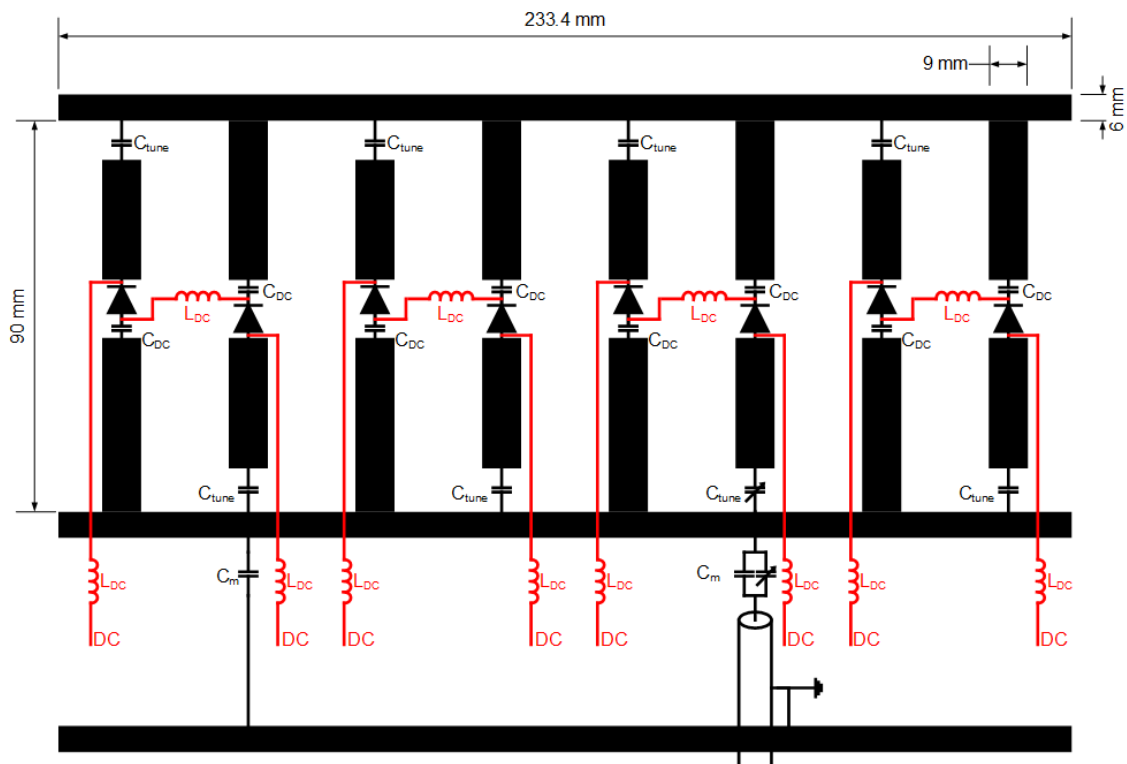


**Figure 3.2:** Circuit diagram of the 8 leg low-pass Birdcage coil. The tuning capacitors are placed at alternating ends of the legs. Detuning is realized by inserting PIN diodes in each leg. Blocking capacitors were added at positions where no tuning capacitors were placed. The Birdcage coil is connected to the system via a ground ring and split matching capacitors.

Active detuning of the coil was realized by adding high power PIN diodes in every leg (see Figure 3.2). The diodes represent an open during Rx phase and a short during Tx phase.

### 3.2.1.2 Receiver array

The receiver array consisted of three identical coils (Figure 3.3 a and b). The coils were built with an outer diameter of 52 mm. Each element was made of a double wound silver-coated copper wire (diameter 1.5 mm) and tuned to the resonance frequency using split tuning capacitors. The coils were equipped with a cable trap (wound semi-rigid coaxial cable with a capacitor in parallel) and a low noise preamplifier (Stark Contrast, optimum NF = 0.7dB, input impedance =  $2+j28\Omega$ , noise match impedance =  $50\Omega$ , gain  $\approx$

27dB). Active detuning was realized using a PIN diode and an inductor in parallel to one split capacitor. For detuning, the PIN diode was shorted to form a parallel circuit with the inductor and the capacitor tuned to the resonance frequency. Additionally, a crossed diode was placed in front of the preamplifier connected from signal to ground for additional preamplifier protection.

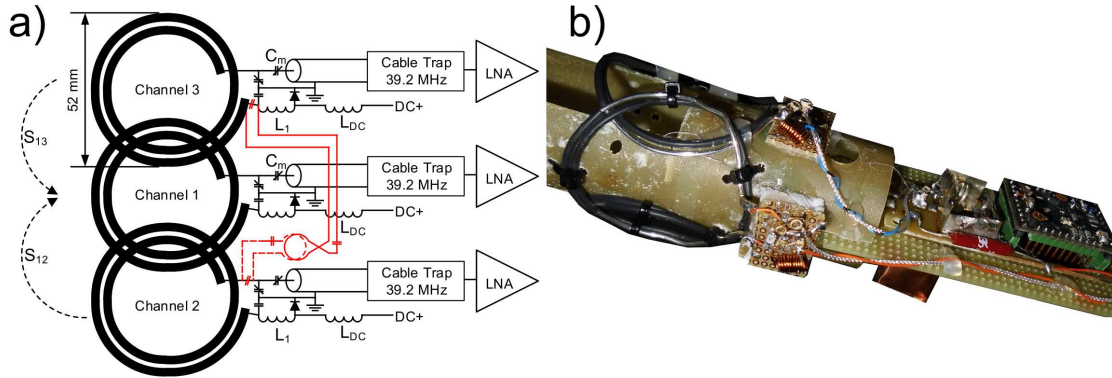


**Figure 3.3:** a) Circuit diagram of the 3 channel Rx array. Each element is equipped with a tuning and matching network, an active detuning unit, a cable trap and a low noise preamplifier. The red lines indicate the transformer decoupling. b) Image of the 3 channel Rx array.

The 3 Rx coils were wrapped around an FRP tube (diameter 42 mm). Nearest neighboring coils were decoupled using overlap decoupling. The configuration's geometry resulted in the two outer Rx elements (Channel 2 and 3, Figure 3.3 b) facing each other. The 3 channel Rx array was designed, firstly, with typical dimensions used for rodent and, secondly, to have a combination of decoupled and coupled coils. This was to investigate the influence of the different decoupling and matching strategies of the coupled coils on the performance of the coils and the array.

## 3.2.2 Decoupling and matching strategies

A common approach to decouple next nearest neighboring coils is preamplifier decoupling (Roemer et al., 1990). Yet, it has been shown before that in some cases SNR performance is degraded despite preamplifier decoupling (Malzacher et al., 2016b; Wiggins et al., 2012). This depends on the combination of the loaded Q-factor and the degree of coupling of the coils. In general, a high loaded Q-factor and strong coupling lead to SNR degradation; however, this has to be evaluated for each array design. Therefore, we compared simultaneously acquired single channel SNR maps using preamplifier decoupling with single channel SNR maps acquired by the single Rx coils standalone.

### 3.2.2.1 Transformer decoupling

There are different approaches to decouple non-nearest neighboring coils using decoupling networks, for example capacitive ladder decoupling networks (Jevtic, 2001) or transformer decoupling (Nabeshima et al., 1996). In our case we implemented the transformer decoupling approach.

In this approach, the Channel 2 and 3 coils were extended each by a transformer in the form of a solenoid coil (Figure 3.3 b, extension of the circuit diagram with red lines). The transformers of the coupled coils were placed directly facing each other but with the

current flowing in opposite directions. The fields of the two transformers canceled out the mutual inductance of the coupled coils, consequently decoupling the coils. An additional series capacitor was added to each transformer adjusted in a way that the two components create a series resonant circuit at the coil's resonance frequency. This prevented frequency shifts and thus the need of retuning the coil.

### 3.2.2.2 Broadband matching and mode matching

Because additional decoupling networks are sometimes challenging to implement concerning the placement of these networks, two methods have been recently suggested to mitigate the SNR degradation of coupled coils despite preamplifier decoupling (Vester et al., 2012). These two methods are broadband matching and mode matching. Vester et al. (Vester et al., 2012) stated that the noise coupling between two coils can be analyzed as the mismatch of the coils' two fundamental eigenmodes, which appear if the two coils are coupled. This noise mismatch can appear despite preamplifier decoupling and can lead to SNR degradation. The broadband and mode matching approaches presented here can both be applied by adjusting the input impedance of the coil using the matching network and the tuning capacitors.

The first method to overcome this mismatch aims to reduce the effective reflection due to coupling between different coils and thus the effective noise figure. The method has already been shown to be feasible in two studies (Brown et al., 2016a; Wiggins et al., 2012). The effective noise factor in a two coil system is given by Brown et al. (Brown et al., 2016a) as:

$$F' = F \cdot \left( \frac{1}{2z} + \frac{z}{2} + \frac{(kQ)^2}{2z} \right) \quad (3.2)$$

$F$  is the noise factor of the preamplifier in isolation.  $k$  is the coupling factor and  $Q$  the  $Q$ -factor of the coils.  $z$  is the impedance ratio of the optimum noise match (in our case  $50\Omega$ ) and the input impedance of the coil presented to the preamplifier. Using the classical matching strategy ( $z = 1$ ) the effective noise factor is  $F' = F \cdot \left( 1 + \frac{(kQ)^2}{2} \right)$ . The optimal matching impedance ratio using the broadband matching approach is (Vester et al., 2012; Wiggins et al., 2012)

$$|z| = |1 + jkQ| \quad (3.3)$$

which reduces the effective noise factor to  $F' = F \cdot \sqrt{1 + (kQ)^2}$ . Nevertheless, since the Rx coil is now sensitive to both modes, the sensitivity to each of these modes is reduced compared to an exclusive match to a single mode.

The coupling factor  $k$  was calculated to  $k = 0.075$  using

$$k = \frac{|f_1 - f_2|}{\sqrt{f_1 \cdot f_2}} \quad (3.4)$$

with  $f_1$  and  $f_2$  the two resonance frequencies of the two appearing modes of the coupled coil pair. The frequencies were measured with the preamplifiers of the coupled coils being unplugged using a double pick-up loop. The absolute impedance was therefore calculated to be  $|z| = 10.5$  with the coils' loaded  $Q$ -factor of 140 (Table 3.1). This resulted in an absolute reflection factor of  $r = 0.83$  using

$$r = \frac{z - 1}{z + 1} \quad (3.5)$$

The input impedance of coil 2 and 3 was now changed individually by adjusting the series and parallel capacitors at the coil input with the other coils detuned. In Figure 3.4 the S-parameters of the reflection measurements of the coil matched to  $r = 0$  and the broadband match with  $r = 0.83$  at the resonance frequency are shown. The impedance circle of the match to  $r = 0.83$  is encircling the center of the smith chart creating a broadband matching of the coil's input impedance.

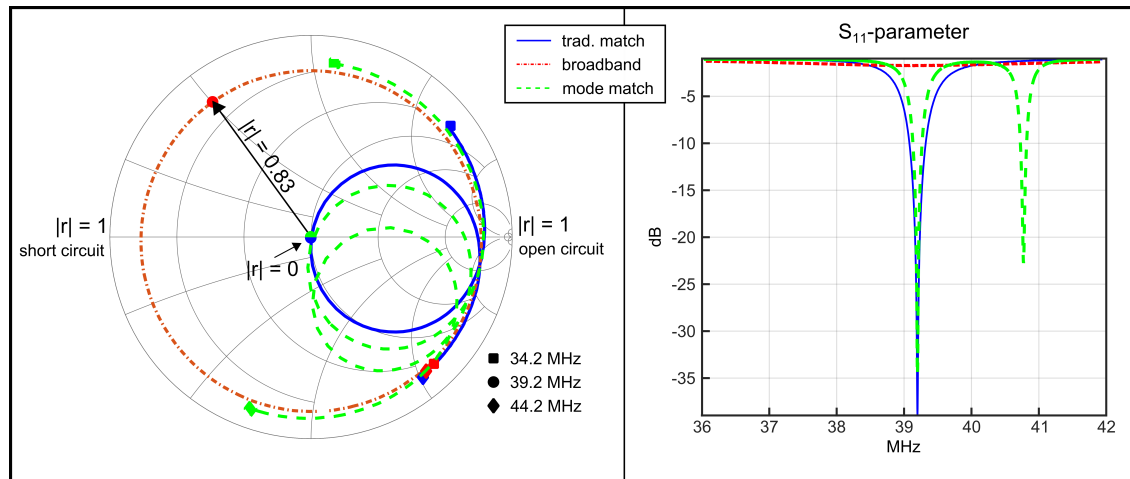


**Figure 3.4:** Reflection S-parameter of the traditional match (blue), the broadband match (red) and the mode match (green) in the Smith chart on the left and in dB on the right.

The second method is mode matching. If there is a single mode of a coupled coils' mode spectrum which is sensitive to the region of interest and which does not shift between different MRI measurements, one of the modes can be purposely selected. The process of finding the sensitive mode is illustrated in Figure 3.5. We depicted the reflection S-parameters measured by a pick-up loop in two positions in between coil 2 and 3. The measurement with the pick-up loop placed in the exact middle between the two coils shows the dominance of the lower mode. Whereas the measurement with the pick-up loop placed close to one of the two coils shows a more dominant higher mode. Since our imaging volume is in the middle of the Rx array our sensitive mode was the lower mode. We continued by adjusting the both coils facing each other iteratively that their lower mode was moved to the resonance frequency. During the adjustments coil 1 was detuned. The resulting reflection S-parameters of one of the coils facing each other are depicted in Figure 3.4.

### 3.2.3 Measurement and sequence parameters

In this work, we performed SNR measurements with the Rx array using preamplifier decoupling, transformer decoupling, broadband matching and mode matching. Additionally, standalone measurements of the single coils as well as measurements with the BC were conducted.

The MR measurements were performed using a preclinical 9.4 T MRI scanner (94/20 Biospec, Bruker, Ettlingen, Germany). A cylindrical phantom with a diameter of 38 mm, a length of 64 mm filled with 0.9% saline solution cooked with 0.05% agar was used. The phantom was placed at a distance of 2 mm to the Rx coils. Measurement data were acquired, firstly, using the Rx array with the different decoupling and matching methods and, secondly, using the transmission coil with the Rx array removed. All

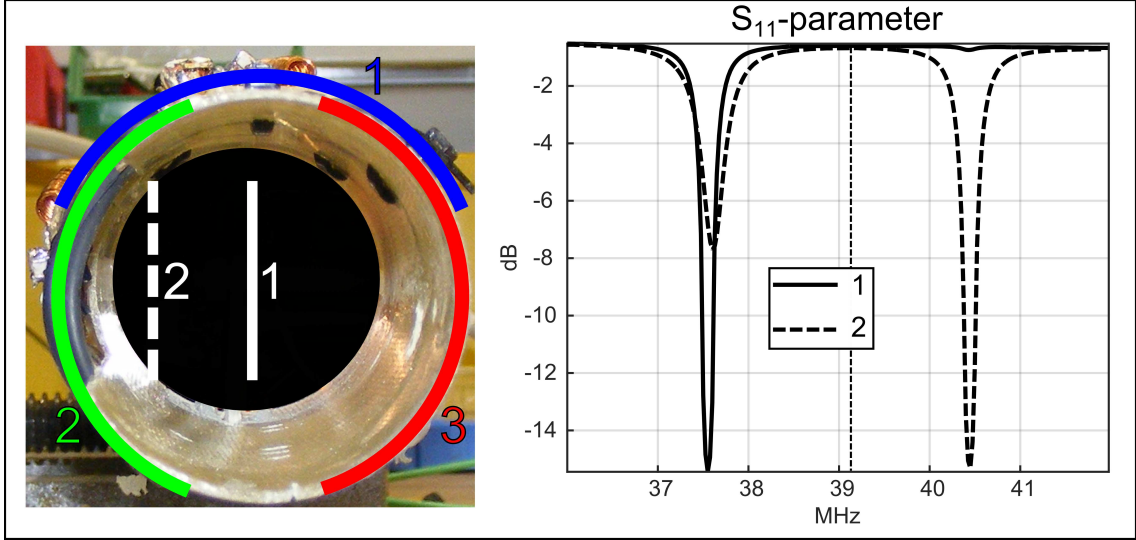


**Figure 3.5:** On the left an axial picture of the Rx array with the 3 Rx coils (1: blue, 2: green, 3: red) and the positions of the pick-up loop. On the right the respective reflection  $S$ -parameters of the two pick-up loop positions.

measurements were performed using an ultra-short echo time sequence (3D radial density-adapted sequence (Hu et al., 2017)). The sequence parameters for the SNR measurements were: Repetition Time/Echo Time = 20/0.3 ms, Flip Angle =  $60^\circ$ , Projections = 3500, Averages = 32, Field-of-View = 50 mm x 50 mm x 50 mm, Isotropic Resolution = 1.5 mm x 1.5 mm x 1.5 mm, Readout Time = 8 ms, Zero-filling Factor 2, Acquisition Time = 37 min.

SNR maps were generated using a separate noise scan with the same sequence parameters without playing an RF pulse for excitation. Combined channel SNR maps were generated using sum-of-squares:

$$SNR = \frac{\sum_i^n iSNR_i \cdot iSNR_i^*}{\sum_{ik} \sqrt{iSNR_i \cdot R_{ik} \cdot iSNR_k^*}} \quad (3.6)$$

with  $iSNR$  the SNR maps of the individual channels and  $R$  the normalized noise correlation matrix.

### 3.3 Results

Table 3.1 shows the measured loaded and unloaded Q-factors of the Rx coils with and without the transformer decoupling network and the Birdcage coil. The Q unloaded to loaded ratio of the Birdcage was approximately one. This indicates that the noise source was mainly coil-dominated. In the case of the two coupled coils, the Q unloaded to loaded ratio was approximately 2. Therefore, the resistance of the coil and that of the load contributed equally to the noise. The Channel 1 coil revealed a lower Q factor and Q factor ratio. This might arise due to additional capacitive losses since this coil shares two overlaps with the other coils.

In Figure 3.6 the SNR maps of the different measurements are shown. For each plot the center transversal plane of the coil was selected. For each measurement the simultaneously

	Channel 1	Channel 2	Channel 2 (trans. dec)	Channel 3	Channel 3 (trans. dec)	Birdcage
<b>Q loaded</b>	128.9	137.8	132.5	142.5	120	55.2
<b>Q unloaded</b>	221.9	285.5	245	285	243.5	59.4
<b>Q unloaded to loaded ratio</b>	1.72	2.07	1.86	2.00	2.03	1.08

**Table 3.1:** Loaded and unloaded  $Q$  factors and  $Q$  factor ratios of the 3 channels of the Rx array and the Birdcage.

acquired single channel maps as well as the combined SNR maps are displayed. The single channel maps in the right column were acquired standalone with the other coils detuned.

Channel 1 coil: This coil is by design decoupled. Neither its profile nor its SNR changed significantly in between the different measurements.

Channel 2 coil and Channel 3 coil: These coils face each other. Their profiles and SNR varied between the different measurements. The coil profiles appear similar in the different measurements except in the mode matching measurement. This was expected since tuning the coils to the lower mode is almost equivalent to a Helmholtz pair but with two separate receiver channels. The broadband matching coil profile therefore can be seen as a combination of the upper and the lower mode. This again looks similar to the original coil profile.

In terms of SNR all different measurements revealed an SNR drop compared to the standalone measurement of the two coupled coils.

The plots of the combined SNR and the reference measurement can be found in the bottom row. Mean SNR values of the measurements with the Rx array compared to the reference scan were higher by a factor of 3.8 for the preamplifier decoupling measurement, higher by a factor of 4.5 for the transformer decoupling and broadband matching measurement and higher by a factor of 4.4 for the mode matching measurement. Finally, SNR profiles taken in the center y and x direction are given at the bottom of Figure 3.6.

Figure 3.7 shows in the top row, the noise levels of the three different receiver channels acquired with the different decoupling and matching methods. The values are scaled to the largest occurring value. Channel 1, which had geometric decoupling, revealed almost no difference within the different measurements. Channel 2 and 3 showed a noise level degradation of approximately 30% for the decoupled, the mode matched and the broadband matched case compared to the preamp decoupled case. The normalized noise correlation matrices can be found in the bottom row of Figure 3.7. The noise correlation value of coil 2 and 3 for the preamp decoupled case is comparably low. The noise correlation is the highest for the mode matched case.

### 3.4 Discussion

In this work, we implemented a TORO RF system consisting of a volumetric Birdcage coil and a 3 channel Rx array for  $^{35}\text{Cl}$  MRI at a 9.4T preclinical MR scanner.

Even though all measurements using the Rx array revealed a major SNR improvement compared to the Birdcage measurement, the mean SNR of the preamplifier decoupling measurement was about 18% lower than that of the other measurements using the Rx array.



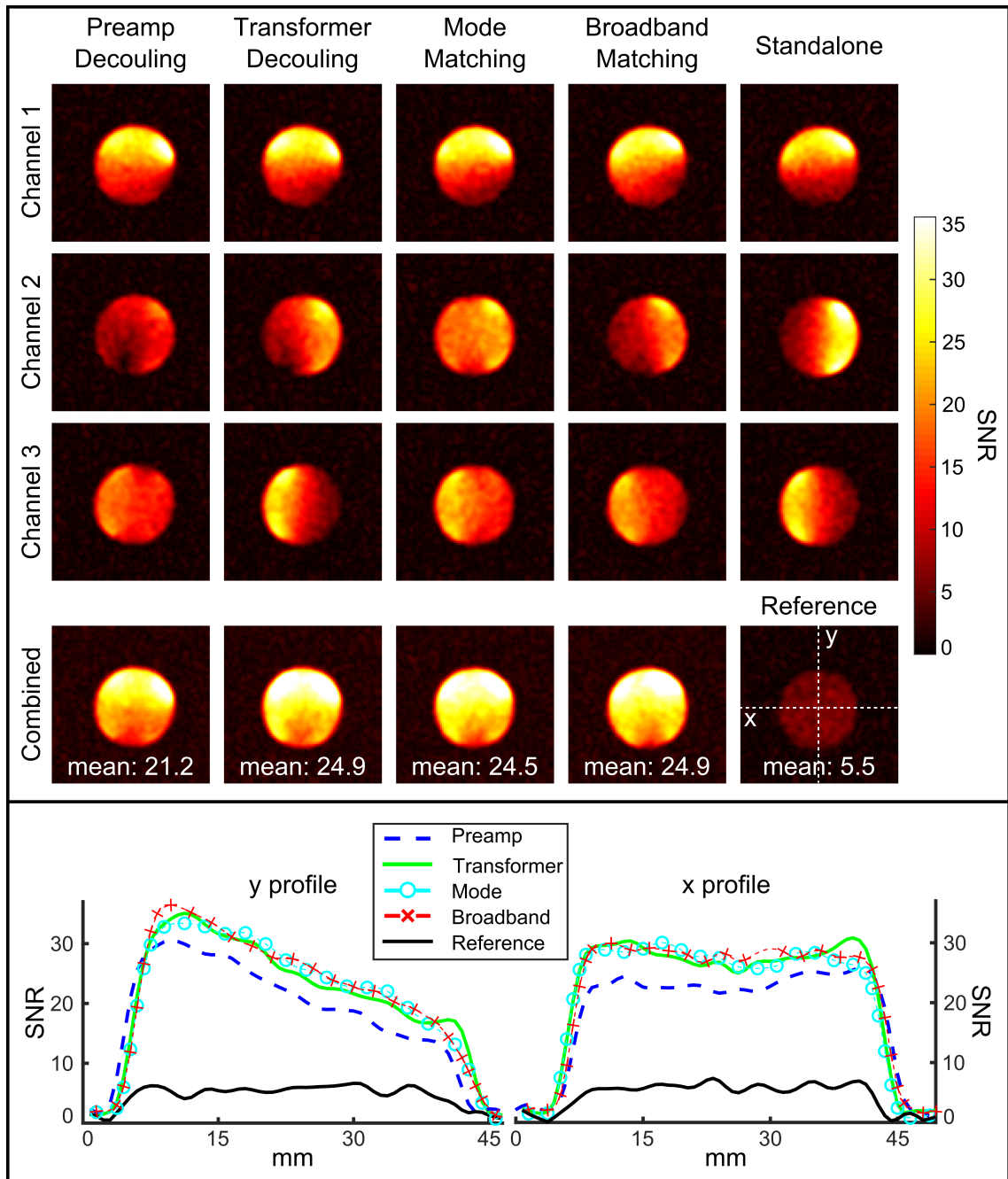


**Figure 3.6:** Single SNR maps of the different measurements as well as the combined SNR maps are depicted. The middle transversal slice is selected. In the last column the single channel SNR maps acquired standalone and the reference SNR map is shown. SNR profiles of the combined SNR maps are given on the bottom. The position of the SNR profiles is shown in the reference SNR map.

Single channel SNR plots revealed that the performance of the coil, which is decoupled in any case, is not affected in any measurements. The SNR performance of the coils facing each other was improved by either use transformer decoupling or mode/broadband matching compared to the measurement utilizing preamplifier decoupling. Yet, the full single channel SNR as achieved by the standalone measurement could not be restored.

In the case of transformer decoupling, one possible reason for the SNR drop is the losses added due to the decoupling network. For the mode matching measurement, a mode

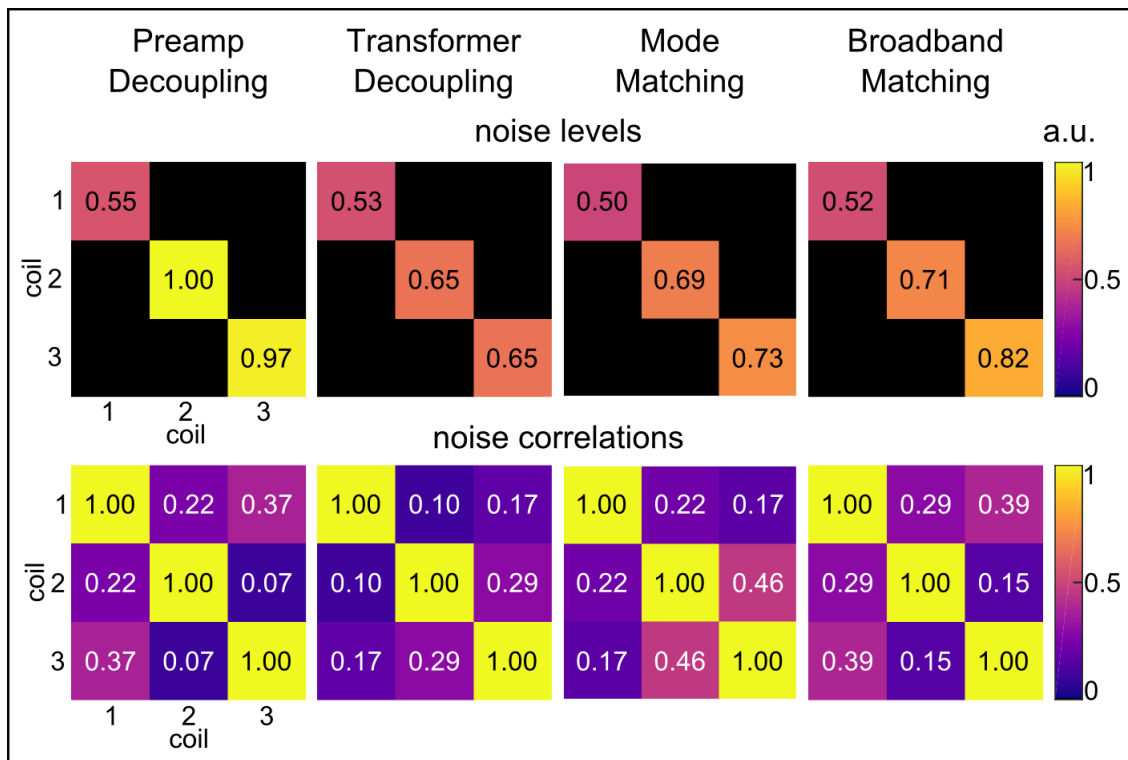


**Figure 3.7:** The noise levels of the individual channels acquired with the different measurements are shown in the top row. The noise values are scaled to the highest value occurring. The respective normalized noise correlation matrices are provided in the bottom row.

was selected, which is sensitive in the middle between the two coupled coils. Therefore, the SNR was only restored at locations reached by the selected mode. The broadband matching measurement was sensitive to both modes but with lower absolute sensitivity to both modes.

The noise levels of the single channels are in agreement with the results of the SNR maps. The noise level of the channel 1 showed almost not change within the different measurements. This is expected since the coil was not changed within the different measurements. Individually, the noise levels of channel 2 and 3 are higher for the preamp decoupled case compared to the noise levels of the other tested methods which aim to decrease the noise of each channel. In contrast, the noise correlation value of channel 2 and 3 for the preamp decoupled case is comparably low although the SNR of these two channels is low. This shows that the noise contribution of the coupled coils is not visible in the normalized noise correlation as it is claimed by Vester et al. (Vester et al., 2012). The noise correlation of channel 2 and 3 is the highest for the mode matched case which is expected since they have a similar coil profile.

In conclusion, SNR degradation despite preamplifier decoupling cannot be neglected for highly coupled coils. In order to determine if SNR degradation occurs, single channel standalone SNR measurements can be compared to simultaneously acquired single channel SNR maps. In the case of the Rx array structure presented here, a total of 3 methods were evaluated, which can mitigate this effect of SNR degradation. Using these methods, single SNR and mean combined SNR could be increased compared to the preamplifier decoupled case. With this SNR increase, we expect to improve image quality for *in-vivo*  $^{35}\text{Cl}$  at 9.4T.

### **3.5 Statement of contribution**

In this study I was responsible for the study design. I built all measurement setups, acquired all measurement data and analyzed and evaluated the measurement data. I did the literature research and wrote the manuscript.



# “Feasibility study of a double resonant ( $^1\text{H}/^{23}\text{Na}$ ) abdominal RF setup at 3T” *Z Med Phys, submitted (06.08.2018)*

---

4

## 4.1 Introduction

In recent years, sodium ( $^{23}\text{Na}$ ) magnetic resonance imaging (MRI) is evolving next to the commonly used proton MRI. Sodium MRI can provide important information about tissue viability and vitality non-invasively (Ouwkerk et al., 2007; Thulborn et al., 1999). Therefore, it is a possible monitoring tool for the effectiveness of radio therapy (Schepkin et al., 2006, 2005). Multiple applications for sodium MRI (Madelin and Regatte, 2013), including diseases in the brain, the heart or the breast are in the scope of current research. Furthermore, abdominal examinations of e.g. the kidney, the prostate, the intervertebral disks, the spinal cord and tumor monitoring are of increasing interest. Studies which focused on sodium MRI of the whole abdomen have been performed recently at 3T (Neumann et al., 2017; Wetterling et al., 2012) and at 7T (Platt et al., 2018).

There are many challenges that need to be overcome for sodium MRI, e.g. motion artifacts due to breathing (Platt et al., 2018) or partial volume effects (Milford et al., 2018; Niesporek et al., 2015). One main challenge is the MR sensitivity of sodium *in-vivo* which is approximately 10 000 times lower compared to proton. To overcome this challenge, research is either moving to higher field strengths or increasing the sensitivity of the RF setups. A common approach to enhance receiver (Rx) sensitivity is to combine a volumetric transmit (Tx) coil with multiple small Rx coils arranged in an Rx array, which is placed in the immediate vicinity of the subject of interest. Such a transmit-only receive-only approach (Barberi et al., 2000) was shown to be feasible for sodium MRI before (Brown et al., 2016a, 2013; Malzacher et al., 2016a; Shajan et al., 2016). Additionally, the possibility to enable proton MRI without the need of exchanging the RF setup is of interest for co-registering the physiological sodium images to the morphology.

The aim of this work was to study the feasibility of a double resonant proton/sodium RF setup for abdominal MRI at 3T. Therefore, a 16-channel sodium Rx array was built to be used in combination with a volumetric sodium Tx Birdcage (BC) (Wetterling et al., 2012). For proton imaging, a proton TxRx coil was added. This proton coil was placed within the sodium Tx coil because of to the shield of the sodium coil. The whole setup was simulated using electromagnetic (EM) simulations. The simulations and the measurements were compared using a phantom. The specific absorption rate (SAR) distribution of the proton coil was calculated for two different human voxel models. Finally, initial sodium and proton MR images of a healthy male 29-year-old volunteer were acquired.

## 4.2 Material and methods

### 4.2.1 EM Simulation

EM simulations were performed for several reasons. First, to determine the geometry of the individual Rx coils of the sodium array for optimal overlap decoupling. Second, for the assurance of the inter-coil compatibility between the sodium array and the proton coil. Third for the performance evaluation of the sodium Rx array compared to the sodium Tx coil. Last to determine the SAR distribution of the proton TxRx coil.

All RF structures were modeled with infinitely thin perfect electrical conductor. Every simulation was performed within a tube (diameter = 684 mm, length = 1300 mm) mimicking the MR system.

#### 4.2.1.1 Phantom simulation

Simulations were performed using the frequency domain Finite-Element-Method (FEM) solver (CST Computer Simulation Technology GmbH, Darmstadt, Germany) based on a tetrahedral mesh. This solver is compatible with a tetrahedral mesh, which is more appropriate to simulate complex and bent structures due to the nature of its generation. Therefore, the iterative optimization process of the Rx array coils could be performed faster. Models of the CST simulation are depicted in Figure 4.1.

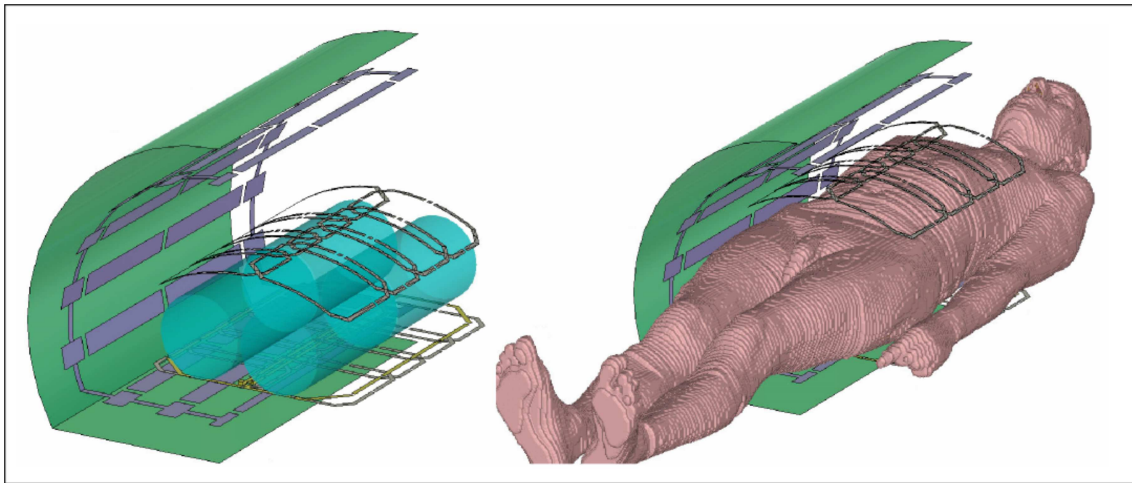


**Figure 4.1:** CST setups for the EM simulations. Left: setup for the phantom simulations, right: setup for the human model simulation with the Gustav model.

The sodium BC coil model was shaped as described in (Wetterling et al., 2012). It comprised 16 legs, each leg with a conductor width of 30 mm and a length of 515 mm. Five legs were placed horizontally to fit in the patient table. The other legs were placed as it is done in a conventional BC (Hayes et al., 1985). Each leg was split two times for the tuning capacitors. For detuning, a PIN diode was added in the middle of each leg. In the simulation, the PIN diodes were modeled with 5 nF in the tuned state and 1 pF in the detuned state. The width of the end-rings was 10 mm. They were placed with a distance of 20 mm to the end of the legs. Feeding ports for the quadrature drive were placed at the first and the last horizontal leg. The shield (length = 515 mm) was placed with a distance of 50 mm to the coil structure.

The  $^{23}\text{Na}$  Rx array was split into a lower and an upper part. Each part comprised 8 single  $^{23}\text{Na}$  Rx coils. The coils were arranged in an 'olympic' like configuration as depicted in Figure 4.2. This configuration provided sufficient decoupling for nearest neighboring coils. The lower part of the  $^{23}\text{Na}$  Rx array was flat while the upper part was bent to adapt to the human abdominal geometry. All single  $^{23}\text{Na}$  Rx elements were simulated without preamplifier and DC electronic components. The conductor width was 6 mm. Each element's corners were flattened to minimize capacitive coupling at the overlapping points. Individual coil geometries were optimized for optimal decoupling as described in the following. The total size of the flat array was set to a length of 378 mm and a width of 300 mm. The approximate size of the individual elements was initially calculated using an overlap of 10% (Roemer et al., 1990) of the coil size. At first, the large coil, which is placed at one end of each row of the array, was modeled and tuned to the resonance frequency. Then the second coil in the row was modeled and tuned as well with the initial coil off-resonant. Afterwards, both coils were simulated simultaneously and the coil width was iteratively changed until a decoupling below -15 dB was achieved.

The first coil of the second coil was modeled and tuned with the dimensions and capacitor values found by simulating the first two coils. Then, the length of the elements was iteratively changed until a decoupling of all three coils below -15 dB was reached. Finally, the array was completed with the missing coils using the dimensions and capacitor values from the simulations before. The bent part of the array was built with the same dimension as for the flat part. Detuning of the Rx array elements for the  $^1\text{H}$  simulation was realized as described in (Malzacher et al., 2018). To avoid any influence of the  $^1\text{H}$  coil on the sodium array, each Rx element was equipped with a proton trap. This trap was realized as a two-staged approach (I Mispelter et al., 2006) as depicted in Figure 4.2. The value of the inductor was set to 150 nH and the capacitor values were calculated using

$$C_{par} = \frac{1}{L\omega_{Na}^2} \quad (4.1)$$

$$C_{ser} = \frac{1}{L(\omega_H^2 - \omega_{Na}^2)} \quad (4.2)$$

with L the inductance value,  $C_{par}$  the parallel capacitor,  $C_{ser}$  the serial capacitor,  $\omega_H$  the proton frequency and  $\omega_{Na}$  the sodium frequency. The simulated reflection and transmission S-parameter are depicted in Figure 4.3. This type was chosen since it presented low input resistance at the sodium frequency and low transmission at the proton frequency. The series resonance circuit which is 'seen' by the coil at the sodium frequency avoided the need of retuning the coil after insertion of the trap.

The  $^1\text{H}$  TxRx coil was built as a single butterfly (Bottomley and Hardy, 1990) coil with the following dimensions: length = 400 mm, width = 278 mm. It was split into 24 parts to ensure an even current distribution. The  $^1\text{H}$  coil was placed above the lower part of the  $^{23}\text{Na}$  Rx array separated by a PVC layer (thickness = 2 mm). The sodium BC was initially not designed to be proton compatible. In order to protect the PIN diodes, which were placed in series to the legs, they had to be driven by a DC current. Therefore, the sodium BC stayed resonant during the  $^1\text{H}$  simulations and measurements.

Four bottle shaped phantoms (diameter = 115 mm, length = 205 mm) filled with saline solution ( $\epsilon_r = 80$ ,  $\sigma = 0.9 \frac{\text{S}}{\text{m}}$ ) were used to load the coils. The phantom's properties were

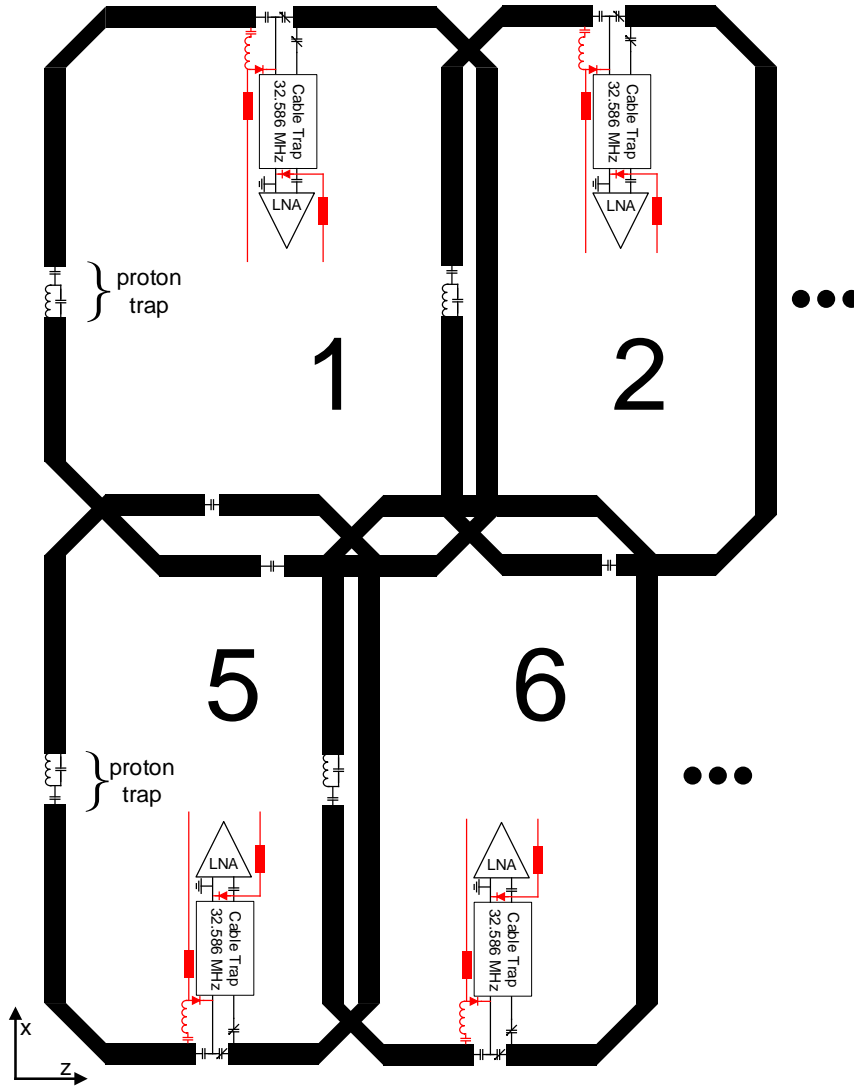


**Figure 4.2:** Electrical circuit diagram of a part of the array. Each coil was equipped with a proton trap and an active detuning network.

selected to match the phantoms used for the measurements.

The following simulations were performed:

- (1)  $^{23}\text{Na}$  BC standalone
- (2)  $^{23}\text{Na}$  Rx array with the detuned  $^{23}\text{Na}$  BC and the resonant  $^1\text{H}$  coil
- (3)  $^1\text{H}$  coil with the resonant  $^{23}\text{Na}$  BC and the detuned  $^{23}\text{Na}$  Rx array

All simulations were performed at their respective Larmor frequency ( $f_{23\text{Na}} = 32.586$  MHz and  $f_{^1\text{H}} = 123.2$  MHz) with a bandwidth of 10 MHz. Mesh adaption was performed at the respective frequency with a stop criterion of 0.02 S-parameter difference between iterative solver runs. After the mesh refinement, the bandwidth was sampled at 11 equidistant frequency points. Finally, automatic frequency points were sampled until the



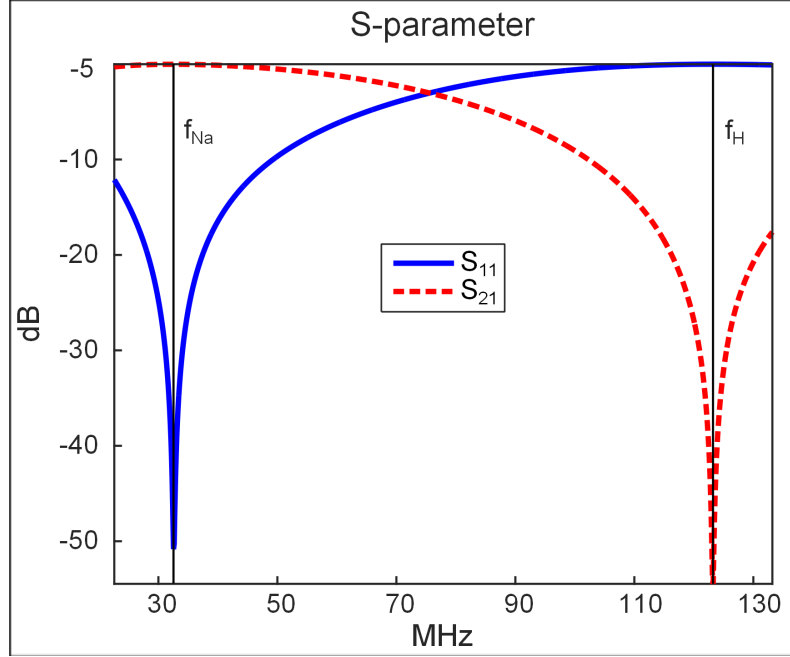


**Figure 4.3:** Reflection (solid blue line) and transmission (dotted red line) S-parameter of the proton trap.

maximum deviation of the linear S-parameters between two successive frequency points was below 0.02.

Tuning and matching for the  $^{23}\text{Na}$  BC and the  $^1\text{H}$  coil were performed using the CST co-simulation (Kozlov and Turner, 2009). The channel combination of the  $^{23}\text{Na}$  Rx array was done based on (Schnell et al., 2000; Stumpf et al., 2018).

#### 4.2.1.2 Human model simulation

Additional human model simulations were performed to determine the SAR of the  $^1\text{H}$  TxRx coil. The SAR simulations were performed using the Finite-Difference-Time-Domain (FDTD) solver with CST based on a hexahedral mesh. This solver was used for the SAR simulations since human models are mostly available only for hexahedral meshing. SAR distribution was calculated using the IEEE/IEC 62704-1 norm. The following formula was used for the calculation

$$SAR = \frac{\sigma}{2\rho} \|E\|^2 \quad (4.3)$$

with  $\sigma$  the material conductivity,  $\rho$  the mass density of the material and E the magnitude of the E-field.

The human voxel models used were the male Gustav and the female Laura model from the CST voxel family. The voxel size of the Gustav model was  $(1.7 \text{ mm})^3$  isotropic and the voxel size of the Laura model was  $(1.875 \times 1.875 \times 1.5) \text{ mm}^3$ . The local mesh of the proton coil was set to 1.5 mm, of the sodium BC to 5 mm and of the sodium Rx coils to 2 mm. The background mesh was set to 15 cells per wavelength. The frequency range of the simulations was 0 to 133.2 MHz. The stop criterion for the solver was set to a steady state of -50 dB.

## 4.2.2 Hardware

### 4.2.2.1 $^{23}\text{Na}$ RF coils

The  $^{23}\text{Na}$  transmission coil used for the measurements was the coil presented in (Wetterling et al., 2012).

The individual elements of the  $^{23}\text{Na}$  array were built with the dimensions found in the simulations (Figure 4.4). One tuning capacitor of each coil was split to generate a virtual ground. At this position, the coil was tuned and matched to the resonance frequency. A cable trap was placed between the matching network and the preamplifier. Detuning was realized using an active detuning circuit comprised a PIN diode, an inductor and one of the split capacitors. An additional PIN diode was put in front of the preamplifier for additional protection. The PIN diodes were fed via  $15\ \mu\text{H}$  inductors to block RF current to flow into the DC line. The inductors for the detuning circuit and the proton traps were self-wound inductors made of enameled copper wire. The proton traps were soldered and adjusted on a separate FR4 piece and added to each coil after they were tuned and matched. Final readjustment of the coils was done to compensate for small occurring frequency shifts. Finally, the coils were arranged as in the simulations and checked for overlap decoupling. The lower part of the array was but inside a PVC housing. The upper part of the array was mounted on a bent PVC plate. Tuning and matching was checked again after adding the  $^1\text{H}$  TxRx coil.

### 4.2.2.2 $^1\text{H}$ TxRx coil

In order to enable the use of the local proton TxRx coil, a frequency splitter and a proton TxRx switch (Stark Contrast GmbH) were used. The proton coil was built as in the simulation. It was tuned and matched via a lumped element matching network and connected to the TxRX switch via a proton cable trap. The coil was put on top of the housing of the lower Rx array and covered by a synthetic pad (thickness = 5 mm). Adjustment of the coil was performed with the sodium Rx array elements detuned and the BC coil resonant.

## 4.2.3 Sequence for phantom and *in-vivo* imaging

Sodium imaging was performed using a 3D density adapted radial sequence (Nagel et al., 2009) with the following parameters for phantom measurements: TE/TR/TA = 0.54 ms / 24 ms / 3:42 min, FoV = 450 mm, isotropic resolution =  $(6\ \text{mm})^3$ , flip-angle =  $60^\circ$ , projections = 17 670. An additional noise measurement was performed with the same sequence parameters but no Tx power applied. This was done for the channel combination (Schnell et al., 2000) and to generate SNR maps. The sequence parameters for the *in-vivo* measurements were: TE/TR/TA = 0.36 ms / 24 ms / 30 min, averages = 5, FoV = 360 mm, isotropic resolution =  $(4.5\ \text{mm})^3$ , flip-angle =  $60^\circ$ , projections = 15 000. Noise measurements for the channel combination were performed with the same parameters but without Tx power and a factor 10 less projections.

Proton images were acquired using an abdominal localizer sequence.

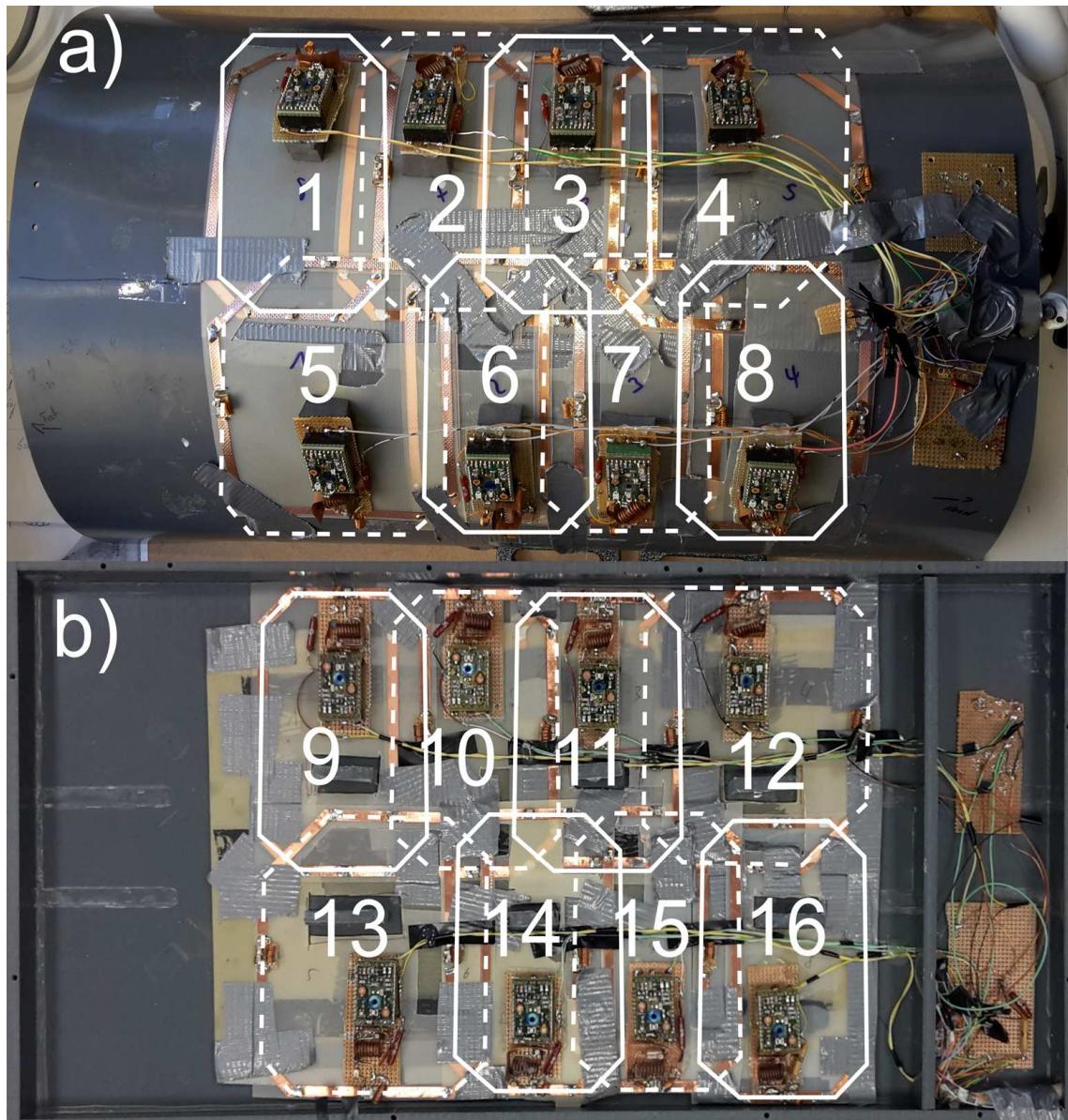


**Figure 4.4:** Images of the sodium Rx arrays. The cover of the lower part was removed for taking the image.

## 4.3 Results

### 4.3.1 Phantom simulation and SAR results

The ratio (Rx array/Birdcage) of the simulated B-1-fields for the sodium Rx array and the sodium Birdcage is given in Figure 4.5. The B-1 sensitivity of the Rx array was about a factor 3 higher in the middle of the phantom and up to a factor 6 higher in the periphery of the phantom which is in the vicinity of the Rx array coils.

The mean SAR was 0.0063 W/kg for the Laura model and 0.0057 W/kg for the Gustav model normalized to 1 W accepted power. The mean was calculated within the  $^1\text{H}$  Tx coil dimensions. The peak SAR values were 0.59 W/kg for the Laura model and 0.70 W/kg for the Gustav model normalized to 1 W accepted power.

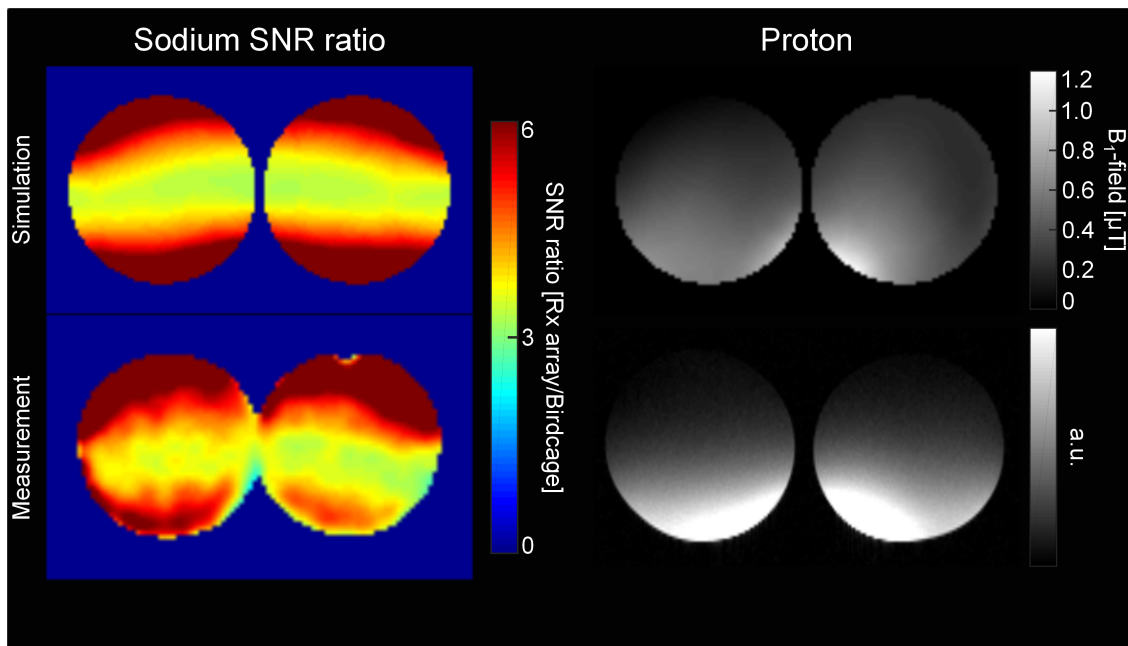


**Figure 4.5:** Phantom simulation and measurement results in a sagittal slice for the sodium and proton coils.

## 4.3.2 Measurement results

### 4.3.2.1 Phantom results

The measured sodium SNR ratio (Rx array/Birdcage) using the phantom measurements are given in Figure 4.5. The SNR distribution, as well as the SNR ratio values, was similar compared to the simulations. The simulated proton B<sub>1</sub>-field, as well as the measured proton image, revealed a similar coil profile.

The measured noise correlation matrix of the Rx array is depicted in Figure 4.6. A higher noise correlation can be observed for the upper bent part of the array compared to the lower flat part. The noise correlation between the two parts was low.

### 4.3.2.2 *In-vivo* results

Sodium and proton *in-vivo* images of a 29-year-old healthy volunteer are plotted in Figure 4.6. The images are given in arbitrary units since the noise scan for the Rx array was reduced and no noise scan was performed for the proton images. In the selected slices the kidneys, the heart, intervertebral disks and the spine can be seen.

## 4.4 Discussion

The feasibility of a double resonant proton/sodium RF setup for MRI at 3T was evaluated using EM simulations and MR measurements of a phantom and a volunteer.

The simulations as well as the measurements in the sodium case revealed an SNR improvement of a factor 3 to 6 compared to the volumetric transmit coil. This was expected since the Rx array was placed in the immediate vicinity of the phantom. The phantom was smaller compared to the human abdomen which decreases the SNR gain in the middle of the abdomen. Nevertheless, the gain in the vicinity of the coils will stay the same.

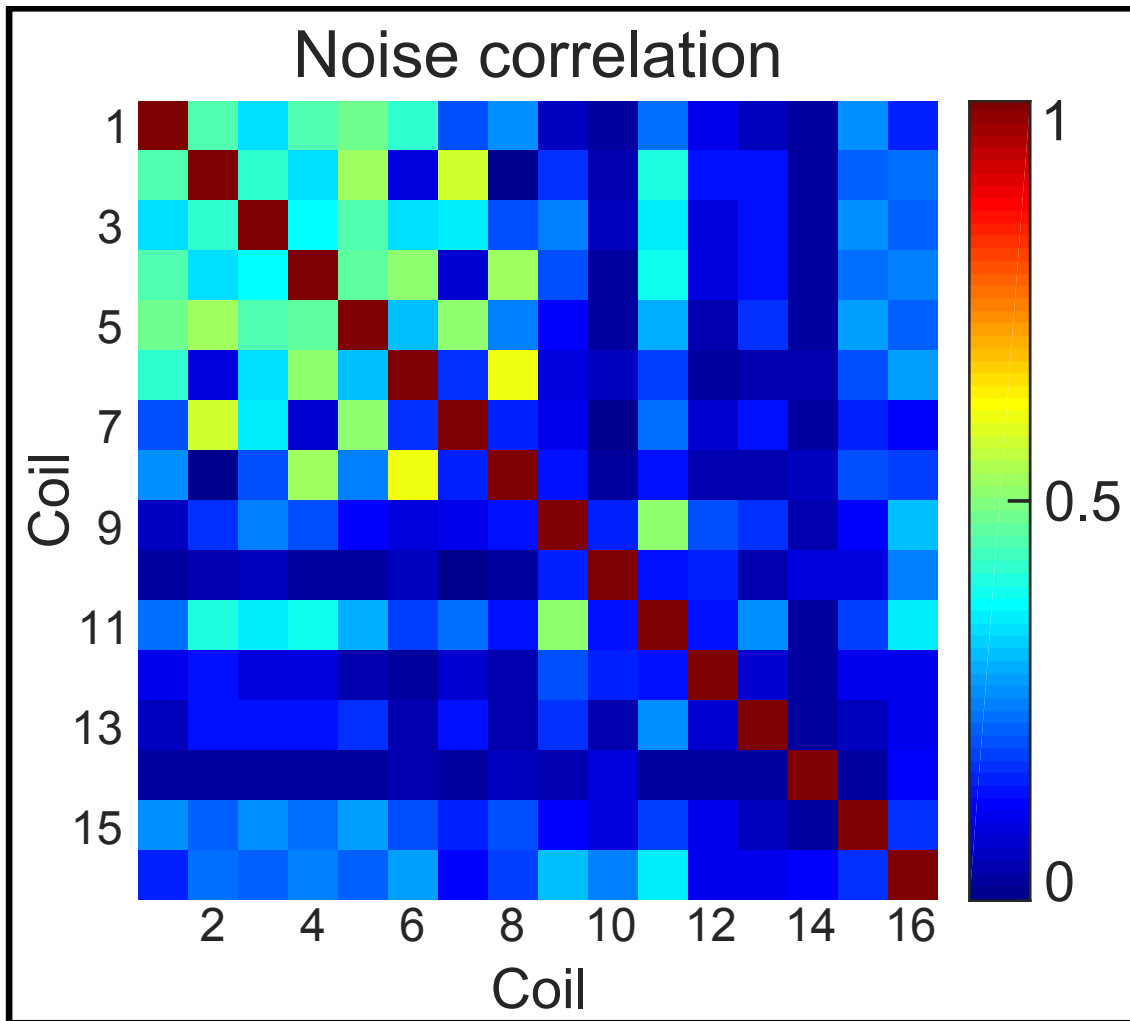


**Figure 4.6:** Noise correlation matrix of the sodium Rx array.

*In-vivo* MR images were acquired with an isotropic resolution of  $(4.5 \text{ mm})^3$  within an acquisition time of 30 minutes. Similar sequence parameters were used before in another study for abdominal sodium imaging at 7T (Platt et al., 2018) with comparable image quality. The mentioned study introduced additionally a breathing correction by reconstructing the measurement data in the inhaled and exhaled state separately. Such a correction can further increase image quality. Nevertheless, this was not considered here since we only focused on the feasibility of such a hardware setup.

To enable additional proton imaging, a local TxRx proton coil was added within the sodium setup. It was not possible to use the system's proton Tx coil due to the shield of the sodium Tx coil. The shield is necessary since it decreases noise due to eddy currents. This poses challenges to enable proton imaging. Due to the limited space of the sodium Tx coil and the sodium Rx arrays the positioning of the proton coil was limited. We choose to put the proton coil on top of the sodium spine array since at this position the coil was least affected by body motion. We did not choose to put an additional proton coil on the top part of the sodium array since matching and tuning of the coil was found to be almost impossible due to body motion. Future research may focus on more sophisticated approaches for proton imaging within the sodium Tx coil

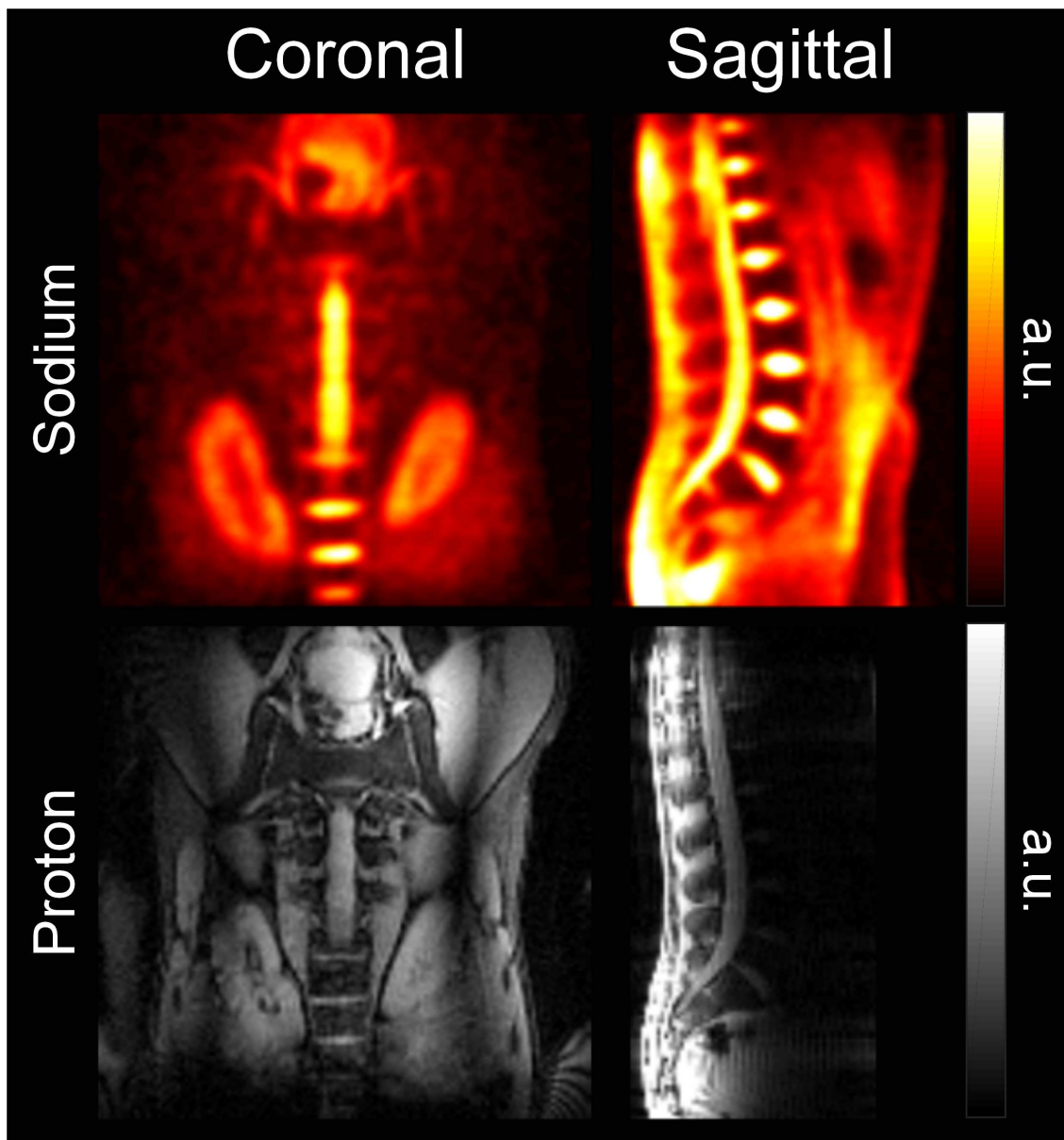


**Figure 4.7:** Sodium and proton images of a 29-year-old healthy volunteer in a coronal and sagittal slice.

## 4.5 Conclusion

The concept of a double resonant RF structure comprised of a shielded sodium Tx Birdcage coil, a sodium Rx array and a local proton TxRx coil for abdominal MRI was proven to be feasible. Using a sodium Rx array substantially increased the sodium SNR. Proton imaging could be enabled using a local TxRx coil.

## 4.6 Statement of contribution

In this study I was responsible for the study design. I built all measurement setups, modeled all simulation setups, acquired all measurement and simulation data and analyzed and evaluated the measurement and simulation data. I did the literature research and wrote the manuscript.

“Feasibility study of a double resonant  
 $^1\text{H}/^{23}\text{Na}$  16-channel receive-only head coil  
at 3T” *Magn Reson Imaging, submitted*  
(20.08.2018)

5

---

## 5.1 Introduction

Sodium ( $^{23}\text{Na}$ ) magnetic resonance imaging could be used by clinicians as an additional diagnostic tool next to conventional proton MRI. Besides different applications in the body (Madelin et al., 2014; Neumann et al., 2017; Platt et al., 2018; Wetterling et al., 2012), brain applications as e.g. stroke, tumor, multiple sclerosis, and Alzheimer (Madelin and Regatte, 2013) are especially increasingly interesting since sodium MRI can give additional information about tissue viability and vitality (Schepkin et al., 2006, 2005).

Nevertheless, sodium MRI is challenging due to its fast relaxation times and low MR sensitivity (approximately 10 000 times lower compared to proton ( $^1\text{H}$ ) *in-vivo*). In order to overcome these challenges, the use of special sequences (Boada et al., 1997; Nagel et al., 2009; Pipe et al., 2011), post-processing techniques (Milford et al., 2018; Niesporek et al., 2015; Platt et al., 2018) and dedicated radio frequency (RF) setups (Wiggins et al., 2016) is crucial. One additional requirement for the hardware, shall it be used in the clinical routine, is a combination of high sodium sensitivity and full proton imaging performance (high signal-to-noise ratio (SNR) and parallel imaging capability). Due to scan time limitations (e.g. in case of stroke) and for patient comfort, this should be provided using a single RF setup to avoid the need to exchange the coil setup.

Many different approaches for a double resonant coil setup have been presented before (Brown et al., 2016a,b, 2013; Ha et al., 2010; Han et al., 2017; Lakshmanan et al., 2018; Shajan et al., 2016). Nevertheless, one common drawback of these approaches has been that the  $^1\text{H}$  performance of these coils has been limited to the acquisition of morphological images. This has been often due to the use of transceiver arrays with small coils for  $^1\text{H}$  imaging.

A commonly used technique for homogeneous excitation and high receiver (Rx) sensitivity is the transmit-only receive-only (ToRo) approach (Barberi et al., 2000) which has been shown to be feasible for different sodium RF setups in previous works (Brown et al., 2016a, 2013; Malzacher et al., 2016a; Shajan et al., 2011).

The aim of this work was to build a double resonant 16-channel Rx head array for MRI at 3 T with high sodium sensitivity and full proton imaging performance. In order to evaluate the feasibility of such setup, sodium SNR performance was compared to a commercially available sodium head coil. Additionally, SNR, as well as parallel imaging performance for proton was evaluated against a commercially available proton Rx head array. Both comparisons were performed using phantom measurements. Finally, initial volunteer sodium and proton MR images were acquired.

## 5.2 Material and methods

### 5.2.1 Sodium array

A circuit diagram of the double resonant Rx coil and a 3D model of the coil are depicted in Figure 5.1. The sodium coil was built as a degenerate Birdcage (DGB) coil (Leussler et al., 1997). This structure is a conventional band-pass Birdcage (Hayes et al., 1985) but the capacitors in the legs are adjusted in a way that the different modes of the Birdcage collapse. The DGB resulted in 8 independent Rx channels. The coil structure was made of flat copper conductor (width = 6mm, thickness = 0.1mm) and mounted on a PVC tube with an outer diameter of 250 mm. The dimensions of the single coils were in x-direction 98 mm and in z-direction 240 mm. The single coils were split by capacitors at four positions, two in the ring segments and two in the legs. The capacitors in the legs were used to decouple nearest neighboring coils. The capacitors in the ring segments were used to tune the individual coils. One of the tuning capacitors was split to generate a virtual ground. At this position the preamplifier (Stark Contrast GmbH) was connected via a capacitive matching network. A sodium cable trap was positioned between the coil and the preamplifier. The trap was made of wound coaxial cable bridged by a capacitor and shielded with copper tape. A proton trap was added to each leg and every second ring segment of the DGB. This was done to avoid interactions between the sodium and the proton Rx array as well as protect the sodium Rx coils during the proton transmit phase. The two-stage trap design was chosen (I Mispelter et al., 2006). It comprised an inductor bridged by a capacitor and an additional capacitor in series. The inductor was made of wound enameled copper wire. The inductor value was set to 300 nH. The value of the capacitor in parallel to the inductor ( $C_{par}$ ) and the capacitor in series ( $C_{ser}$ ) was calculated using

$$C_{par} = \frac{1}{L\omega_{Na}^2} \quad (5.1)$$

$$C_{ser} = \frac{1}{L(\omega_H^2 - \omega_{Na}^2)} \quad (5.2)$$

with  $\omega_{Na}$  the sodium Larmor frequency and  $\omega_H$  the proton Larmor frequency. This design was chosen since it presents high impedance at the blocking (proton) frequency and low impedance at the resonance (sodium) frequency. This avoids the need of retuning the coil after insertion of the trap circuit.

The structure of the sodium coil was first modeled for EM simulations (CST Computer System Technology GmbH, Darmstadt, Germany) to obtain the values of the capacitors roughly. The DGB was then constructed iteratively. Each coil was first tuned to the sodium resonance frequency. Then the proton traps were added consecutively. After the



insertion of a trap circuit, the resonance frequency of the coil was readjusted to the initial resonance frequency if a frequency shift occurred. This was done by changing the value of the series capacitor of the trap circuit.

After the insertion of the traps, the coil was decoupled from its neighbors by adjusting the capacitor in the common leg. This was done using transmission S-parameter measurements. Afterwards, each coil was tuned and matched and preamplifier decoupling was adjusted by varying the series and parallel capacitor of the matching circuit. This process was repeated for each channel. Finally, all individual channels were re-adjusted while the other coils were resonant and equipped with a preamplifier.

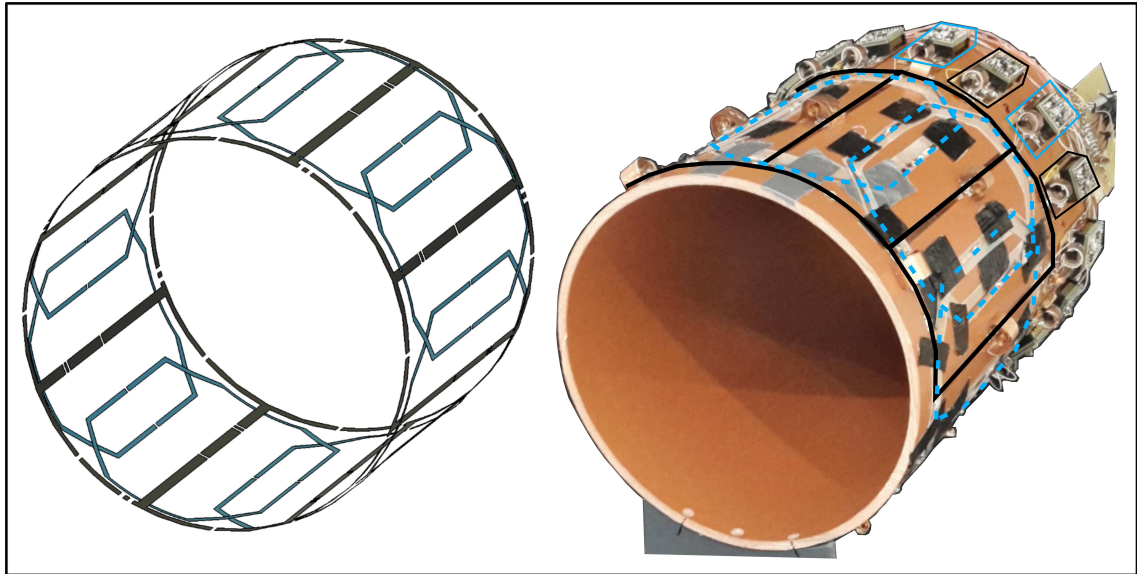


**Figure 5.1:** 3D model of the coil on the left and image of the coil on the right. The sodium array in black and the proton array in blue.

In order to reduce SNR losses due to coil coupling, the Rx coils were matched in a broadband fashion (Vester et al., 2012). The highest coupling was found between the next nearest neighboring coils. The two frequencies of the coupled coils were measured with both coils resonant without preamplifier and the other coils detuned using a double pick-up loop (Darrasse and Kassab, 1993). The coupling coefficient  $k$  was calculated using

$$k = \frac{|f_1 - f_2|}{\sqrt{f_1 \cdot f_2}} \quad (5.3)$$

with  $f_1$  the frequency of the upper mode and  $f_2$  the frequency of the lower mode. The optimum broadband matching impedance was then calculated using

$$|z| = |1 + jkQ| \quad (5.4)$$

with  $Q$  the loaded Q-factor of a single sodium coil. The reflection factor for the sodium coil resulted in  $r = 0.24$  with a loaded Q-factor of 140. The sodium coils were matched to this reflection factor at the resonance frequency with the impedance circle of the reflection S-parameter encircling the center of the smith chart (Brown et al., 2016a; Malzacher et al., 2018).

At last an active detuning circuit was added to each coil consisting of a PIN diode and an inductor made of wound enameled copper wire.

## 5.2.2 Proton array

The proton Rx array consisted of 8 single Rx coils. The dimensions of the single coils were in x-direction 131 mm and in z-direction 216 mm. The individual coils were decoupled using overlap decoupling. The coils were built in an octagonal shape to decrease capacitive coupling at the overlap positions. The coil's size in z direction was shorter compared to the sodium DGB to avoid large overlapping areas of the conductors. This was done to decrease capacitive coupling between the sodium and the proton coils. The geometry of the proton coils in terms of overlap was found iteratively using EM simulations. In order to find the optimal overlap two proton coils were simulated with a 45° shift to each other (in the middle of the coils) on top of the detuned sodium DGB. Both were tuned to the Larmor frequency of proton. Then the width of both coils was changed consequently until a decoupling of at least -15 dB was found.

For the measurement setup the coils were made of flat copper tape (width = 3 mm, thickness = 0.1 mm). Each coil was split four times by a capacitor. One of the capacitors which were placed at the end of the coil in z-direction was split to generate a virtual ground. At this point, the coil was connected to the preamplifier (Siemens Healthcare GmbH) via a capacitive matching network. A proton cable trap was placed between the coil and the preamplifier. The cable trap was built as described for the sodium coils. Each coil was built on a flexible FR4 board (thickness = 0.2 mm) and tuned to the resonance frequency. The coils were placed on top of the legs of the sodium DGB (Figure 1). The overlap distance was checked for optimum decoupling using transmission S-parameter measurements. During the mounting process the sodium DGB was detuned (as it is during the proton measurement). Highest coupling was found between next neighboring elements. The optimum matching impedance was found as described for the sodium DGB. The reflection factor was calculated to be  $r = 0.56$  with a loaded Q-factor of 120.

Additionally, each coil was equipped with a PIN diode driven detuning network. Finally, the elements of the sodium DGB were readjusted when needed with the proton array detuned.

## 5.2.3 Measurements

### 5.2.3.1 Phantom

All measurements were performed on a clinical 3T Tim Trio MR system (Siemens Healthcare GmbH). Phantom measurements were performed using a bottle shaped phantom (diameter = 115 mm, length = 205 mm) filled with 3.75 NiSO<sub>4</sub>·6H<sub>2</sub>O+5g NaCl. For each SNR scan a noise measurement was performed with the same sequence parameter but without transmit (Tx) power. The single channel SNR maps were combined using the matched filter approach (Schnell et al., 2000).

### *<sup>23</sup>Na imaging*

Sodium images were performed using a 3D density adapted radial sequence (Nagel et al., 2009) with the following parameters: TE/TR/TA = 1 ms/100 ms/4 min, flip angle = 48°, FoV = 250 mm, isotropic resolution = (6 mm)<sup>3</sup>, projections = 2500.

For <sup>23</sup>Na transmission, a <sup>1</sup>H compatible linear polarized Helmholtz coil (Rapid Biomedical) was used. For reference, images a circular polarized double resonant <sup>1</sup>H/<sup>23</sup>Na head Birdcage coil (Rapid Biomedical) was used.

### <sup>1</sup>H imaging

Proton images were acquired using a gradient echo sequence with the following parameters: TE/TR/TA = 10 ms/100 ms/20 s, FoV = 250 mm, flip angle = 90°, resolution = 1x1x5 mm<sup>3</sup>. For <sup>1</sup>H transmission, the systems transmit coil was used. A reference measurement was performed using a 12-channel head Rx coil (Siemens Healthcare GmbH).

In order to evaluate parallel imaging performance, g-factors were calculated using the SENSE formalism on the images acquired with the commercial coil and with the double resonant coil.

#### 5.2.3.2 *In-vivo*

All methods were performed according to the relevant guidelines and regulations. The *in-vivo* head scans were approved by the local Institutional Review Board and acquired with prior written informed consent. *In-vivo* images were acquired of a healthy 32 year-old male volunteer.

### <sup>23</sup>Na imaging

The same 3D density adapted radial sequence as for the phantom measurements were used with the following parameters: TE/TR/TA = 0.74 ms/32 ms/8 min, flip angle = 60°, FoV = 250 mm, isotropic resolution = (5 mm)<sup>3</sup>, projections = 7500, averages = 2. The noise scan for channel combination was performed with the same parameters but a factor 10 less projections and no Tx power applied.

### <sup>1</sup>H imaging

A T<sub>1</sub> weighted multi-slice FLASH sequence was applied with the following parameters: TE/TR/TA = 2.42 ms/450 ms/2.25 min, FoV = 230x320 mm<sup>2</sup>, resolution = 0.7x0.7x3 mm<sup>3</sup> and GRAPPA with reduction factor =2.

Additionally a T<sub>2</sub> weighted multi-slice multi-shot turbo spin echo sequence was applied with the following parameters: TE/TR/TA = 112 ms/5650 ms/2.04 min, FoV = 230x320 mm<sup>2</sup>, resolution = 0.7x0.7x3 mm<sup>3</sup> and GRAPPA with reduction factor =2.

## 5.3 Results

### 5.3.1 Measurement results

#### 5.3.1.1 Proton trap

The measured reflection and transmission S-parameter of one exemplary proton trap are depicted in Figure 5.2. For the transmission parameter, -0.8 dB at the sodium and -62.4 dB at the proton frequency were achieved. Reflection parameters of -39.2 dB at the proton frequency and -1.7 dB at the proton frequency were measured.

#### 5.3.1.2 Phantom

The SNR results of the phantom measurements are depicted in Figure 5.3. The top row shows the ratios (Rx array/Commercial) of the SNR maps in the center transversal slice. The profiles of the individual SNR maps in x-direction are given in the second row. The mean SNR ratio of the proton measurement was 1.14. The SNR of the commercial coil is higher in the neck region but in the center the SNR values are comparable. The SNR

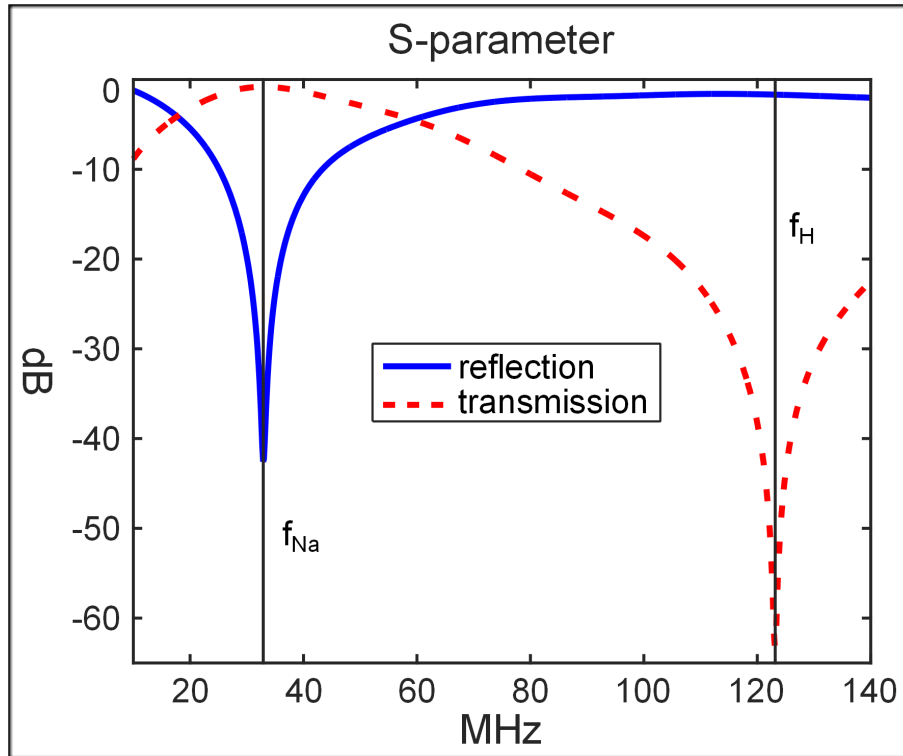


**Figure 5.2:** Measure  $S$ -parameter of the proton trap. The solid blue line indicates the reflection parameter and the dashed red line the transmission parameter.

maps of the sodium measurement show an increased SNR at the periphery of the phantom for the Rx array but SNR losses compared to the commercial coil in the middle of the phantom. The mean SNR ratio was calculated to 1.09.

The calculated  $g$ -factors for the proton coils are given in Figure 5.4.  $G$ -factors were computed for reduction factors ( $R$ ) of 2 and 3 in both phase encoding directions. Mean  $g$ -factors were for  $R = 2$  between -7% and +1% and for  $R = 3$  between -11% and +6% compared to the commercial coil. Maximum  $g$ -factors were found to be between -21% and +16% for  $R = 2$  and between +16% and +33% for  $R=3$  compared to the commercial coil. No  $g$ -factors were calculated for the sodium array since due to the low SNR commonly no acceleration is used.

### 5.3.1.3 *In-vivo*

The results of the *in-vivo* measurements acquired with the double resonant Rx array are shown in Figure 5.5. The same transversal slice is shown for all measurements. The images are given in arbitrary unit since a reduced noise scan was performed to decrease measurement time.

## 5.4 Discussion and conclusion

We developed a 16-channel double resonant Rx head coil for MRI at 3 T. The coil comprised 8 individual proton and sodium coils, respectively. The combined design of the DGB for the sodium array and the conventional overlap design for the proton array were chosen to facilitate the manufacturing process. The sodium array could be mounted on the coil support without readjusting the dimensions of the array. Decoupling could be

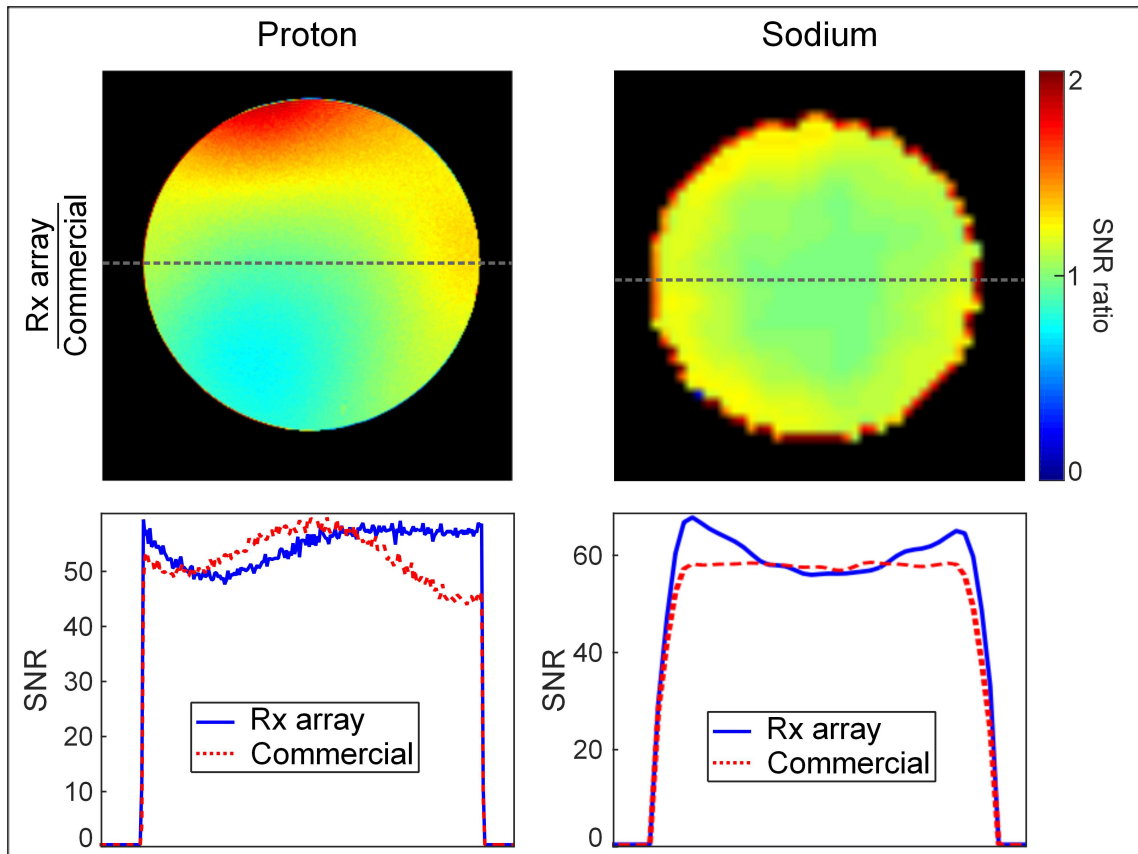


**Figure 5.3:** SNR ratios (Rx array/commercial) of the phantom measurements in the top row. Coil profiles in the x-direction in the middle of the phantom in the bottom row.

simply done using the decoupling capacitors in the DGB legs. This was of special benefit to re-adjust decoupling properties after the proton array was mounted on top of the sodium array. Any geometric changes of the sodium array would have been hard to realize since it was covered by the proton array.

Complete decoupling between non-adjacent elements cannot be achieved for a DGB (Cheng et al., 2003) but this is the same for the conventional overlap array. A possible effect on SNR due to this coupling was avoided by using the broadband matching approach (Brown et al., 2016a; Malzacher et al., 2018). This approach was chosen to avoid additional decoupling circuitry.

Many different designs have been proposed lately for double resonant coil setups. Most often, a nested design has been shown in which the higher frequency coils have been placed within the lower frequency coils (Brown et al., 2016a,b; Lakshmanan et al., 2018). These designs have been often realized as transceiver coils for both or at least one nucleus. We did not choose such a design since usually additional transformer decoupling is needed for the inner nested coils. Another point is that the preamplifier cannot be placed directly at the coil input due to the TxRx switch circuitry which can cause SNR losses. Additionally, due to the design of these setups, the B1+-homogeneity is usually restricted in z-direction compared to a large Body coil. A benefit of the transceiver design is that additional protection fuses are not needed which are necessary for commercial Rx only coils. Such a fuse will add resistance to the coil and decrease SNR in case of a coil

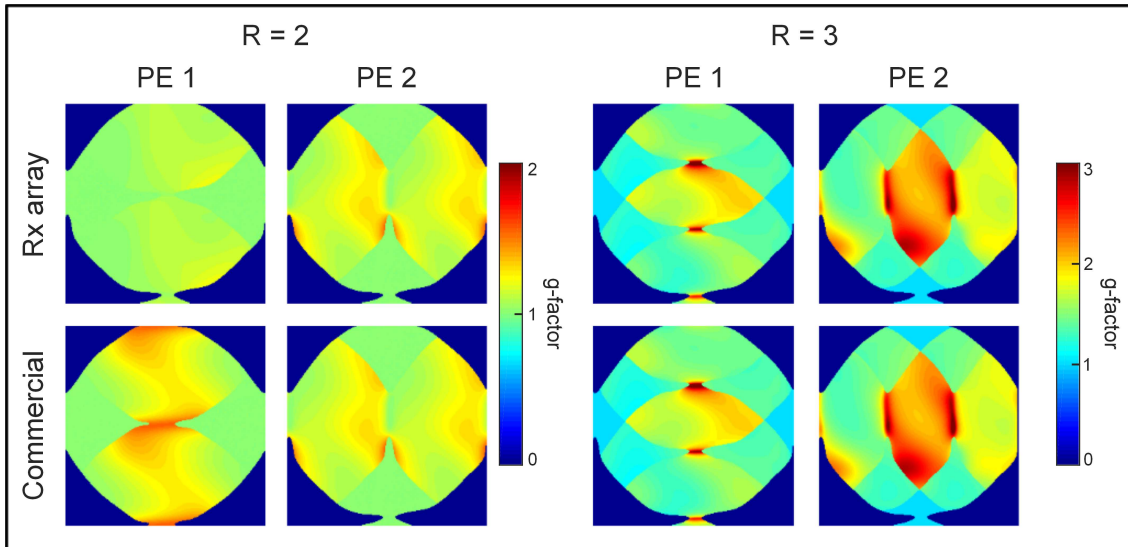


**Figure 5.4:** *G-factor maps for a reduction factor of 2 and 3 for the proton phantom measurements.*

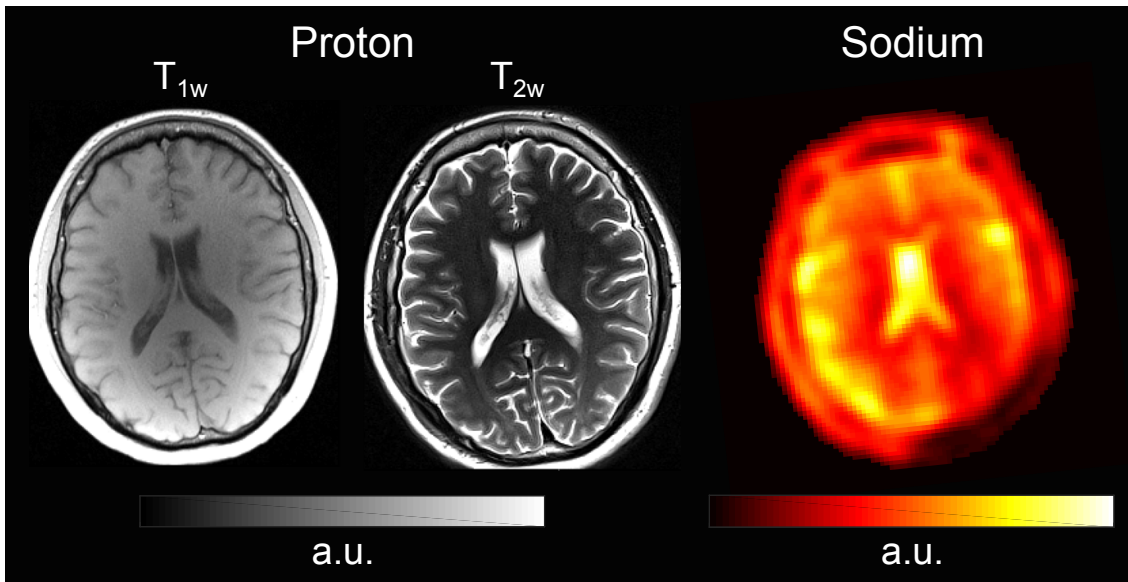


**Figure 5.5:** *In-vivo  $T_1$  and  $T_2$  weighted proton measurements and one sodium measurement.*

noise dominated setup. It was found for the nested transceiver setups that no additional trap circuits are needed depending on the distance of the two frequencies under investigation (Brown et al., 2016b). Such trap circuits are needed for the Rx coils of the lower frequency. Therefore, the two-staged trap design was selected which presents minimum insertion losses at the resonance frequency with the highest possible impedance at the trap frequency. Due to these traps, no additional proton cable traps were needed for the sodium Rx elements. Nevertheless, the losses of the traps added to the sodium Rx coils decreased the SNR in the center of the FoV compared to the commercial BC coil.

Finally, previously presented designs showed proton performance which was sufficient to obtain morphological image data. In contrast, the proton array presented here produced SNR and parallel imaging performance comparable to a commercial head array. Fuses were not added to our array which will decrease SNR performance to a certain extent.

Therefore, SNR and parallel imaging performance could be increased by using more lateral (Wiggins et al., 2009, 2006) or stacked (Chacon-Caldera et al., 2018, 2017; Ohliger and Sodickson, 2006b) elements.

In conclusion, we designed and implemented a double resonant Rx head coil comprised of 8 sodium and 8 proton channels for MRI at 3 T. The sodium SNR performance was comparable to the commercial solution as well as the proton performance in terms of SNR and parallel imaging performance. This combination of high sodium sensitivity and full proton imaging capability is believed to make an important contribution towards clinically used sodium MRI.

## **5.5 Statement of contribution**

In this study I was responsible for the study design. I built all measurement setups, acquired all measurement data and analyzed and evaluated the measurement data. I did the literature research and wrote the manuscript.





“Evaluating the effects of receive-only  
arrays in specific absorption rate simulations  
at 3 and 7 T” *Magn Reson Imaging*, DOI:  
*10.1016/j.mri.2018.06.011*

6

---

## 6.1 Introduction

The radio frequency (RF) power absorbed by the patient is a limiting factor for some magnetic resonance (MR) measurements since it can heat up the body tissue of the patient. The specific absorption rate (SAR) is used to maintain the RF power exposure of the human body within its regulatory limits. Extensive studies have been presented and are commonly performed to obtain detailed SAR information which is vital for patient protection and allows using the full potential of the MR scanner. However, only a few works have accounted for the effect of the receive (Rx) arrays in the SAR calculations and they have used very specialized setups or simplified detuning modeling of the Rx elements. In this work, we performed electromagnetic simulations using a clinical alike setup for whole-body scans at 3T and head scans at 7T.

Here, we consider a typical MR scanner setup which is comprised of a large volumetric transmission (Tx) coil surrounding the region-of-interest and purpose-built Rx arrays (Barberi et al., 2000). These have geometries adapted to closely fit the body part to be imaged. Such Rx arrays are also usually comprised of numerous single coil elements. These designs can increase Signal-to-Noise Ratio (SNR) and enable parallel imaging techniques (Ohliger and Sodickson, 2006a) to significantly reduce measurement time. Similar setups are used at higher field strengths. However, here (e.g. at 7T), the applications focus on smaller body structures like the head (Wiggins et al., 2006) or the knee (Chang et al., 2012) due to the reduced wavelength.

In a clinical MR measurement, SAR is determined globally based on the transmitting coil properties such as the accepted transmit power and the patient’s weight and approximate position. However, electromagnetic (EM) simulations are a powerful tool to assess additional key parameters for patient protection e.g. expected local SAR, mean SAR and SAR hotspots (maximum SAR).

Multiple SAR investigations have been performed in the past, for example, using detailed body models (Wolf et al., 2013), providing patient-specific models (Voigt et al., 2012) or defining ultimate intrinsic SAR for multiple parallel transmit coils (Guerin et al., 2014). Additional research has also been conducted to decrease SAR using hardware (Golestanirad et al., 2017; Kaneko et al., 2018) or pulse sequence approaches (Hennig et al., 2004; Okanovic et al., 2018). Moreover, clinical alike setups have been investigated at 1.5T (Wang et al., 2009), as well as experimental setups at 3T (Oh et al., 2010) and head

setups at 7T (Kozlov and Turner, 2010b; Krishnamurthy et al., 2014) and 9.4T (Avdievich et al., 2018).

During an MR scan, the single elements of the Rx arrays are detuned during RF pulse transmission i.e. they are made off-resonant. This is necessary to protect the patient and the Rx circuitry because an on-resonant Rx coil would distort the transmit field distribution and also absorb some of the transmitted power. In the few previous studies which included the Rx arrays, the modeling of the detuned coils has been done differently. More specifically, the Rx coils were, for example, modelled with gaps at the positions of capacitors in (Krishnamurthy et al., 2014) or as closed loops in (Golestanirad et al., 2017). Only very specialized works have attempted to match the properties of the detuned Rx coils to real Rx arrays (Avdievich et al., 2018; Kozlov and Turner, 2010b). Additionally, the outcome of these investigations have had a high variation yielding both increased (Krishnamurthy et al., 2014) and decreased (Golestanirad et al., 2017) SAR when taking Rx elements into account.

In this work, EM simulations are performed at the resonance frequency of  $^1\text{H}$  on a detailed human model using a clinical alike whole-body setup at 3T and a head setup at 7T. SAR simulations are performed for both setups with and without Rx arrays. Moreover, we investigate different human model positions and Rx array combinations using the 3T setup. Lastly, we adjust the detuning of the single coils of the Rx arrays in simulation following standard workbench methods used in the construction of Rx arrays.

## 6.2 Methods

### 6.2.1 Simulation and human model

#### 6.2.1.1 Simulation Setup

Full 3D EM simulations were performed using the frequency domain Finite-Element-Method (FEM) solver (CST Computer Simulation Technology GmbH, Darmstadt, Germany) with a tetrahedral mesh. The solver was set up with a frequency bandwidth of 20 MHz. At first, S-parameters were calculated at the resonance frequency and 10 frequency samples distributed equidistantly over the frequency bandwidth. Then, as many additional frequency points as necessary were calculated to get the maximum deviation of the linear S-parameters between two successive frequency points below 0.02. Initial global and local mesh properties were set manually concerning the complex simulation setup. Detailed information is provided in the following paragraphs. Mesh adaption was performed at the respective resonance frequencies (3T: 123.2 MHz, 7T: 297.15 MHz) for all S-parameters. Adaptive meshing stop criterion was set to an S-parameter magnitude difference of 0.05. The transmission coils were each driven with 2 ports (quadrature excitation). Matching and tuning of the transmission coils was done using the CST co-simulation (Kozlov and Turner, 2009).

#### 6.2.1.2 SAR calculation and scaling factor

SAR calculations were performed using

$$SAR = \frac{\sigma}{2\rho} \|E\|^2 \quad (6.1)$$

where  $\sigma$  is the material conductivity (S/m),  $\rho$  is the mass density of the material ( $\text{kg/m}^3$ ) and  $E$  is the magnitude of the E-field (V/m). 10g averaged SAR was calculated based on IEEE/IEC 62704-1 with 1W accepted power. In order to make the different SAR simulations comparable, different scaling factors were calculated. Thus, the power was calculated to produce a mean  $B_1^+$  field of  $11.7\mu\text{T}$  in different volumes. Different volumes were selected to take the transmit coil profile and possible influences of the Rx arrays on the  $B_1^+$  field into account. For 3T, the center plane (plane thickness 3 mm) and volumes with thicknesses in z-direction of 20, 40 and 60 cm were selected. For 7T the center plane (plane thickness 3 mm) and volumes in z-direction of 10, 20 and 30 cm were selected.

### **6.2.1.3 Human model**

The human model used was the CST Female Visible Human model “Nelly” which is based on the work of the National Library of Maryland’s research laboratory. This model is optimized for tetrahedral meshing. The model was cropped at the height of its armpits for the 7T simulations. The body tissue dielectric parameters for the different frequencies were provided by CST using the 4-Cole-Cole model (Gabriel, 1996).

### **6.2.1.4 Simulation positions**

In total, 3 different positions were simulated for the 3T setup and one position for the 7T setup (Figure 6.1).

Each setup was simulated with and without detuned Rx arrays. In the 3T simulations, the Rx array setup was changed depending on the position. The setups were chosen following standard clinical routine practices. Consequently, the spine array was included in all setups. The abdominal array was modelled as a flexible array and it was only used for the heart setup and abdomen setup. The head array was used in a full and a reduced configuration. A detailed description of the Rx arrays is given in the following paragraphs. The different positions were:

- a) 3T, abdomen setup, Rx arrays: head array (3T) reduced, spine array and two abdominal arrays
- b) 3T, head setup, Rx arrays: head array (3T) and spine array
- c) 3T, heart setup, Rx arrays: head array (3T) reduced, spine array and one abdominal array
- d) 7T, head centered, Rx array: head array (7T)

## **6.2.2 Whole-body setup at 3T**

### **6.2.2.1 Transmission coil**

A 32-legged high-pass Birdcage coil was designed with a diameter of 700 mm and a total length of 550 mm. The leg width was 38 mm and the end-ring width was 50 mm. Each end-ring was separated between each leg by a lumped element representing a capacitor. The coil was fed using two ports. Each port was added in series to one end-ring with  $90^\circ$  phase shift with respect to each other. The coil was pre-tuned using fixed lumped element capacitors. Fine tuning and matching was done using a co-simulation network comprised of lumped elements. A lumped element capacitor (5 nF) was added in series to each leg to emulate the PIN diodes be used to detune the coil. The transmission coil was surrounded by a shield modeled as a cuboid with a cylindrical cavity (diameter: 744 mm, length: 1600 mm). The initial background mesh was set to 30 cells per maximum wavelength

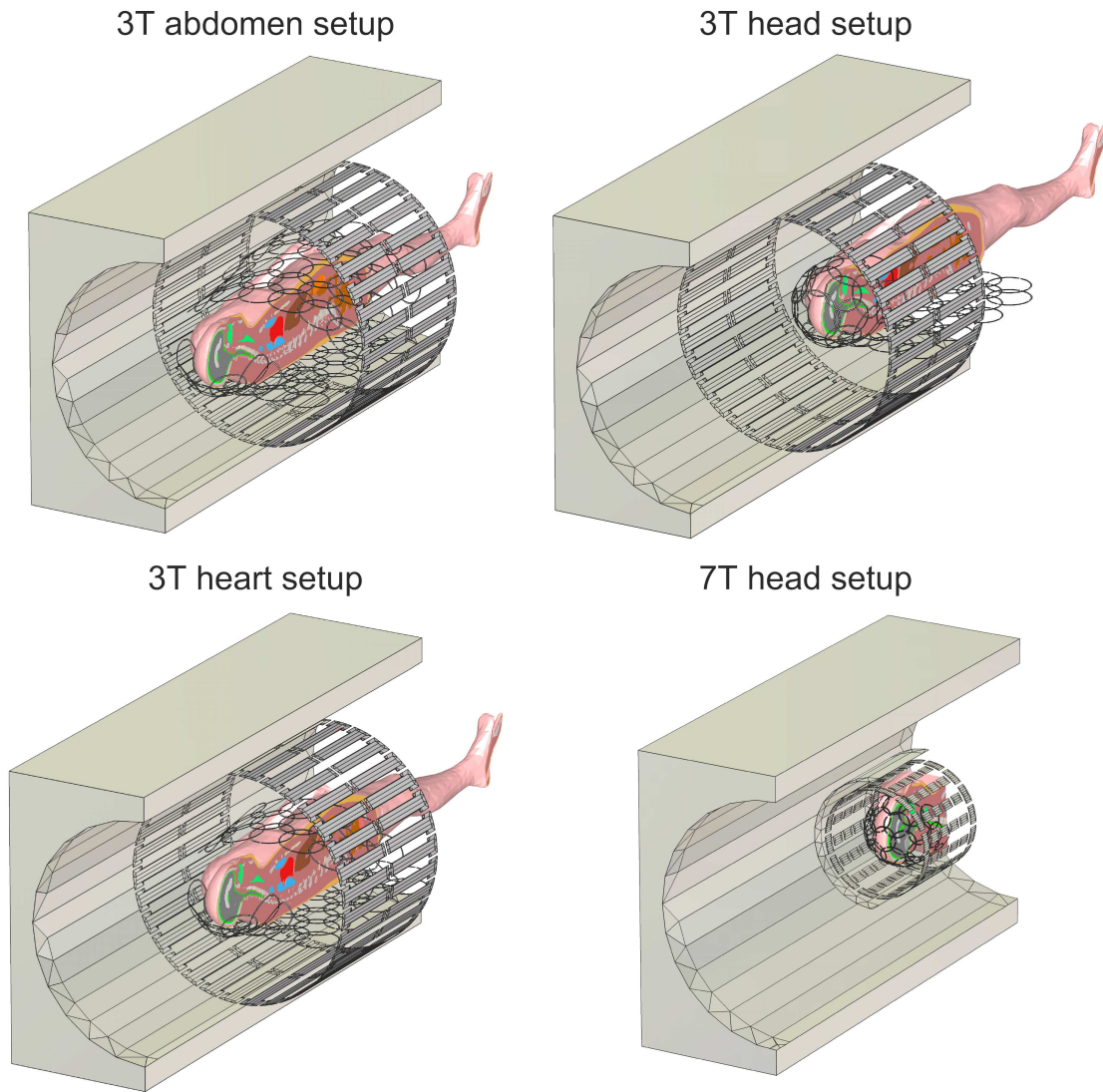


**Figure 6.1:** Simulation setups of the different 3 T setups and the 7 T setup. The shield and the human model were cut in coronal plane and all lumped elements and driving ports were hidden for imaging purposes.

( $\lambda_{@133.2MHz} = 2.25$  m, please note that the concerning frequency is 10MHz higher than the respective resonance frequency because of the selected bandwidth). The initial local mesh properties of the transmission coil were set to a maximum step width of 8 mm.

### 6.2.2.2 Receive arrays

Each coil of the arrays was split uniformly four times using three tuning capacitors and one detuning network. The detuning network is described in detail in paragraph 2.4. The individual coils were decoupled using overlap decoupling. The decoupling and the resonance frequency were adjusted iteratively. For this purpose the detuning network was replaced by a port.

#### Head array (3T)

A generic 24 channel head array was designed with an inner diameter of 244 mm and a length of 270 mm. The array was comprised of 4 rows (row 1: seven coils, row 2 and 3: eight coils, row 4: one coil). The head array was designed in a manner that it could also be split up in the middle as it is the case for most commercial head arrays. The reduced version of the head array was comprised of 10 elements in total. The conductors were arranged with a distance of 0.5 mm to each other. The diameters of the circular coils were 135.2 mm for row 1 and row 2 and 114 mm for row 3 and row 4. The conductor width was 3 mm for each coil. The conductor was modeled as flat perfectly electrical conductor (PEC) (Krishnamurthy et al., 2014). The same conductor dimensions were used for all Rx arrays.

### **Spine array**

A generic 32 channel spine array was designed with a width of 480 mm and a length of 736 mm. The single circular coils had a diameter of 134.8 mm. The spine array was comprised of 8 rows with 4 coils each row. The coils were arranged in the so-called “olympic” configuration.

### **Abdominal array**

A generic 18-channel abdominal array was designed with a width of 572 mm and a length of 304 mm. Since most of the abdominal arrays are designed as flexible arrays, the abdominal array was modeled so that it could be bent over the body of the human model. The abdominal array was comprised of 3 rows with 6 coils each. The single circular coils were built with a diameter of 132.5 mm. The coils were arranged in an “olympic” configuration.

## **6.2.3 Head setup at 3T**

### **6.2.3.1 Transmit coil**

A 16-leg band-bass Birdcage coil was designed with a diameter of 300 mm and a total length of 280 mm. The design of the coil was based on (Wiggins et al., 2006). The leg width was 25 mm and the end-ring width was 30 mm. Each end-ring was split with a lumped element capacitor between each leg and each leg was separated with 5 lumped element capacitors. The coil was fed using two ports. Each port was added in series to one end-ring with 90° phase shift with respect to each other. The coil was pre-tuned using the fixed lumped element capacitors. Fine tuning and matching was done using a co-simulation network comprised of different lumped elements. The coil was surrounded by a shield with a diameter of 354 mm and a length of 300 mm. An additional shield was added with a diameter of 682 mm and a length of 1300 mm to model the scanner surroundings. The initial background mesh was set to 30 cells per maximum wavelength ( $\lambda_{@307.15MHz} = 0.98$  m, please note that the concerning frequency is 10MHz higher than the respective resonance frequency because of the selected bandwidth). The initial local mesh properties of the transmission coil were set to a maximum step width of 6 mm.

### 6.2.3.2 Rx array

A 32-channel head array was designed with an inner diameter of 205 mm and a length of 200 mm. The array was comprised of 5 rows (row 1: six coils, row 2: nine coils, row 3: ten coils, row 4: six coils and row 5: one coil). The diameters of the circular coils were 72.3 mm. The conductors were arranged with a distance of 0.5 mm to each other. The setup of the coils and decoupling and tuning were adjusted as described in 6.2.2.2.

### 6.2.4 Detuning

The standard approach to detune the single Rx coils during the transmit phase in an MR measurement is to insert an “open” in at least one point of the coil. This is commonly achieved by adding an inductor in parallel to one tuning capacitor. The capacitor and the inductor form a circuit tuned to the Larmor frequency and therefore present a quasi “open” (high impedance) for the current in the coil. This inductor can be switched to the capacitor for example by a PIN diode which is synchronized with the Tx and Rx phases. This approach was replicated in our simulations. Additionally, since such a detuning network does in general not represent a perfect open, a resistor was added in parallel to the capacitor and inductor for the simulation. By changing the value of this resistor, the level of detuning could be adjusted. At the workbench the detuning can be adjusted by adjusting the resonance frequency of the LC circuit and measuring the response using a double pick-up loop (Darrasse and Kassab, 1993). Similarly, in order to adjust the level of detuning for the simulation setups, a double pick-up loop was modeled and the detuning was adjusted for each coil of the different Rx arrays. The detuning setup of one coil in the 24 channel head coil is depicted in Figure 6.2 on the left. An exemplary simulated and measured S12-parameter set is shown in Figure 6.2 on the right. The red lines show the S12-parameter in the resonant case and the blue lines the S12-parameter in the detuned case. The detuning level was adjusted to approximately 40 dB difference between the resonant and the detuned case at the respective resonance frequency (Barberi et al., 2000).

## 6.3 Results

### 6.3.1 E-field distribution

In Figure 6.3, middle sagittal slices of the combined E-fields normalized to 1 W accepted power are displayed.

This is done since induced currents on the Rx coils produce additional E-fields which modify the E-field distribution. A different E-field distribution caused by the Rx arrays will, consequently, change the SAR distribution in the human model following Eq. 6.1. The E-field results of the simulations including the detuned Rx arrays are shown in the first column and the E-field results without the Rx arrays are depicted in the second column. E-field hot spots at the conductor surfaces of the Rx array can be detected in all simulations including the Rx arrays. In addition, slight changes in the E-field distribution caused by the Rx arrays can be observed.

### 6.3.2 Local SAR distribution

Maximum intensity projections of the SAR ratio maps (SAR with Rx array / SAR without Rx array) are depicted in Figure 6.4. This is done to show the local variations in SAR

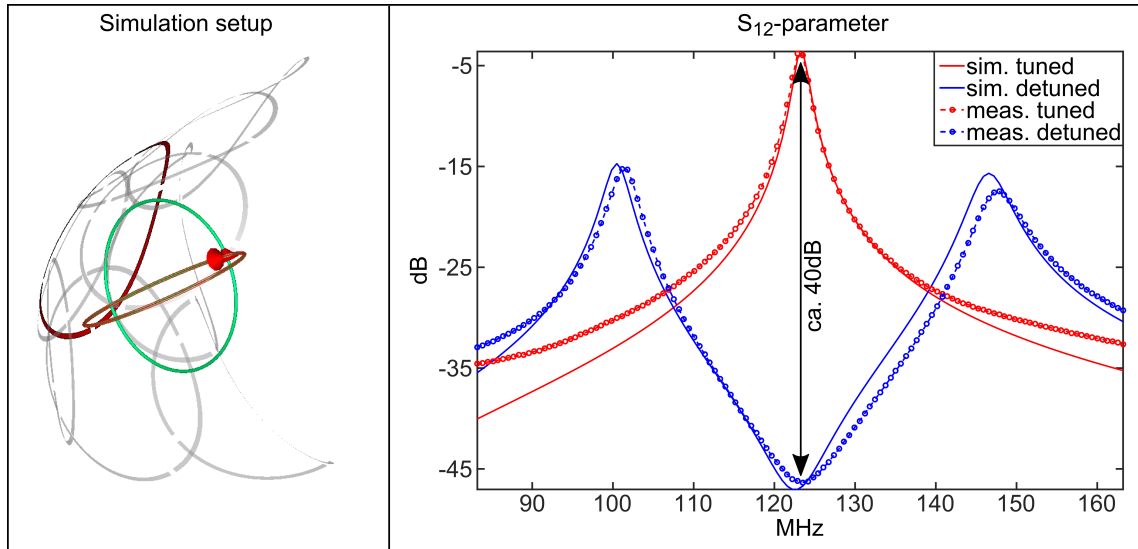


**Figure 6.2:** An exemplary simulation setup of the 24 channel Rx array for detuning process is shown on the left. The double pick-up loop is illustrated in green and the tested coil in red. Some surrounding coils of the array have been hidden for improved visibility. Exemplary simulated and measured  $S_{12}$ -parameters in dB acquired using a pair of decoupled pick-up loops. The  $S_{12}$ -parameters for the tuned case are shown in red and for the detuned case in blue.

distribution caused by the Rx arrays. The center planes of the transmit coils for all setups are indicated with a solid line. The respective volumes taken for the calculation of the scaling factors out of the  $B_1^+$  fields are marked with the dotted lines, the dashed lines and the dotted and dashed lines respectively.

Local SAR variations extend within 30% for all simulations within the imaging volume. Even higher ratios can be observed in the periphery of the human model. However, the absolute SAR values in these regions are comparably low.

### 6.3.3 Mean and maximum SAR values and $B_1^+$ field homogeneity

In Table 6.1,  $B_1^+$  field standard deviation ratios as well as SAR mean and maximum ratios are given. The standard deviation ratios were evaluated in the full volume, the center plane and three different reduced volumes. All 3T setups revealed a  $B_1^+$  field standard deviation ratio within 0% and 8% whereas the highest standard deviation differences were found in the head-centered setup. The 7T setup showed a 6% to 10% standard deviation difference.

Ratios of the mean SAR evaluated in the full simulation volume can be found in the second column. Mean SAR was evaluated using scaling factors using the mean  $B_1^+$  field determined in the full volume, the center plane and different reduced volumes. Mean SAR ratios remained in between 0% and 1% in case of the abdomen and heart setup at 3T. For the head setup the mean SAR was 2% higher for the simulations including the Rx arrays in case of the evaluation using the scaling factor acquired using the full volume. Using the scaling factor from the center plane or the reduced volumes mean SAR was between 2% and 4% higher for the simulations without the Rx arrays. The mean SAR for the 7T setup was between 6% and 11% lower for the simulations without the Rx array.

Scaling volume	$B_1^+$ field std. ratio [% difference]	SAR mean ratio in full volume [% difference]	SAR mean ratio in scaling volume [% difference]	SAR max ratio in full volume [% difference]
<i>Abdomen</i>				
Full volume	-0.16	+1.60	+1.60	-7.92
Center plane	-5.15	+0.43	-3.49	-8.98
Reduced 60 cm	-0.51	+0.50	-2.70	-8.92
Reduced 40 cm	-2.83	+0.23	-3.03	-9.16
Reduced 20 cm	-3.88	+0.31	-2.95	-9.09
<i>Head</i>				
Full volume	+2.54	+2.17	+2.17	+6.86
Center plane	+8.73	-3.52	-2.95	+0.90
Reduced 60 cm	+5.57	-1.92	-2.86	+2.57
Reduced 40 cm	+8.10	-1.74	-0.61	+2.77
Reduced 20 cm	+5.42	-2.61	-0.03	+1.85
<i>Heart</i>				
Full volume	-1.03	+1.03	+1.03	-8.04
Center plane	-4.28	+0.98	-2.41	-8.08
Reduced 60 cm	-1.59	+0.66	-1.79	-8.37
Reduced 40 cm	-3.72	+0.62	-2.05	-8.41
Reduced 20 cm	-3.73	+0.81	-2.23	-8.24
<i>7T</i>				
Full volume	+6.33	-5.07	-5.07	-2.48
Center plane	+9.12	-11.03	+3.70	-8.59
Reduced 30 cm	+8.57	-7.70	+0.10	-5.18
Reduced 20 cm	+9.60	-8.84	+2.64	-6.34
Reduced 10 cm	+10.36	-10.41	+4.16	-7.96

**Table 6.1:** Table 1 shows the percentage difference of the simulations with the Rx arrays compared to the simulations without the Rx arrays. The values of each setup are given for the tested scaling values which were calculated using the different scaling volumes. The values of the  $B_1^+$  field standard deviation are given in column 2, of the mean SAR evaluated in the full volume in column 3, of the mean SAR evaluated in the different scaling volumes in column 4 and the maximum SAR evaluated in the full volume in the last column.



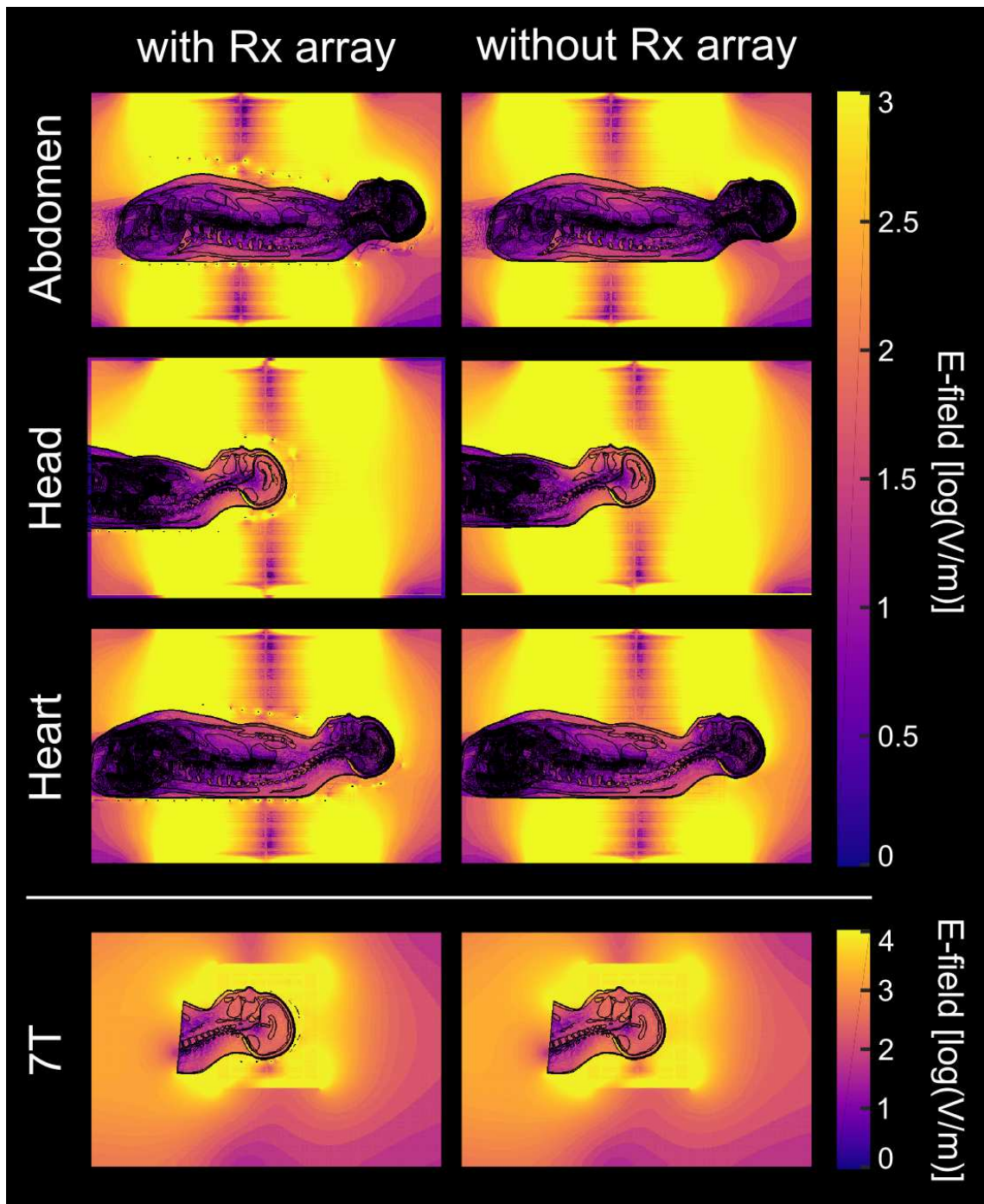


**Figure 6.3:** Middle sagittal slices of the simulated E-fields normalized to 1W accepted power. The simulations including Rx arrays are shown in the first column and the simulations excluding the Rx arrays are shown in the second column.

The third column of Table 6.1 shows mean SAR ratios in the volumes used to determine the scaling factors. For the 3T head setup the results stayed almost the same except for the evaluation in the center plane. The results for the other 3T setups, however, revealed an up to 3% lower mean SAR for the simulations including the Rx array for all evaluation volumes except the full volume. Mean SAR in the 7T simulations changed to an up to 4% higher mean SAR for the simulations including the Rx arrays by evaluating in the center plane and the reduced volumes.

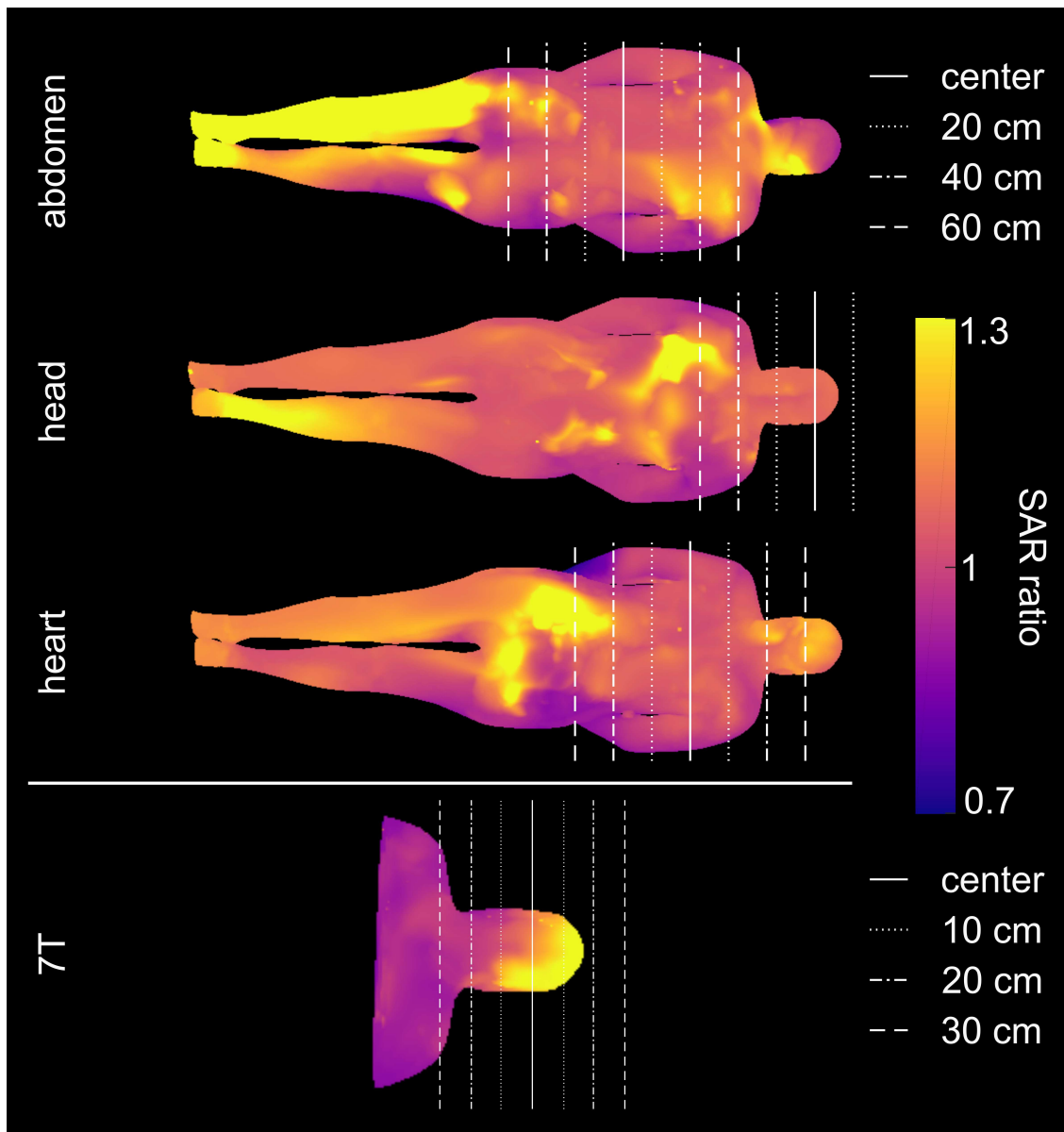


**Figure 6.4:** Maximum intensity projections of the SAR ratios (SAR with Rx arrays/SAR without SAR Rx arrays). The SAR was scaled using the scaling factor calculated out of the full simulation volume. The center position of the transmit coil is indicated with a solid line. The different scaling volumes for the 3 T and the 7 T setup are marked with the dotted lines, the dashed lines and the dotted and dashed lines respectively.

In the last column the maximum SAR ratios can be found. Maximum SAR was between 8% and 10% percent lower for the abdomen and heart setups including the Rx arrays but from 0% to 6% lower for the head setup simulations without the Rx arrays. In case of the 7T setup maximum SAR was between 3% and 9% lower for the simulation including the Rx array.

## 6.4 Discussion

In this work, the impact of detuned Rx arrays on SAR simulations was evaluated. In order to reflect the complex array setups of today's clinical MR systems, different Rx arrays

with numerous single coil elements were modelled. These arrays and a quadrature driven whole-body volume coil were created for EM simulations at the resonance frequency of 3T. As high field systems become more and more common, especially for head applications, a 7T head coil setup comprised of a quadrature driven head volume coil and a 32-channel head array was also simulated. Since the single coil elements of Rx arrays are detuned during transmit phase, a detuning network was added to the coils according to standard RF design procedures in coil building. Finally, full EM simulations were performed with and without the detuned Rx arrays and the results were compared.

The impact of the Rx arrays on the  $B_1^+$  fields was below 10% for all setups with regard to the difference in standard deviation of the fields. Since the detuning of Rx arrays is generally optimized for lowest disturbance of the transmit field such behavior was expected (Barberi et al., 2000).

There was no general trend found by adding the detuned Rx arrays to the simulation. However, high local alterations in SAR were found when the Rx arrays were added to the simulation. The local alterations may represent an elevated risk for the patients. For example, in the 7T case, the mean SAR was comparable in the whole volume.

For the evaluation and comparison of mean and maximum SAR values the different simulations were scaled to a certain mean  $B_1^+$  value. Different volumes were used for the scaling factors generation to take the coil profile of the volume coils into account. The total maximum difference for the mean SAR values for the different evaluation volumes and scaling volumes for the 3T setups remained within 8% and within 15% for the 7T setup.

Other publications investigating the impact of Rx array on the SAR distribution modelled the detuning of the coils of the Rx arrays as closed coils at 1.5T (Golestanirad et al., 2017) (all capacitor gaps were connected with conductors) or as open coils at 7T (Krishnamurthy et al., 2014) (all capacitor gaps were left open without connection of conductors or lumped elements). Both studies were performed with head coils only. In this work, we followed workbench methods used in coil construction to model the detuning state of the Rx coils as described in paragraph 2.4. Additionally, our simulations included 3 and 7T setups as well as different body regions. The study that used closed coil Rx arrays (Golestanirad et al., 2017) reported an overall reduction of mean (up to 70%) and max SAR (up to threefold) in all conditions. The investigations using the open coils (Krishnamurthy et al., 2014) found max SAR increase of 5% to 20% (mean SAR was not reported). Both studies showed strong effects on SAR by Rx arrays but always either an SAR increase or an SAR decrease. The variations in SAR induced by Rx arrays found in our study showed both an SAR increase and an SAR decrease.

One of the limitations of our study was that the simulated coils, arrays and the body model used were generic configurations which only reflect clinical setups to a certain extend. Additionally, components such as fuses, passive detuning circuits, circuit boards, preamplifiers and bunches of cables including cable traps were not included in the simulation. Further research needs to be performed in order to evaluate the effect of these components on SAR. Moreover, the impact on SAR distribution may differ by detuning the coils at multiple positions as is sometimes done for large Rx coils.

In conclusion, our results demonstrate that the inclusion of Rx array configurations in the SAR simulations changes the local SAR distribution especially at 7T. Nevertheless, considering the uncertainty of SAR calculations in general, case-by-case decisions could be made to decide whether the extra complexity of including Rx arrays into the simulations is worth it.

## **6.5 Statement of contribution**

In this study I was responsible for the study design, the generation of the simulation models, the data generation and the data analysis. I partially did the literature research and wrote the manuscript.

“A comparison of Time Domain and Frequency Domain methods for the simulation of RF systems for MRI applications at 3 to 11.7 T” *PLOS ONE*, submitted (25.07.2018)

7

---

## 7.1 Introduction

Rapid prototyping and safety assessment are important aspects in modern developments of radio frequency (RF) systems for magnetic resonance imaging (MRI) for proton and X-nuclei applications (Kozlov and Turner, 2009; Malzacher et al., 2016a; Shajan et al., 2016). The use of 3D electromagnetic (EM) simulations is therefore increasingly adopted to avoid the expensive manufacturing of multiple measurement setups and speed up the optimization process (Davidson, 2010). Additionally, such simulations can provide detailed insights into local specific absorption rate (SAR) distribution within a human body which cannot be measured *in-vivo* (Fiedler et al., 2018; Okanovic et al., 2018).

3D EM simulations are based on numerical solutions of Maxwell’s equations in a defined volume. Currently, mostly two solver types and mesh types are used (Rylander et al., 2012). These are the time domain (TD) solver, usually used with a hexahedral grid, and the frequency domain (FD) solver, usually used with a tetrahedral grid. Both methods are typically implemented in state of the art commercial software packages. Independently of the vendor’s individual implementation of the solvers, the main advantages and disadvantages of these solvers are determined by their mathematical bases. Thus, the selection of the solver of choice is strongly dependent on the analyzed RF structure and sample but also on the hardware available to compute the simulations. A well-considered selection of the solver type depending on the problem type can lead to efficient and accurate results. On the other hand, a bad solver choice can lead to slow and mistaken results. Additionally, not only the solver but also its parameters can greatly affect the results and performance. A comparison of these two methods for RF structures in MRI has been performed in two works for a specialized setup (Kozlov and Turner, 2010a; Martius et al., 2015).

In this work, we aim to provide a direct comparison between the TD and the FD solver using several state-of-the art RF setups at different field strengths. We adjusted the RF setups and the solver settings to achieve a good agreement of the S-parameter,  $B_1^+$ -fields and SAR distributions between the two solvers. Finally, we discuss the benefits

and possibilities of the two solvers depending on the RF setup and the magnetic field strength.

## 7.2 Background

### 7.2.1 Time Domain solver

Popular approaches for EM field simulations in the time domain are the Finite-Difference Time-Domain (FDTD) method (Yee, 1966) or the Finite Integration (FIT) method (Weiland, 1977) whereby the FDTD method discretizes the differential form and the FIT method the integral form of Maxwell's equations. The time evolution of the EM fields can be calculated by splitting the simulated volume up into a -most often- hexahedral grid with a second grid orthogonal to the first one. The two grids are shifted by half a cell size applied spatially ( $\Delta x$ ,  $\Delta y$ ,  $\Delta z$ ) and temporally ( $\Delta t$ ) and the H and E-fields are calculated each on a different grid. Since these solvers calculate the propagation of the fields through time in discrete temporal and spatial locations, the system has to be fed by at least one port. At the feeding ports, the fields can propagate into the structure and voltages and currents are monitored as input and output signals. Since the S-parameters are defined as the quotient of output and input signal spectrum, Discrete Fourier Transform of the signal spectra provides the full S-parameter set.

Straightforward gridding is one benefit of the hexahedral mesh used for the TD methods which allows generation of human voxel models relatively easily. A human model can be generated and modified by assigning material values to individual voxels. These models are fully compatible with the hexahedral mesh (Gosselin et al., 2014).

Nevertheless, there are certain drawbacks using a hexahedral mesh and a TD solver for MRI setups. One main problem, especially at lower fields ( $B_0 \leq 7T$ ), is the curvature and dimensions of the RF coils. Such structures need a very fine mesh to be accurately resolved (Figure 7.1). This can cause long computation times since the local fine mesh is extended over the whole simulation volume. At higher fields ( $B_0 \geq 7T$ ), for example microstrip transmission line (MTL) elements are more often used (Shajan et al., 2011). These elements usually have no bent structures and therefore they can be meshed more easily using a hexahedral grid.

Another point to consider is that the accuracy of the fields and S-parameter calculation depends on the steady state criterion. For the TD calculation, this is the amount of energy which remains in the simulation system when the calculation finishes. Highly resonating structures e.g. a Birdcage (Hayes et al., 1985) coil will extend the computation time required to reach a steady state criterion for high accuracy. However, using MTL like elements which are often made resonant only in co-simulations (Kozlov and Turner, 2009), a high accuracy can be reached in shorter time. The TD approach also becomes more efficient by simulating structures at higher frequencies. This is because the excitation bandwidth increases and therefore, the excitation pulse length decreases. Nevertheless, the frequency bandwidth should not be extended excessively over the frequency of interest since this will decrease the maximum wavelength. The maximum wavelength defines the spatial steps ( $\Delta x$ ,  $\Delta y$ ,  $\Delta z$ ) which influence the maximal stable time step  $\Delta t$  given by the Courant-Friedrichs-Levy-criterion:

$$\Delta t \leq \frac{\sqrt{\epsilon\mu}}{\sqrt{\left(\frac{1}{\Delta x}\right)^2 + \left(\frac{1}{\Delta y}\right)^2 + \left(\frac{1}{\Delta z}\right)^2}} \quad (7.1)$$

This means that a higher stop frequency causes a smaller time step and therefore to a longer computation time.

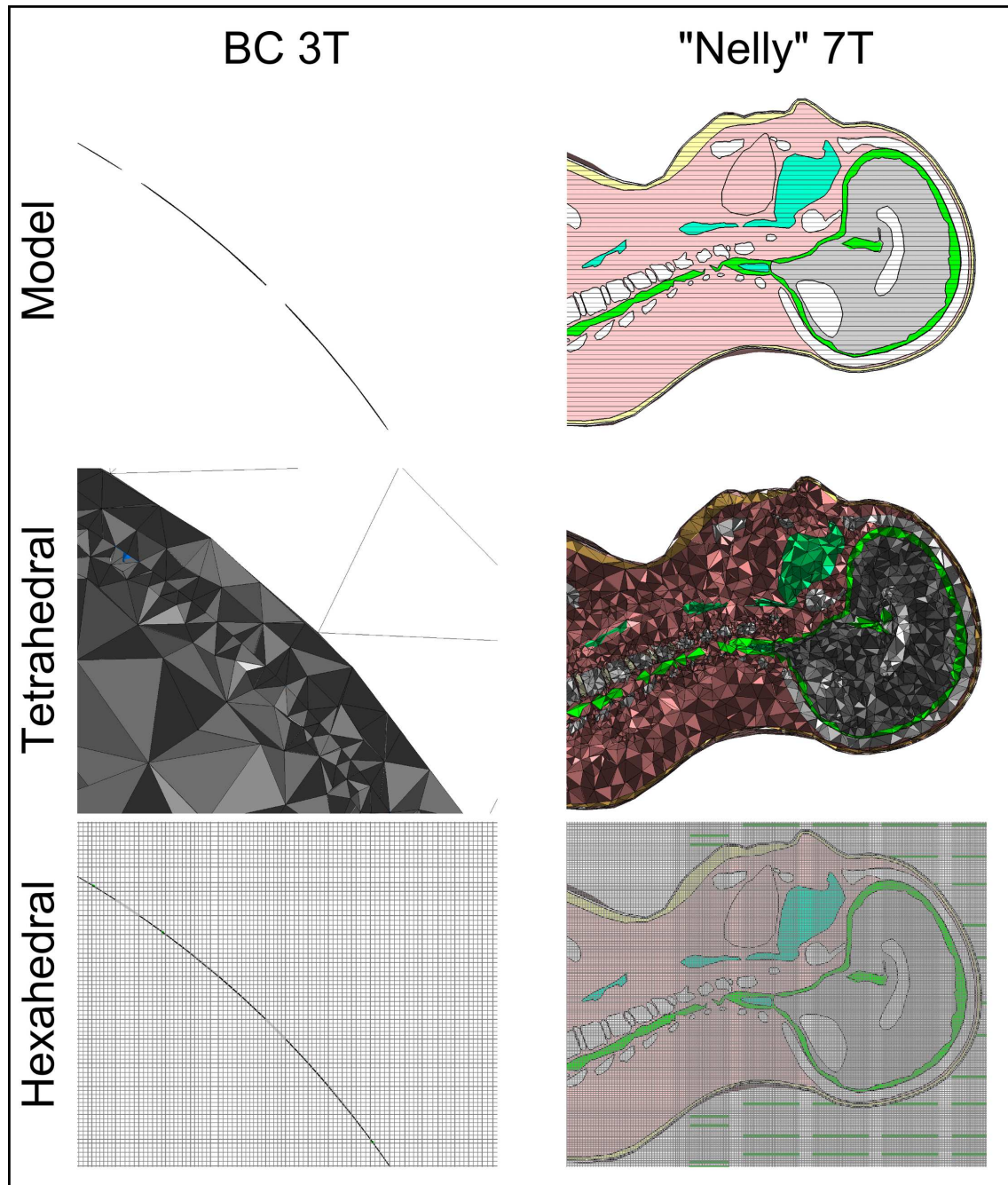


**Figure 7.1:** Left column: 3D model, tetrahedral mesh and hexahedral mesh of the Birdcage at 3T. A small part of the end-ring in an transversal slice. Right column: 3D model, tetrahedral mesh and hexahedral mesh of the “Nelly” head at 7T in the middle sagittal slice.

Finally, it has to be mentioned, that a large bandwidth may be only beneficial if there are no resonating modes below the resonance frequency of interest e.g. in a high-pass or

band-pass Birdcage. Such modes extend the time which the simulation takes to reach the steady state criterion since they can keep the energy in the system for longer. Therefore a compromise has to be found between achieving the steady state criterion and the selected bandwidth.

## **7.2.2 Frequency Domain solver**

Assuming a time-harmonic dependency of the EM fields, the equations to be solved can be transformed to the frequency domain. One approach to solve EM fields in the frequency domain is the Finite-Element-Method (FEM). Here, the simulation volume can be subdivided using a hexahedral mesh or other mesh types. One of the most often preferred mesh-type for these problems is the tetrahedral mesh. Using this method, the simulation volume can be split up into tetrahedral mesh cells of different size depending on the local complexity. This means for example that an accurate human model and a complex bent coil structure can be very finely resolved whereas large homogeneous structures can be comparably coarsely meshed (Figure 7.1). In order to get a broadband S-parameter set, multiple frequency sample points have to be simulated. The resulting S-parameters are interpolated from these points until the interpolation error goes below a selected accuracy criterion. One could only sample the frequency of interest but for the sake of accuracy and to ease a manual matching and tuning process using the co-simulation, a certain bandwidth should be simulated.

To ensure the accuracy of the mesh, the simulations are solved iteratively with a mesh more finely refined each time. After each simulation, the resulting S-parameters are compared until a prescribed accuracy criterion is met. In this way, accurate results will be obtained from the minimum number of cells required for the mesh adaptation to converge. Nevertheless, for complex simulation tasks, as it is the case most often in MRI simulations, the solutions are usually computed iteratively. In this case, a finer initial mesh may be considered to reduce the number of solver's iterations needed to reach the stop criterion for the residuum of the solver.

Compared to the time domain solver, the frequency approach can handle a highly resonant structure as efficiently as a non-resonant structure. One challenge of a tetrahedral mesh is the generation of human body models. Voxel models could be meshed using tetrahedrons but this may lead to a large number of mesh-cells which extends the simulation time.

## **7.3 Material and methods**

### **7.3.1 Simulation setup**

In this work, we used CST Microwave Studio (CST, Computer Simulation Technology GmbH, Darmstadt, Germany) to compute the simulations. This software package uses the FEM solver for FD and the FIT solver for TD simulations.

The simulations were performed on a server equipped with 2x Intel Xeon E5-2630v3 ( 8-Core, 2.40-3.20GHz) processors and 128GB DDR4-RAM.



### 7.3.2 RF structures and mesh settings

The different coil setups are depicted in Figure 7.2. All simulation setups were surrounded by a tube (3T: diameter 700 mm, length 1600 mm; 7-11.7T: diameter 682 mm, length 1300 mm) made of Perfect Electrical Conductor (PEC). This was done to mimic the gradient insert of a common MRI system. The broadband sweep stop criterion for all FD simulations was set to 0.02. Adaptive mesh refinement was performed at the respective resonance frequency. The steady state criterion for all TD simulations was set to -60dB.

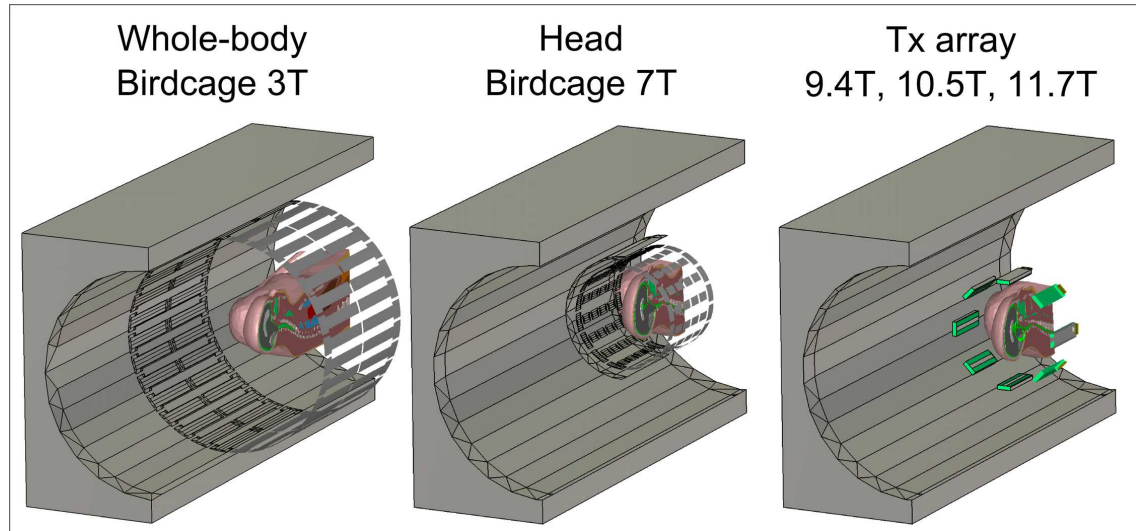


**Figure 7.2:** Simulation models of the different RF setups.

#### 7.3.2.1 3T whole-body Birdcage

A whole-body Birdcage coil with a diameter of 700mm and length of 550mm was modeled Figure (7.2). The coil was designed as a high-pass Birdcage with 32 legs (leg width 38 mm, end-ring width 50 mm) as previously shown in (Malzacher et al., 2018). Infinitely thin PEC was chosen as conductor. The coil was fed via two ports in series with the end-rings and with a phase shift of  $90^\circ$  to each other. The coil was pre-tuned using fixed lumped elements in the end-rings. Matching and tuning was done at the two ports using the co-simulation. The resonance frequency of the setup was 123.2 MHz.

For the FD simulation, the initial mesh of the coil structure was set to a maximum step width of 8 mm and the initial background mesh to 30 cells per maximum wavelength. The bandwidth of the simulation was 20 MHz.

For the TD simulation the coil mesh was set to 2 millimeters isotropic and the background mesh to 15 cells per wavelength. The bandwidth of the TD simulation was 40 MHz. We did not use a broadband bandwidth to exclude the lower modes of the Birdcage coil to decrease simulation time.

#### 7.3.2.2 7T head Birdcage

Based on (Wiggins et al., 2006), a 16-leg band-bass Birdcage coil was modeled (diameter 300 mm, length 280 mm). One capacitor was placed between each leg in the end-rings and five capacitors were placed in each leg (leg width 25 mm, end-ring width 30 mm). The coil was fed via two ports, one in each end-ring, with a  $90^\circ$  phase shift in respect to each other. The coil conductor was infinitely thin PEC. The conductor was replaced

by a faceted representation of the initial structure in order to enable the use of edge lumped elements and ports. Compared to the use of point lumped elements and ports the elements are connected via a edges of the tetrahedral mesh. Commonly, this increases the robustness of the mesh refinement for the FD solver. As for the 3T Birdcage the coil was pre-tuned using fixed lumped elements. Final tuning and matching was done at the ports using the co-simulation. The coil was additionally surrounded by a shield (diameter 354 mm, length 300 mm).

For the FD simulation, the initial mesh of the Birdcage coil was set to a maximum step width of 6 mm and the initial background mesh was set to 30 cells per maximum wavelength. The bandwidth of the simulation was 20 MHz.

For the TD simulation, the coil mesh was set to 1 millimeter isotropic and the background mesh to 15 cells per wavelength. The bandwidth of the TD simulation was 40 MHz. We did not use a broadband bandwidth to exclude the lower and upper modes of the band-pass Birdcage coil to decrease simulation time.

### **7.3.2.3 9.4 to 11.7T transmit array**

For the frequencies of 400 MHz (9.4T), 447 MHz (10.5T) and 498 MHz (11.7T) an 8 channel transmit (Tx) array was modeled. The inner diameter of this array was the same as of the head Birdcage coil (300 mm). Each element of the Tx array was a MTL element based on (Shajan et al., 2011). The ground-plane (width 42 mm, length 140 mm) was wrapped up (10 mm) on both sides of the dielectric (PTFE, width 42 mm, length 140 mm, height 12.5 mm). The MTL elements' conductors (width 12.5 mm, length 140 mm) were modeled with PEC. Each MTL element was electrically shortened using a capacitor at the front and the end of the element. These capacitors were also used to pre-tune the elements to their respective resonance frequency for the different field strengths. Each element was fed via two ports mounted on FR4 (width 30 mm, length 15 mm, height 5 mm). Tuning and matching was performed at these two ports using the co-simulation. Each element was matched and tuned individually with the other elements off-resonant. Afterwards the fields were combined in a circular polarized mode ( $0^\circ$ ,  $45^\circ$ ,  $90^\circ$ ,  $135^\circ$ ,  $180^\circ$ ,  $225^\circ$ ,  $270^\circ$ ,  $315^\circ$ ) with all elements resonant at the same time.

For the FD simulations the bandwidth was 40 MHz at their respective Larmor frequency. The initial background mesh was set to 10 cells per wavelength. The maximum step width was 2 mm for the ground-plane and the transmission line, 4 mm for the FR4 and 3 mm for the PTFE.

For the TD simulations the bandwidth was set from 0 to 420 MHz for the 9.4T simulation, from 0 to 467 MHz for the 10.5T simulation and from 0 to 518 MHz for the 11.7T simulation. The background mesh was set to 15 cells per wavelength. The mesh for the ground-plane, the transmission line, the FR4 and the PTFE were set to 1 mm isotropic.

### **7.3.3 Human model**

The human model used in this work was the “Nelly” Female Visible Human model from CST. This human model consists of 27 different body tissues. The model can be used for tetrahedral as well as hexahedral meshing. The tissue parameters for the different frequencies are calculated using the 4-Cole-Cole model (Gabriel, 1996). The human model was placed with the head in the center of the simulated volume in all simulations. is the model was cropped at the hips for the 3T simulation and at its armpits for the other

Ratio FD/TD mean	$B_1^+$ -field (1W acc.) [% difference]	SAR (10g avg. 1W acc.) [% difference]
3T	$-1.53 \pm 2.44$	$-0.59 \pm 7.28$
7T	$+2.16 \pm 16.28$	$+4.56 \pm 14.44$
9.4T	$+0.40 \pm 6.57$	$-2.83 \pm 6.78$
10.5T	$+1.58 \pm 6.83$	$+1.27 \pm 7.66$
11.7T	$+6.12 \pm 17.40$	$+7.67 \pm 13.85$

**Table 7.1:** Percentage differences of the mean ratios (FD/TD) of the  $B_1^+$ -fields and the SAR distributions.

simulations. A 2 mm isotropic mesh was used for the human model for all TD simulations. For the FD simulations, the initial mesh is not explicitly redefined.

The  $B_1^+$ -fields were calculated using:

$$B_1^+ = \frac{1}{2}(B_x + i \cdot B_y) \quad (7.2)$$

The SAR distributions were calculated using:

$$SAR = \frac{\sigma}{2\rho} ||E||^2 \quad (7.3)$$

Both, the  $B_1^+$ -fields and the SAR distribution were normalized to 1W accepted power.

## 7.4 Results

### 7.4.1 Coupling S-parameter

In Figure 7.3, ratios (FD / TD) of the linear coupling S-parameters are depicted for the different setups. The FD simulation yielded approximately 7% higher coupling compared to the TD simulation for the 3T setup. For the 7T setup, the difference was below 1%. The S-parameter ratios were between -22% and +9% for the 9.4T setup, between -7% and +14% for the 10.5T and between -14% and +9% for the 11.7T setup.

The center sagittal slices of the circular polarized  $B_1^+$ -fields of the different setups and different solvers are illustrated in Figure 7.4. The corresponding local SAR distributions are depicted in Figure 7.5. The solid white lines indicate the center of the coil setups. The dashed lines indicate the region of interest (ROI) in which the means and standard deviations of the  $B_1^+$ -field ratios and the local SAR ratios were calculated. The ratios (FD / TD) were calculated in the whole 3D ROI and are given in Table 7.1. The mean  $B_1^+$ -ratios were within -2% and +6% and the standard deviations were between 2% and 17%. The mean SAR ratios were between -3% and +8% with standard deviations between 6% and 14%.

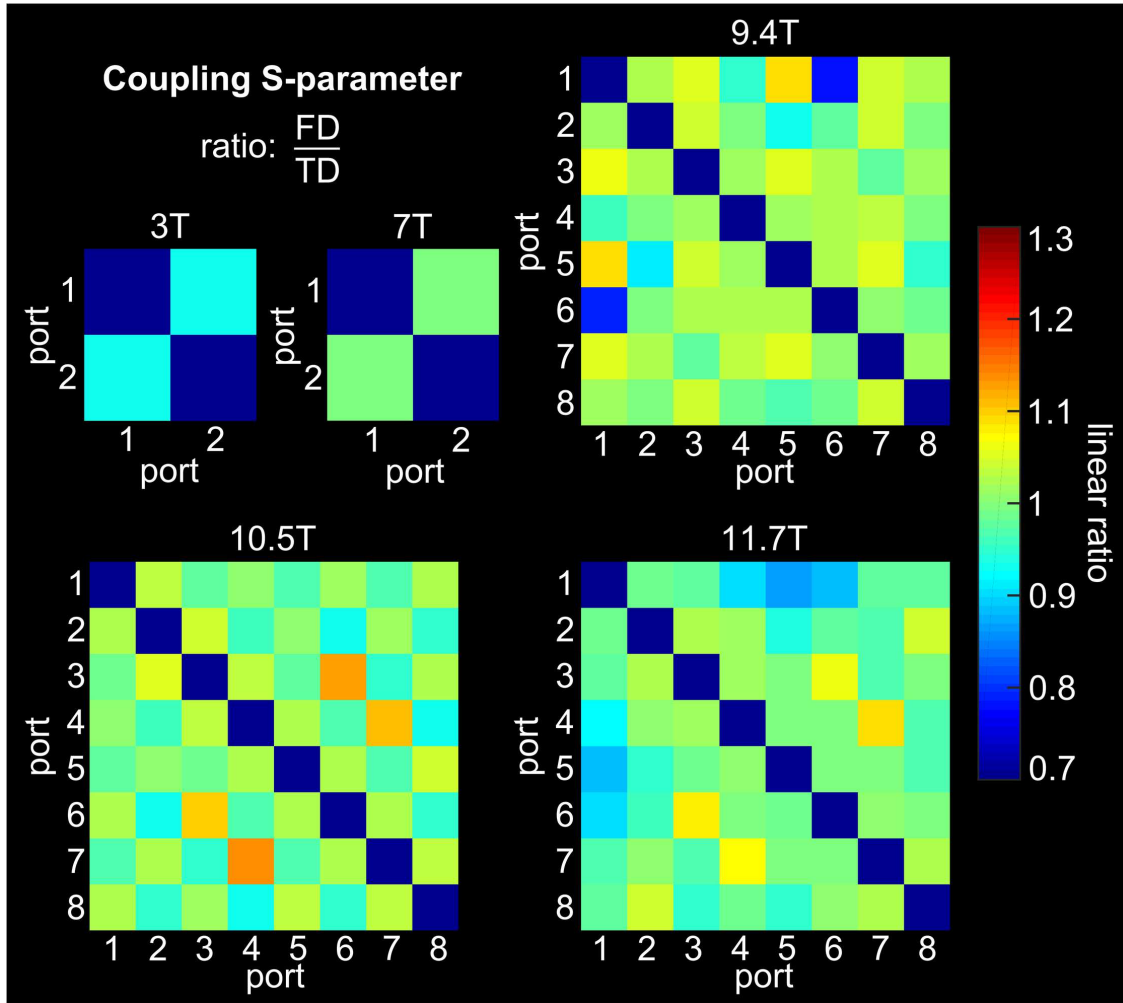


Figure 7.3: Coupling S-parameter ratios (FD/TD) for the different setups.

## 7.4.2 Mesh and solver performance

Key parameters in the evaluation regarding the mesh and the solver performance are summarized in Table 7.2. The adaptive mesh refinement for all FD simulations converged at least below 0.016 difference between subsequent simulations. The steady state criterion of -60dB was reached for all TD simulations. The total mesh cell number was between 20 and 120 times lower for the FD simulations compared to the respective TD. The largest difference was found in the 3T simulations since the total simulation volume is the largest for this setup. The total solver time of the TD simulations was between 4 and 12 time longer compared to their respective FD simulation.

## 7.5 Discussion

In this work, we performed a direct comparison of TD and FD approaches to calculate the EM fields for MRI RF applications. In order to cover a wide range of coil setups, we modeled volumetric Tx coils and Tx arrays for five different field strengths. Moreover, we

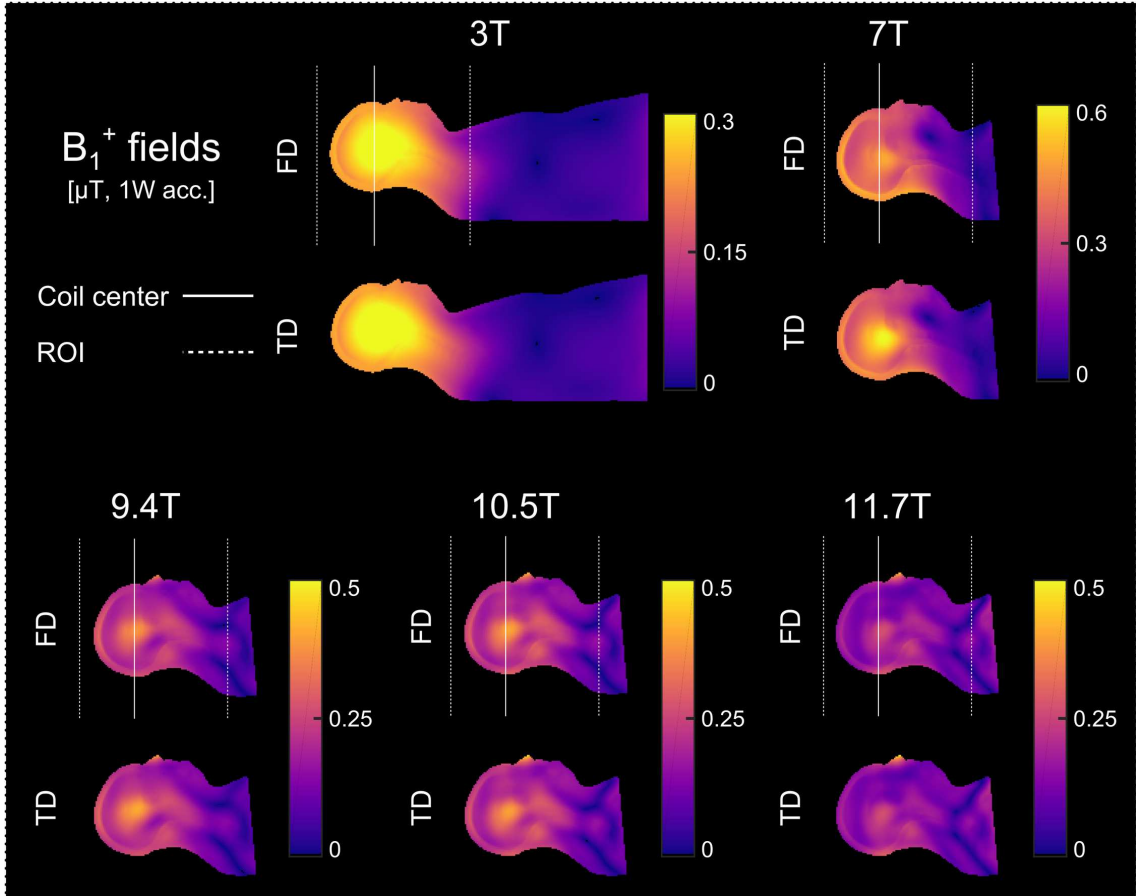


**Figure 7.4:**  $B_1^+$ -fields of the different setups in the middle sagittal slice. The white lines indicate the coil center and the dotted line indicate the region of interest for the calculation of the mean values.

investigated how much simulation cost is required for these two approaches to yield the comparable results. Our aim here was to reach a difference of results below 20% which has been found in a previous publication for one specialized setup (Kozlov and Turner, 2010a).

The first consideration is to select the most suitable solver to determine the problem type. Here, key parameters considered were the frequency of interest, the total simulation volume and the type of RF resonator. For all simulations the TD solver time is higher than the FD solver time. Nevertheless, we found that with higher frequencies and for non-resonant planar RF elements the total solver time of the TD solver decreases rapidly. The benefit of choosing a very large bandwidth and to have non-resonant structures improved the TD performance in terms of speed. However, the benefit of a large bandwidth vanished for resonant structures with multiple resonances below the frequency of interest as it is the case for common high-pass or band-pass Birdcages. Here, a compromise between reduced bandwidth and steady state criterion has to be found. Additionally, at comparably low frequencies, resonant and bent structures and a large simulation volume (as it is the case for most clinical systems) the FD solver clearly outperformed the TD in terms of total solver time.

Another consideration is the purpose of the simulation. For example, for the optimization of a complex, bent, multi-channel Rx coil, the FD domain solver seems to be the

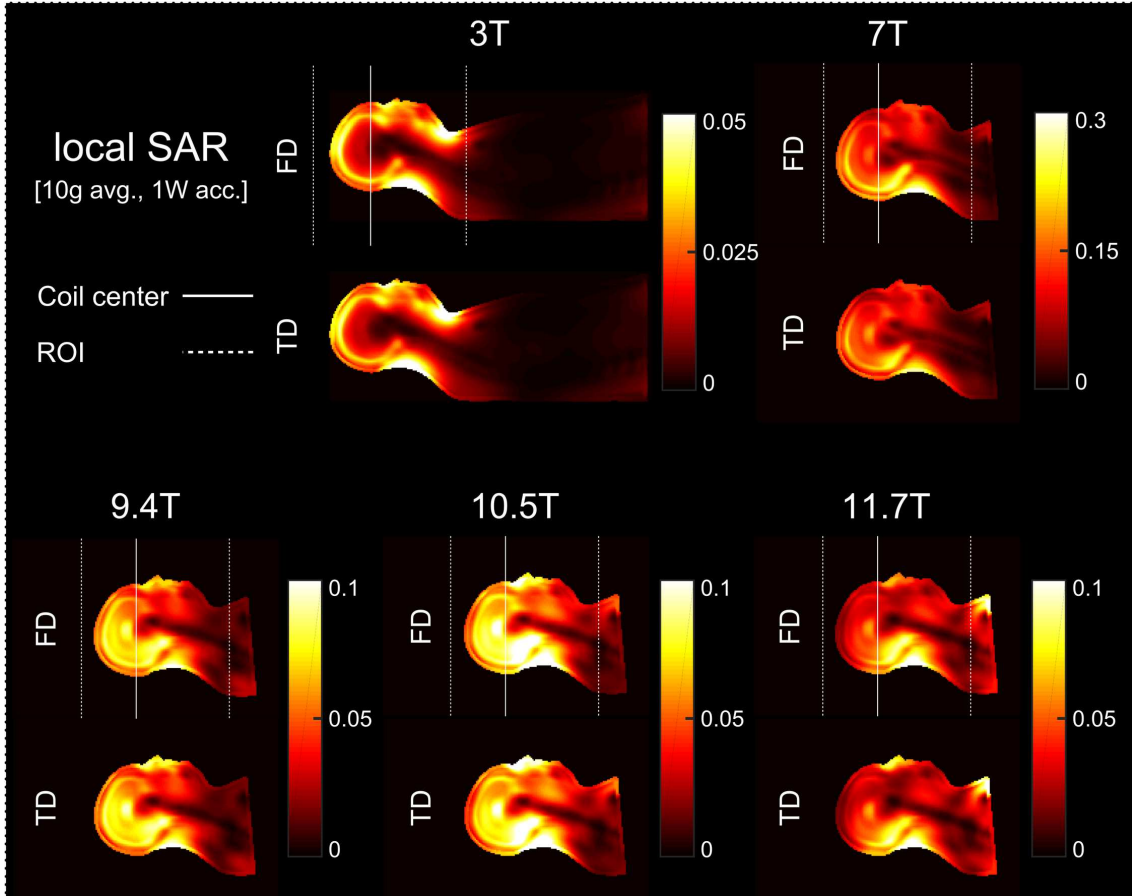


**Figure 7.5:** SAR maps of the different setups in the middle sagittal slice. The white lines indicate the coil center and the dotted line indicate the region of interest for the calculation of the mean values.

optimum choice since the optimization process usually aims to minimize the decoupling between the coils and maximize the  $B_1$ -field. Therefore, a homogenous phantom model could be sufficient for this purpose which can reduce the complexity of the simulation. For complex and fine RF structures, the tetrahedral mesh can be a better suit. Nevertheless, a human model is more appropriate if the SAR distribution of a Tx coil is being evaluated.

In terms of S-parameters, both solvers yielded comparable results. Especially for the 3T and 7T simulations, the coupling S-parameter differed below 7%. For the Tx array simulations, the difference between the simulations exceeded 20% for a single S-parameter. Nevertheless, the other S-parameters stayed below 20% difference.

Differences in coupling S-parameters may have an influence on the  $B_1^+$ -field magnitude since coupling describes the power exchange between the ports. However, the calculated  $B_1^+$ -fields reveal a low difference (below 7%) between the two solvers for the mean values in the selected ROI.

Different S-parameters may also yield different SAR distributions since the SAR is calculated from the E-fields in the human model (Equation 7.3). Here, we found a difference of SAR between the solvers below 8%. Therefore, although one S-parameter exceeded 20% difference between the solvers, the impact on the  $B_1^+$ -field and SAR distribution are

Simulation	Mesh cells	Adapt. mesh. refinement convergence	Total solver time	Steady state
3T FD	796 468	0.016	11 h	-
3T TD	97 308 120	-	135 h	-60 dB
7T FD	745 223	0.015	4 h	-
7T TD	51 807 060	-	31 h	-60 dB
9.4T FD	983 912	0.008	2 h	-
9.4T TD	21 608 640	-	18 h	-60 dB
10.5T FD	1 047 547	0.008	2 h	-
10.5T TD	22 638 000	-	14 h	-60 dB
11.7T FD	1 121 035	0.012	3 h	-
11.7T TD	23 123 520	-	17 h	-60 dB

**Table 7.2:** *Number of mesh-cells, adaptive mesh refinement convergence for the FD solver, total solver time and steady state criterion for the TD solver for all setups.*

minor.

In terms of SAR distribution the TD solver has the advantage that human voxel models can be produced more easily than surface models. In general, a surface human model can recreate complex human tissue structures better than a voxel model since it avoids partial volume effects which are unavoidable for the hexahedral mesh (Davids et al., 2017). This may be beneficial if, for example, the MR safety of small metallic implants has to be investigated. But if not many details are needed a voxel model can also be sufficient.

In either case, each solver can be optimized based on the choice or the availability of the simulation hardware due to the nature of the two different methods. On the one hand, the TD solver does not require much RAM but fast processors or graphic cards. Additionally, each port can be solved by an individual graphic card which would allow a simultaneous computation of all ports. Yet, this could be an expensive solution considering that some simulations could contain hundreds of ports. On the other hand, the need for RAM increases massively with the complexity and therefore, the number of mesh-cells of the simulation using the FD solver. Here, several fast processors will speed up the simulation but contrary to the TD solver, graphic cards cannot be used.

Finally, each RF setup may need different settings of the solver parameter to achieve the needed accuracy efficiently.

## 7.6 Conclusion

We showed that both approaches work and offer different advantages and disadvantages. However, each problem should be analyzed considering complexity, requirements of the sample, and available hardware. In either case, we expect our work to contribute to RF engineers in selecting the best fitting solver for each problem

## **7.7 Statement of contribution**

In this study I was responsible for the study design, the generation of the simulation models, the data generation and the data analysis. I did the literature research and wrote the manuscript.



# Summary 8

---

Optimized and problem tailored MR coil hardware can severely accelerate MR imaging and increase image quality for preclinical and clinical applications. Whereas vendors already offer high-end coil solutions dedicated RF setups optimized for specific problems can still increase imaging performance. Besides the performance optimization of MR coils, safety assessment is another very important point, which has to be addressed by vendors and researches. The limiting factor for Tx coils is expressed in the specific absorption rate, which is most often determined using complex EM simulations. The aim of this work was to develop optimized RF setups for preclinical and clinical X-nuclei MRI and to improve the accuracy of SAR calculations and EM simulations.

An issue which came up in recent years is SNR degradation due to coil coupling despite preamplifier coupling. This degradation only appears in certain circumstances, namely for coupled and low-loaded Rx coils. Therefore, it affects especially X-nuclei coils for small animal application due to the low frequency and low loading condition relative to the element size. This SNR degrading effect could be verified and overcome for a  $^{35}\text{Cl}$  application at 9.4 T, which increases imaging performance for this application.

Besides preclinical applications, X-nuclei MRI - especially sodium MRI - is of increasing interest for clinical applications. Main challenges for clinical sodium MRI are to overcome the low SNR and enable sodium and proton imaging using a single RF setup. Especially applications with large volumes of interest, as for example abdominal sodium MRI, suffer from low SNR. For abdominal applications the developed Rx array could enormously increase SNR compared to the volumetric transceiver coil. For head applications an RF setup was developed with high sodium SNR and proton performance comparable to commercially available coils.

Next to the optimization of the SNR performance of coils, safety assessment is a crucial point when developing Tx coils for clinical applications. EM simulations are widely used by vendors and researchers to determine detailed SAR distribution of a transmit setup. However, the impact of Rx arrays on this SAR distribution is rarely considered. Therefore a detailed investigation of a possible effect of Rx arrays included in the SAR simulations was performed for different clinical alike multi coil setups and one research setup. Differences between the simulation results with and without Rx arrays were found whereas the impact was larger for the high field research application.

EM simulations are not only used for safety assessment but also for rapid coil prototyping. There are different solver types and mesh types that can be used to solve the EM fields of a coil setup. Depending on the application it has to be carefully considered which solver should be used. Additionally, the adjustment of these solvers can strongly affect the accuracy and speed of these simulations. The comparison study presented here investigated different setups at different field strengths. Additionally, depending on the problem type advantages and disadvantages of solver type and solver settings were discussed.

A detailed summary of each scientific study (Chapter 3 through 7) is given in the following.

### **Reducing signal-to-noise ratio degradation due to coil coupling in a receiver array for $^{35}\text{Cl}$ MRI at 9.4 Tesla: A comparison of matching and decoupling strategies**

*Concept Magn Reson B, doi: 10.1002/cmr.b.21383*

In the third chapter, novel Rx coil matching methods have been evaluated based on theoretical considerations proposed in previous publications. Coupled Rx coils can experience SNR degradation despite preamplifier decoupling. The amount of SNR degradation depends on the loaded Q factor and the coupling factor. This means that a possible SNR degradation has to be detected for each individual coil setup. Next to a conventional decoupling method to mitigate this SNR degradation, there are two methods to avoid SNR degradation due to coil coupling. One is the broadband matching approach which was shown feasible in earlier works and another is the mode matching approach which was shown to be feasible for the first time in this work.

A complete RF setup was built for  $^{35}\text{Cl}$  MRI at 9.4T. The setup consisted of a volumetric Tx Birdcage coil and a 3 channel Rx array. The Rx array was comprised of 3 identical loop coils arranged around a tubular holder. The arrangement resulted in one coil which was decoupled from two coils via overlap and the two remaining coils facing each other. Therefore these coils were coupled with each other. Different phantom MRI measurements were performed using a 3D isotropic density adapted radial readout as follows:

- (1) Images were acquired using preamplifier decoupling for all coils.
- (2) The two coupled coils were decoupled using transformer decoupling. This was done by adding an additional loop to each coupled coil. These two loops were placed in front of each other to decouple the coupled coils.
- (3) The coupled coils were tuned and matched to one of the modes occurring due to coupling. The mode which was the most sensitive in the ROI was selected.
- (4) The coupled coils were matched in a broadband manner by coupling the preamplifier electrically tighter to the coil.
- (5) Images were acquired by the single Rx coils with the other coils detuned to evaluate the impact of SNR degradation.
- (6) Images were acquired using the volume coil without the Rx array present as a reference scan.

The preamplifier decoupled scan revealed severe SNR degradation for the coupled coils compared to the coils measured standalone. The transformer decoupled, the mode matched and the broadband matched measurement could recover lost SNR partially for the two coupled coils. This resulted in a 15%-17% higher combined SNR compared to the preamplifier decoupled measurement and an up to factor 4.5 higher SNR compared to the reference scan with the volumetric coil.

The two new matching approaches for mitigating SNR degradation due to coil coupling showed very promising results. The broadband matching approached worked especially well since it provided the same SNR as the conventional transformer decoupling approach. Additionally, this broadband approach is easier to implement and more appropriate for more complex Rx arrays compared to the transformer approach since no additional decoupling circuitry is needed. The mode matching approach was realized for measurement in this work for the first time to our knowledge. Although it performed not as well as the broadband approach, it is potentially promising for other Rx setups where the sensitive modes are more focused on the ROI.

The findings made in this work can substantially improve coil performance of complex Rx arrays for preclinical X-nuclei MRI. Even high density Rx arrays for clinical proton MRI could benefit of these methods depending on the design of the respective arrays.

### **Feasibility study of a double resonant ( $^1\text{H}/^{23}\text{Na}$ ) abdominal RF setup at 3T** *Z Med Phys, submitted (06.08.2018)*

In the fourth chapter, the feasibility of a double resonant sodium/proton RF setup for abdominal MRI at 3T was evaluated. The low MR sensitivity for sodium (approximately 10 000 times lower than for protons) is one main challenge of sodium MRI. The RF setup plays a key role in order to overcome this limitation. A common approach to increase receiver sensitivity is to combine small receiver coils placed in the immediate vicinity of the region of interest with volumetric transmission coils. Morphological proton images are still required to localize the physiological sodium information. The use of an additional proton coil to acquire these proton images without the need of replacing the RF setup minimizes patient discomfort and speeds up the imaging process.

In this study the feasibility of such a double resonant coil setup for abdominal MRI was evaluated. The setup comprised a 16 channel sodium receiver array, an asymmetric sodium Birdcage coil and a local proton transceiver coil. The sodium Birdcage coil was presented in another work before. The sodium Rx array consisted of a lower part and an upper part each with 8 individual Rx coils. Each Rx coil was equipped with a proton trap to minimize interaction with the proton coil and protect the Rx coils. The proton coil was realized as a Butterfly coil and mounted on top of the lower part of the sodium Rx array.

First, the complete setup was modeled for EM simulations. The dimensions of the sodium Birdcage were taken from the corresponding publication. The geometry and size of the sodium Rx coils were iteratively optimized for optimal overlap decoupling. EM simulations were performed with a phantom to evaluate the coil performance. For the safety assessment of the proton transceiver coils SAR simulations were conducted using a female and a male human model.

In order to realize MR measurements the 16 channel sodium array and the proton coil with an adequate housing were built. A power splitter and a proton TxRx (Stark Contrast GmbH) switch were used to enable sodium and proton MRI. Phantom measurements were conducted to compare the coil performance to the simulations. Finally, initial *in-vivo*

sodium and proton images of a healthy volunteer were acquired.

Both the phantom simulations and the measurements achieved a 3 to 6 fold sensitivity improvement of the sodium array compared to the volumetric coil. Peak SAR values were found to be 0.70 W/kg for the male model and 0.59 W/kg for the female model normalized to 1W accepted power. The feasibility of the whole setup was finally proven with an *in-vivo* sodium and proton scan acquired in one session without exchanging the coil setup.

The combination of a 16 channel sodium receive array combined with an asymmetric sodium Birdcage coil and an additional proton coil for sodium and proton MRI at 3T has been showed here for the first time to the best of our knowledge. The sodium receive array clearly outperformed the volumetric coil and therefore is believed to substantially enhance abdominal sodium MRI performance. Additionally, the inclusion of a local proton coil removed the necessity of co-registration and concurrently increased patient comfort.

### **Feasibility study of a double resonant $^1\text{H}/^{23}\text{Na}$ 16-channel receive-only head coil at 3T**

*Magn Reson Imaging, submitted (20.08.2018)*

In the fifth chapter, a feasibility study of a double resonant Rx head coil at 3 T is conducted. In order to enable sodium MRI in a clinical routine the RF setup has to fulfill several requirements. High sodium sensitivity is needed to overcome the low sodium SNR and reduce measurement time. Additionally, full proton performance including high sensitivity and parallel imaging compatibility is needed to acquire all clinically relevant contrast images. It should be possible to acquire sodium and proton images using the same RF setup in order to save measurement time and avoid coil exchange.

In this study a 16 channel sodium/proton Rx head array for MRI at 3T was realized for measurement. The coil comprised of an 8 channel Rx sodium degenerate Birdcage coil and an 8 channel proton Rx array. The sodium coils consisted of 8 individual Rx channels equipped with active detuning, sodium cable trap and sodium preamplifier. Additionally, a two staged proton trap was added to each leg and every second ring element of the degenerate Birdcage. This was done to minimize interactions of the sodium Rx array with the proton Rx array and to protect the sodium Rx coil during the proton transmit phase. The proton array consisted of 8 individual Rx coils which were decoupled by each other via overlap. Each coil was equipped with an active detuning circuit, a proton cable trap and a proton preamplifier.

First the array was designed using EM simulations. This was done to determine roughly the needed capacitor values and to obtain the geometry of the proton elements for optimum decoupling. Then the sodium array was mounted on a PVC tube with an outer diameter of 250 mm. Each element was initially tuned to the resonance frequency. The proton traps were added consecutively. The Rx elements were re-adjusted after each added proton trap. Decoupling was performed by adding decoupling capacitors in the shared legs of two neighboring coils. Decoupling was adjusted iteratively. Each proton Rx coil was built on an individual flexible FR4 board and added one after another on top of the sodium array.

Finally, MR measurements were performed using a bottle shaped phantom filled with saline solution. Proton transmission was done with the system's Bodycoil and sodium transmission with linear polarized Helmholtz coil. In order to compare the coil perfor-

mance with commercial coils phantom measurements were additionally performed with a sodium head Birdcage coil and a 12 channel proton Rx head array. Finally, initial proton and sodium measurements of a healthy volunteer were performed.

The SNR of the sodium array was comparable to the commercial sodium coil (mean ratio custom built/commercial = 1.14). Proton SNR of the Rx array was also comparable to the commercial solution (mean ratio custom built/commercial = 1.09) and mean g-factors were between -7% to +6% compared to the commercial solution. *In-vivo*  $T_1$  and  $T_2$  weighted proton measurements as well as sodium measurements finally proved the feasibility of such a setup.

### **Evaluating the effects of receive-only arrays in specific absorption rate simulations at 3 and 7 T**

*Magn Reson Imaging, doi: 10.1016/j.mri.2018.06.011*

The sixth chapter addresses one major safety aspect of MRI, namely the SAR distribution within the body. A conventional approach of determining the SAR properties of a Tx coil are the EM simulations. In this work the effect of including Rx arrays on the simulation of the SAR distribution of Tx coils was evaluated which has hardly been done in earlier publications. Therefore, a clinical alike volumetric whole-body Tx coil for 3T was modeled for simulation as well as a volumetric head coil for 7T. Additionally, clinical alike Rx arrays were modeled for 3T comprised of a 24 channel Rx head array, two 18 channel Rx abdomen arrays and a 32 channel Rx spine array. For 7T a 32 channel Rx head array was modeled. 3D EM simulations were performed using three different setups for the 3T coil (head centered, heart centered, abdomen centered) and one setup for the 7T coil. For the 3T setups, the different Rx arrays were composed as it is common in the clinical routine. Each setup was simulated with and without the Rx arrays present. In order to evaluate the impact of Rx arrays as realistically as possible, the detuning state of the individual coils of the Rx arrays were detuned using conventional workbench methods. Therefore a detuning circuit was added to each coil and the detuning state was adjusted for each coil of the arrays. The detuning was adjusted in a way as it was measured with a representing coil sample.

The SAR distributions were normalized to a  $B_1^+$ -field magnitude of 11.7  $\mu\text{T}$  to make a comparison possible. The  $B_1^+$ -field magnitude was evaluated in different volumes in order to take the coil profile of the Tx coils into account. Depending on the setup mean SAR difference was between -4% and 2% for the 3T simulations and up to 11% for the 7T simulation. Maximum SAR difference was found to be between -10% and +6% for the 3T setup and up to -8% for the 7T setup.

A detailed evaluation of the impact of Rx arrays on the simulated SAR distribution especially of clinical alike setups has not been performed elsewhere before to our knowledge. The difference in the local SAR distribution by running simulations with and without Rx arrays indicated that Rx arrays should not generally be excluded from SAR considerations. Nevertheless, whether Rx arrays should be included in the simulation may remain a case-by-case decision depending on the complexity of the simulation setup.

## **A comparison of Time Domain and Frequency Domain methods for the simulation of RF systems for MRI applications at 3 to 11.7 T**

*PLOS ONE, submitted (25.07.2018)*

In the seventh chapter, approaches for solving EM fields of RF setups for MRI applications are evaluated. EM solvers are widely used in the MR community for rapid prototyping and optimizing of complex RF setups as well as the consideration of safety issues. Currently, two methods are commonly used; namely the Time Domain (TD) and the Frequency Domain (FD). Both methods have different advantages and disadvantages concerning their solver and mesh properties. These properties are strongly dependent on the RF structure and its resonance frequency.

The TD method utilizes an orthogonal hexahedral grid to subdivide the simulation volume. Then, the time evolution of the EM fields, as well as the S-parameters are calculated by solving Maxwell's grid equations on the hexahedral mesh. The FD method mostly discretizes the simulation volume by using a tetrahedral mesh. Then the Maxwell equations are solved in the frequency domain using the variational method. The TD solver with the hexahedral mesh are best fitting for planar and non-resonant RF structures whereas the FD solver with the tetrahedral mesh is best suited for complex bent and resonant structures.

In order to evaluate benefits and drawbacks of these methods for different RF setups at different field strengths, multiple RF setups were modeled for simulation. These were a whole-body Birdcage for 3T, a head Birdcage for 7T and an 8 channel Tx array for 9.4T, 10.5T and 11.7T. The human model used was the CST "Nelly" model which is compatible with a hexahedral and a tetrahedral mesh. Each setup was simulated using both approaches. Afterwards the  $B_1^+$ -fields, the SAR distribution, the coupling S-parameters and the solver performance were compared.

Due to the different types of RF setups, the adjustments of the different solver and mesh settings were adapted for each setup. A difference below 20% between the solver approaches for the  $B_1^+$ -fields, the SAR distribution and the S-parameters were found. Nevertheless, the FD solver outperformed the TD solver in terms of total solver time in each case (FD solver up to 12 times faster).

A detailed comparison of the TD and FD method for clinical alike and research MRI RF setups has been performed in this expanse for the first time to our knowledge. Such a comparison has been previously done only for a specialized setup twice. The findings made here regarding the adjustments of the solvers in order to use the two solver approaches within certain deviation limits is expected to help RF engineers to select the best fitting solver approach and its adjustment settings for each type of RF structure for MRI applications.

## Outlook 9

---

MRI coils have rapidly evolved over the last years. High channel Rx arrays and efficient Tx coils are available on most clinical MR scanners of the latest generation. Nowadays most research in MR coils focuses on multi transmit arrays at field strengths higher than commonly applied in the clinic ( $\geq 7T$ ). However, there are still unsolved issues on conventional coil systems at lower frequencies.

The evaluated methods of mitigating SNR degradation due to coupled coils presented in the first scientific study (Chapter 3) are also applicable for clinical coils. Coupled and low loaded coils can be found for example in the upper part of head or knee arrays. The mode and broadband matching approach applied in this work could mitigate SNR penalty in such applications. Nevertheless, for the mode matching approach a possible resulting impact on parallel imaging performance should be taken into account. However, coil designs that aim for remotely mounted coils to increase patient comfort can greatly benefit from the methods shown. This could pave the way for 'one size fits all' RF coil systems in which the time-consuming positioning of coils on the patient is no longer necessary. In any case, these matching methods are well applicable for many X-nuclei coil designs.

Despite the strong evolution of sodium MRI in the last 30 years due to the use of sophisticated sequences, optimized post-processing and the availability of high field MR systems, a major obstacle for its application in the clinical routine has been the need for coils, which operate at a common clinical field strength of 3T. Therefore, the feasibility studies of the double resonant sodium and proton abdomen and head coil setups at 3T presented in the second and third scientific study (Chapters 4 and 5) make an important contribution towards clinically applied sodium MRI. Due to the high clinical interest in sodium applications in the head the developed head coil (Chapter 5) appears especially promising. Since the proton performance of this coil is comparable to commercial coils sodium images could possibly be acquired during waiting periods of normal clinical protocols, e.g. during contrast agent administration. Additionally, sodium and proton SNR and proton parallel imaging performance can be increased by employing sophisticated coil concepts, e.g. stacked coil elements.

Next to head applications, abdominal applications of sodium MRI are gaining more and more interest in clinical issues as well. Due to the large acquisition volume - compared to head applications - high SNR is even more relevant. Moving to high field strengths can be a solution for this problem but as shown in the second scientific study (Chapter 4) of this work a sophisticated coil design can also increase SNR enormously at clinical

field strengths. The performance of the implemented proton option, however, still needs to improve for clinical use. Future setups may comprise proton compatible sodium Tx coils without shield which allow the use of the MR system's proton Tx coil. Even a proton compatible transceiver sodium array would be conceivable whereby a large sodium Tx coil would no longer be necessary. Such a system would also be advantageous in terms of limited space inside an MR system. This gained space would offer more design possibilities for proton coils and thus the proton performance could also be increased. However, one drawback is the limited X-nuclei transmit power of the MR system which increases the transmit pulse length especially for large acquisition volumes. This increases the echo time which has a negative impact on sodium SNR due to the fast relaxation of the sodium nuclei. A higher transmit peak power could solve this problem but on the other hand may be limited by the SAR.

Besides peripheral nerve stimulation SAR is one of the main limiting factors in MRI. Since the findings of the fourth scientific study (Chapter 6) showed a relevant contribution of Rx arrays, when added to the SAR simulation setup, it should be considered for each specific setup. Furthermore, the detailed implementation of the detuning network for the Rx array elements opens up even more possibilities. Adjustments of the detuning properties, e.g. changes in the coupling level, can be used to decrease SAR by changing the Tx E-field distribution or to focus and to homogenize the Tx B-field. This might help to develop new Rx arrays which offer not only high SNR but also improve the performance of the Tx coils. Anyways, in order to be able to carry out such detailed and complex simulations at all, it is essential to be familiar with the solver and mesh type used and their settings. This is especially important in order to perform accurate SAR simulations.

Accurate simulation results and short simulation times can only be achieved by selecting the most suitability solver and mesh type for each problem. Not only selecting the best fitting solver type but also the right adjustment of the solver parameters is crucial. In the last scientific study (Chapter 7) presented in this work the most commonly used solver types for MR coils are compared for different coil setups and frequencies. Since the FD solver with the tetrahedral mesh outperformed the TD solver with the hexahedral mesh in terms of computation time the need for human models compatible with a tetrahedral mesh is obvious. Additionally, the integration of complex receive arrays into the EM simulation is only possible with a tetrahedral mesh since the amount of mesh cells using the hexahedral mesh would exceed common hardware requirements and reasonable computation times. Although the results of the two methods were in good agreement, future research should include the validation of the simulation results in comparison to measurement results.







## Bibliography

- Avdievich, N., Giapitzakis, I., Pfrommer, A., Borbath, T. and Henning, A. (2018). A Combination of surface and ‘vertical’ loop elements improves receive performance of a human head transceiver array at 9.4 T. *NMR Biomed* *31*, 3878.
- Baier, S., Krämer, P., Grudzenski, S., Fatar, M., Kirsch, S. and Schad, L. R. (2014). Chlorine and sodium chemical shift imaging during acute stroke in a rat model at 9.4 Tesla. *Magn Reson Mater Phy* *27*, 71–79.
- Barberi, E. A., Gati, J. S., Rutt, B. K. and Menon, R. S. (2000). A transmit-only/receive-only (TORO) RF system for high-field MRI/MRS applications. *Magn Reson Med* *43*, 284–289.
- Boada, F. E., Gillen, J. S., Shen, G. X., Chang, S. Y. and Thulborn, K. R. (1997). Fast three dimensional sodium imaging. *Magn Reson Med* *37*, 706–715.
- Bottomley, P. A. and Hardy, C. J. (1990). NMR probe with multiple isolated coplanar surface coils. US Patent 4,973,908.
- Brown, R., Lakshmanan, K., Madelin, G., Alon, L., Chang, G., Sodickson, D. K., Regatte, R. R. and Wiggins, G. C. (2016a). A flexible nested sodium and proton coil array with wideband matching for knee cartilage MRI at 3T. *Magn Reson Med* *76*, 1325–1334.
- Brown, R., Lakshmanan, K., Madelin, G. and Parasoglou, P. (2016b). A nested phosphorus and proton coil array for brain magnetic resonance imaging and spectroscopy. *Neuroimage* *124*, 602–611.
- Brown, R., Madelin, G., Lattanzi, R., Chang, G., Regatte, R. R., Sodickson, D. K. and Wiggins, G. C. (2013). Design of a nested eight-channel sodium and four-channel proton coil for 7T knee imaging. *Magn Reson Med* *70*, 259–268.
- Chacon-Caldera, J., Fischer, A., Malzacher, M., Vetter, Y., Davids, M., Flöser, M., Stumpf, C. and Schad, L. R. (2018). Evaluation of stacked resonators to enhance the performance of a surface receive-only array for prostate MRI at 3 Tesla. *Magn Reson Imaging* *53*, 164–172.
- Chacon-Caldera, J., Malzacher, M. and Schad, L. R. (2017). Partially orthogonal resonators for magnetic resonance imaging. *Sci Rep* *7*, 42347.
- Chang, G., Wiggins, G. C., Xia, D., Lattanzi, R., Madelin, G., Raya, J. G., Finnerty, M., Fujita, H., Recht, M. P. and Regatte, R. R. (2012). Comparison of a 28-channel receive

- array coil and quadrature volume coil for morphologic imaging and T2 mapping of knee cartilage at 7T. *J Magn Reson Im* 35, 441–448.
- Cheng, Y.-C., Eagan, T., Chmielewski, T., Flock, J., Kang, M.-C., Kidane, T., Shvartsman, S. M. and Brown, R. (2003). A degeneracy study in the circulant and bordered-circulant approach to birdcage and planar coils. *Magn Reson Mater Phy* 16, 103–111.
- Darrasse, L. and Kassab, G. (1993). Quick measurement of NMR-coil sensitivity with a dual-loop probe. *Rev Sci Instrum* 64, 1841–1844.
- Davids, M., Guérin, B., Malzacher, M., Schad, L. R. and Wald, L. L. (2017). Predicting Magnetostimulation Thresholds in the Peripheral Nervous System using Realistic Body Models. *Sci Rep* 7, 5316.
- Davidson, D. B. (2010). Computational electromagnetics for RF and microwave engineering. Cambridge University Press.
- Dorland, W. A. N. (1915). The American illustrated medical dictionary. Saunders.
- Fiedler, T. M., Ladd, M. E. and Bitz, A. K. (2018). SAR simulations & safety. *Neuroimage* 168, 33–58.
- Gabriel, C. (1996). Compilation of the dielectric properties of body tissues at RF and microwave frequencies. the U S Air Force Report *AFOSR-TR-96*.
- Golestanirad, L., Keil, B., Angelone, L. M., Bonmassar, G., Mareyam, A. and Wald, L. L. (2017). Feasibility of using linearly polarized rotating birdcage transmitters and close-fitting receive arrays in MRI to reduce SAR in the vicinity of deep brain simulation implants. *Magn Reson Med* 77, 1701–1712.
- Gosselin, M.-C., Neufeld, E., Moser, H., Huber, E., Farcito, S., Gerber, L., Jedensjoe, M., Hilber, I., Di Gennaro, F., Lloyd, B. et al. (2014). Development of a new generation of high-resolution anatomical models for medical device evaluation: the Virtual Population 3.0. *Phys Med Biol* 59, 5287.
- Guerin, B., Villena, J. F., Polimeridis, A. G., Adalsteinsson, E., Daniel, L., White, J. and Wald, L. L. (2014). The ultimate SNR and SAR in realistic body models. In *Proc Int Soc Magn Reson Med* vol. 22, p. 617,.
- Ha, S., Hamamura, M. J., Nalcioglu, O. and Muftuler, L. T. (2010). A PIN diode controlled dual-tuned MRI RF coil and phased array for multi nuclear imaging. *Phys Med Biol* 55, 2589.
- Han, S.-D., Heo, P., Kim, H.-J., Song, H., Kim, D., Seo, J.-H., Ryu, Y., Noh, Y. and Kim, K.-N. (2017). Double-layered dual-tuned RF coil using frequency-selectable PIN-diode control at 7-T MRI. *Concept Magn Reson B* 47, e21363.
- Hayes, C. E., Edelstein, W. A., Schenck, J. F., Mueller, O. M. and Eash, M. (1985). An efficient, highly homogeneous radiofrequency coil for whole-body NMR imaging at 1.5 T. *J Magn Reson* 63, 622–628.

- Hennig, J., Weigel, M. and Scheffler, K. (2004). Calculation of flip angles for echo trains with predefined amplitudes with the extended phase graph (EPG)-algorithm: principles and applications to hyperecho and TRAPS sequences. *Magn Reson Med* 51, 68–80.
- Hilal, S., Roschmann, P., Ra, J. B., Oh, C., Mun, I. and Einstein, S. (1988). Sodium imaging. *Magn Reson Med* , 715–731.
- Hoult, D. I. and Richards, R. (1976). The signal-to-noise ratio of the nuclear magnetic resonance experiment. *J Magn Reson* 24, 71–85.
- Hu, R., Neubauer, A., Malzacher, M., Konstandin, S. and Schad, L. (2017). Density-Adapted k-Space Sampling Technique for Fast Relaxing Chlorine-35 Nuclei at 9.4 Tesla. In *Proc Int Soc Magn Reson Med* vol. 25, p. 2949,.
- Jevtic, J. (2001). Ladder networks for capacitive decoupling in phased-array coils. In *Proc Int Soc Magn Reson Med* vol. 9, p. 17,.
- Kaneko, Y., Soutome, Y., Habara, H., Bito, Y. and Ochi, H. (2018). B1-control receive array coil (B-RAC) for reducing B1+ inhomogeneity in abdominal imaging at 3T-MRI. *J Magn Reson* 287, 25–32.
- Kirsch, S., Augath, M., Seiffge, D., Schilling, L. and Schad, L. R. (2010). In vivo chlorine-35, sodium-23 and proton magnetic resonance imaging of the rat brain. *NMR Biomed* 23, 592–600.
- Konstandin, S. (2012). Development of 2D radial techniques for sodium MRI with application to abdominal imaging at 3 tesla. PhD Thesis .
- Kozlov, M. and Turner, R. (2009). Fast MRI coil analysis based on 3-D electromagnetic and RF circuit co-simulation. *J Magn Reson* 200, 147–152.
- Kozlov, M. and Turner, R. (2010a). A comparison of Ansoft HFSS and CST microwave studio simulation software for multi-channel coil design and SAR estimation at 7T MRI. *Piers online* 6, 395–399.
- Kozlov, M. and Turner, R. (2010b). Comprehensive numerical study of 7T transmit-only, receive-only array coils. In *Proc Intl Soc Mag Reson Med* vol. 18, p. 1447,.
- Krishnamurthy, N., Zhao, T. and Ibrahim, T. (2014). Effects of receive-only inserts on specific absorption rate, B1+ field, and Tx coil performance. *J Magn Reson Im* 29, 475–484.
- l Mispelter, J., Lupu, M. and Briguet, A. (2006). NMR probeheads for biophysical and biomedical experiments: theoretical principles & practical guidelines. Imperial College Press.
- Lakshmanan, K., Brown, R., Madelin, G., Qian, Y., Boada, F. and Wiggins, G. C. (2018). An eight-channel sodium/proton coil for brain MRI at 3 T. *NMR Biomed* 31, e3867.
- Leussler, C., Stimma, J. and Röschmann, P. (1997). The bandpass birdcage resonator modified as a coil array for simultaneous MR acquisition. In *Proc Int Soc Magn Reson Med* vol. 5, p. 176,.

- Madelin, G., Lee, J.-S., Regatte, R. R. and Jerschow, A. (2014). Sodium MRI: methods and applications. *Prg Nucl Mag Res Sp* 79, 14–47.
- Madelin, G. and Regatte, R. R. (2013). Biomedical applications of sodium MRI in vivo. *J Magn Reson Imaging* 38, 511–529.
- Malzacher, M., Davids, M., Schad, L. R. and Chacon-Caldera, J. (2018). Evaluating the effects of receive-only arrays in specific absorption rate simulations at 3 and 7 T. *Magn Reson Imaging* 53, 7–13.
- Malzacher, M., Hu, R., Chacon-Caldera, J., Neubauer, A. and Schad, L. (2017). A  $^{35}\text{Cl}$  ToRo Resonator System for Preclinical MRI/MRS at 9.4T. In *Proc Int Soc Magn Reson Med* vol. 25, p. 5622,.
- Malzacher, M., Hu, R., Chacon-Caldera, J. and Schad, L. R. (2018). Reducing signal-to-noise ratio degradation due to coil coupling in a receiver array for  $^{35}\text{Cl}$  MRI at 9.4 T: A comparison of matching and decoupling strategies. *Concept Magn Reson B* , e21383.
- Malzacher, M., Kalayciyan, R., Konstandin, S., Haneder, S. and Schad, L. R. (2016a). Sodium-23 MRI of whole spine at 3 Tesla using a 5-channel receive-only phased-array and a whole-body transmit resonator. *Z Med Phys* 26, 95–100.
- Malzacher, M., Vester, M., Rhener, Robert, S., Christopher and Korf, P. (2016b). SNR simulations including coupled preamplifier noise. In *Proc Int Soc Magn Reson Med* vol. 24, p. 2157,.
- Martius, S., Schoepfer, J., Fackelmeier, A. and Huber, K. (2015). Comparison of different simulation methods regarding their feasibility for MRI coil design. In *Proc Int Soc Magn Reson Med* vol. 23, p. 3099,.
- Milford, D., Bendszus, M. and Heiland, S. (2018). A novel method for T2 quantification in presence of B1 inhomogeneities. *Z Med Phys* 28, 63–72.
- Nabeshima, T., Takahashi, T., Matsunaga, Y., Yamamoto, E. and Katakura, K. (1996). RF probe for MRI. US Patent 5,489,847.
- Nagel, A. M., Laun, F. B., Weber, M.-A., Matthies, C., Semmler, W. and Schad, L. R. (2009). Sodium MRI using a density-adapted 3D radial acquisition technique. *Magn Reson Med* 62, 1565–1573.
- Nagel, A. M., Lehmann-Horn, F., Weber, M.-A., Jurkat-Rott, K., Wolf, M. B., Radbruch, A., Umathum, R. and Semmler, W. (2014). In vivo  $^{35}\text{Cl}$  MR imaging in humans: a feasibility study. *Radiology* 271, 585–595.
- Neuberger, U., Kickingereder, P., Helluy, X., Fischer, M., Bendszus, M. and Heiland, S. (2017). Accuracy of  $^1\text{H}$  magnetic resonance spectroscopy for quantification of 2-hydroxyglutarate using linear combination and J-difference editing at 9.4 T. *Z Med Phys* 27, 300–309.
- Neumann, W., Lietzmann, F., Schad, L. R. and Zöllner, F. G. (2017). Design of a multimodal ( $^1\text{H}/^{23}\text{Na}$  MR/CT) anthropomorphic thorax phantom. *Z Med Phys* 27, 124–131.

- Niesporek, S. C., Hoffmann, S. H., Berger, M. C., Benkhedah, N., Kujawa, A., Bachert, P. and Nagel, A. M. (2015). Partial volume correction for in vivo  $^{23}\text{Na}$ -MRI data of the human brain. *Neuroimage* *112*, 353–363.
- Oh, S., Ryu, Y., Wang, Z., Robb, F. and Collins, C. (2010). Influence of a Receive-array Coil on Specific Absorption Rate at 3T: Simulations and Experiments with Basic Geometries. In *Proc Intl Soc Mag Reson Med* vol. 18, p. 1444.
- Ohliger, M. A. and Sodickson, D. K. (2006a). An introduction to coil array design for parallel MRI. *NMR Biomed* *19*, 300–315.
- Ohliger, M. A. and Sodickson, D. K. (2006b). An introduction to coil array design for parallel MRI. *NMR Biomed* *19*, 300–315.
- Okanovic, M., Volker, M., Trampel, R., Breuer, F., Jakob, P. and Blaimer, M. (2018). Increasing robustness of radial GRASE acquisition for SAR-reduced brain imaging. *Z Med Phys* .
- Ouwerkerk, R., Jacobs, M. A., Macura, K. J., Wolff, A. C., Stearns, V., Mezban, S. D., Khouri, N. F., Bluemke, D. A. and Bottomley, P. A. (2007). Elevated tissue sodium concentration in malignant breast lesions detected with non-invasive  $^{23}\text{Na}$  MRI. *Breast Cancer Res Tr* *106*, 151–160.
- Pipe, J. G., Zwart, N. R., Aboussouan, E. A., Robison, R. K., Devaraj, A. and Johnson, K. O. (2011). A new design and rationale for 3D orthogonally oversampled k-space trajectories. *Magn Reson Med* *66*, 1303–1311.
- Platt, T., Umatham, R., Fiedler, T. M., Nagel, A. M., Bitz, A. K., Maier, F., Bachert, P., Ladd, M. E., Wielpütz, M. O., Kauczor, H.-U. et al. (2018). In vivo self-gated  $^{23}\text{Na}$  MRI at 7 T using an oval-shaped body resonator. *Magn Reson Med* *80*, 1005–1019.
- Reykowski, A. (1998). Theory and design of synthesis array coils for magnetic resonance imaging. PhD Thesis .
- Reykowski, A. (2006). Receiver systems. Educational session, ISMRM .
- Roemer, P. B., Edelstein, W. A., Hayes, C. E., Souza, S. P. and Mueller, O. (1990). The NMR phased array. *Magn Reson Med* *16*, 192–225.
- Rylander, T., Ingelström, P. and Bondeson, A. (2012). Computational electromagnetics. Springer Science & Business Media.
- Schepkin, V. D., Chenevert, T. L., Kuszpit, K., Lee, K. C., Meyer, C. R., Johnson, T. D., Rehemtulla, A. and Ross, B. D. (2006). Sodium and proton diffusion MRI as biomarkers for early therapeutic response in subcutaneous tumors. *Magn Reson Med* *24*, 273–278.
- Schepkin, V. D., Elumalai, M., Kitchen, J. A., Qian, C., Gor'kov, P. L. and Brey, W. W. (2014). In vivo chlorine and sodium MRI of rat brain at 21.1 T. *Magn Reson Mater Phy* *27*, 63–70.
- Schepkin, V. D., Ross, B. D., Chenevert, T. L., Rehemtulla, A., Sharma, S., Kumar, M. and Stojanovska, J. (2005). Sodium magnetic resonance imaging of chemotherapeutic response in a rat glioma. *Magn Reson Med* *53*, 85–92.

- Schnell, W., Renz, W., Vester, M. and Ermert, H. (2000). Ultimate signal-to-noise-ratio of surface and body antennas for magnetic resonance imaging. *IEEE T Antenn Propag* 48, 418–428.
- Shajan, G., Hoffmann, J., Budde, J., Adriany, G., Ugurbil, K. and Pohmann, R. (2011). Design and evaluation of an RF front-end for 9.4 T human MRI. *Magn Reson Med* 66, 594–602.
- Shajan, G., Mirkes, C., Buckenmaier, K., Hoffmann, J., Pohmann, R. and Scheffler, K. (2016). Three-layered radio frequency coil arrangement for sodium MRI of the human brain at 9.4 Tesla. *Magn Reson Med* 75, 906–916.
- Silbernagl, S. and Despopoulos, A. (2007). *Taschenatlas Physiologie*. Georg Thieme Verlag.
- Sodickson, D. K., Zhang, B., Duan, Q., Brown, R., Lattanzi, R., Lakshmanan, K., Vaidya, M. V., Yang, A., Rehner, R., Vester, M. et al. (2014). Is a “one size fits all” many-element bore-lining remote body array feasible for routine imaging? In *Proc Int Soc Magn Reson Med* vol. 23, p. 618,.
- Streif, J. U., Lanz, T., Griswold, M., Rommel, E. and Haase, A. (2003). A coil combination for magnetic resonance perfusion imaging of mice in vivo at 7 T. *Rev Sci Instrum* 74, 2843–2848.
- Stumpf, C., Malzacher, M. and Schmidt, L.-P. (2018). Radio Frequency Modeling of Receive Coil Arrays for Magnetic Resonance Imaging. *J Imag* 4, 67.
- Thulborn, K. R., Davis, D., Adams, H., Gindin, T. and Zhou, J. (1999). Quantitative tissue sodium concentration mapping of the growth of focal cerebral tumors with sodium magnetic resonance imaging. *Magn Reson Med* 41, 351–359.
- Vester, M., Biber, S., Rehner, R., Wiggins, G., Brown, R. and Sodickson, D. (2012). Mitigation of inductive coupling in array coils by wideband port matching. In *Proc Int Soc Magn Reson Med* vol. 20, p. 2689,.
- Voigt, T., Homann, H., Katscher, U. and Doessel, O. (2012). Patient-individual local SAR determination: in vivo measurements and numerical validation. *Magn Reson Med* 68, 1117–1126.
- Wang, Z., Jin, J., Collins, C., Zhao, S., Oh, S., Yang, Q. and Robb, F. (2009). Numerical Investigation into Effects of a Receive Array on SAR in MRI. In *Proc Intl Soc Mag Reson Med* vol. 17, p. 3102,.
- Weiland, T. (1977). A discretization method for the solution of Maxwell’s equations for six-component fields. *Ele Com Eng* 31.
- Werbellow, L. G. (2007). Relaxation theory for quadrupolar nuclei. *eMagRes* .
- Wetterling, F., Corteville, D. M., Kalayciyan, R., Rennings, A., Konstandin, S., Nagel, A. M., Stark, H. and Schad, L. R. (2012). Whole body sodium MRI at 3T using an asymmetric birdcage resonator and short echo time sequence: first images of a male volunteer. *Phys Med Biol* 57, 4555.



- Wiggins, G., Wiggins, C., Potthast, A., Alagappan, V., Kraff, O., Reykowski, A. and Wald, L. (2006). A 32 channel receive-only head coil and detunable transmit birdcage coil for 7 Tesla brain imaging. In Proc Int Soc Magn Reson Med vol. 14, p. 415,.
- Wiggins, G. C., Brown, R. and Lakshmanan, K. (2016). High-performance radiofrequency coils for  $^{23}\text{Na}$  MRI: brain and musculoskeletal applications. *NMR Biomed* 29, 96–106.
- Wiggins, G. C., Brown, R., Zhang, B., Vester, M., Popescu, S., Rehner, R. and Sodickson, D. (2012). SNR Degradation in Receive Arrays Due to Preamplifier Noise Coupling and a Method for Mitigation. In Proc Int Soc Magn Reson Med vol. 20, p. 2689,.
- Wiggins, G. C., Polimeni, J. R., Potthast, A., Schmitt, M., Alagappan, V. and Wald, L. L. (2009). 96-Channel receive-only head coil for 3 Tesla: design optimization and evaluation. *Magn Reson Med* 62, 754–762.
- Wiggins, G. C., Triantafyllou, C., Potthast, A., Reykowski, A., Nittka, M. and Wald, L. (2006). 32-channel 3 Tesla receive-only phased-array head coil with soccer-ball element geometry. *Magn Reson Med* 56, 216–223.
- Wolf, S., Diehl, D., Gebhardt, M., Mallow, J. and Speck, O. (2013). SAR simulations for high-field MRI: how much detail, effort, and accuracy is needed? *Magn Reson Med* 69, 1157–1168.
- Yee, K. (1966). Numerical solution of initial boundary value problems involving Maxwell's equations in isotropic media. *IEEE T Antenn Propag* 14, 302–307.



# Publications

## Published Journal Papers

Reducing signal-to-noise ratio degradation due to coil coupling in a receiver array for 35Cl MRI at 9.4 Tesla: A comparison of matching and decoupling strategies **M. Malzacher**, R. Hu, J. Chacon-Caldera and L. Schad *Concept Magn Reson B*, in press (2018)

Evaluation of stacked resonators to enhance the performance of a surface receive-only array for prostate MRI at 3 Tesla J. Chacon-Caldera, A. Fischer, **M. Malzacher**, Y. Vetter, M. Davids, M. Floeser, C. Stumpf and L. R. Schad *Magn Reson Imaging*, 53, p. 164-172 (2018)

Evaluating the effects of receive-only arrays in specific absorption rate simulations at 3 and 7 T **M. Malzacher**, M. Davids, L. R. Schad, and J. Chacon-Caldera *Magn Reson Imaging*, 53, p. 7-13 (2018)

Radio Frequency Modeling of Receive Coil Arrays for Magnetic Resonance Imaging C. Stumpf, **M. Malzacher**, and L. Schmidt *J Imag*, 4(5), p. 67 (2018)

Partially orthogonal resonators for magnetic resonance imaging J. Chacon-Caldera, **M. Malzacher**, and L. Schad *Sci Rep*, 7, p. 42347 (2017)

Predicting Magnetostimulation Thresholds in the Peripheral Nervous System using Realistic Body Models M. Davids, B. Guerin, **M. Malzacher**, L. Schad, and L. Wald *Sci Rep*, 7, p. 5316 (2017)

Tracking protein function with sodium multi quantum spectroscopy in a 3D-tissue culture based on microcavity arrays A. Neubauer, C. Nies, V. Schepkin, R. Hu, **M. Malzacher**, J. Chacon-Caldera, D. Thiele, E. Gottwald, and L. Schad *Sci Rep*, 7, p. 3943 (2017)

Sodium-23 MRI of whole spine at 3 Tesla using a 5-channel receive-only phased-array and a whole-body transmit resonator **M. Malzacher**, R. Kalayciyan, S. Konstandin, S. Haneder and L. Schad *Z Med Phys*, 26(1), p.95-100 (2016)

## Conference Contributions

SAR Calculations in Transmit-Only-Receive-Only RF systems: A Comparison of Detuning Methods for Rx Array Coils and their Implementation in EM Simulations **M. Malzacher**, J. Chacon-Caldera, M. Davids and L. Schad *Proc. Int. Soc. Magn. Reson. Med., Paris, France, (2018) 26, p.640*

Feasibility Study of a Double Resonant ( $^{23}\text{Na}/^1\text{H}$ ) 8 Channel Rx Head Coil for MRI at 3T **M. Malzacher**, M. Davids, J. Chacon-Caldera and L. Schad *Proc. Int. Soc. Magn. Reson. Med., Paris, France, (2018) 26, p.142*

A double resonant ( $^1\text{H}/^{23}\text{Na}$ ) whole-body RF system for MRI at 3T **M. Malzacher**, N. Paschke, J. Chacon-Caldera and L. Schad *Proc. Int. Soc. Magn. Reson. Med., Paris, France, (2018) 26, p.1709*

Can sodium triple-quantum signal separate extra- and intracellular signals? investigation on HEP G2 liver cells, liposomes and nanoparticles M. Hoesl, D. Kleimaier, R. Hu, **M. Malzacher**, E. Gottwald, C. Nies and L. Schad *Proc. Int. Soc. Magn. Reson. Med., Paris, France, (2018) 26, p.3875*

Voxel localization for sodium NMR triple-quantum signal; sequence design and test in agarose phantoms and in-vivo rat M. Hoesl, D. Kleimaier, **M. Malzacher**, R. Hu, and L. Schad *Proc. Int. Soc. Magn. Reson. Med., Paris, France, (2018) 26, p.3874*

Simultaneously Acquired Single- and Triple-Quantum Spectroscopic Imaging with Density-Adapted Projection Reconstruction and Time Proportional Phase Increment R. Hu, **M. Malzacher**, M. Hoesl, D. Kleimaier, and L. Schad *Proc. Int. Soc. Magn. Reson. Med., Paris, France, (2018) 26, p.3866*

Measurement of oxygen consumption in a high density 3D cell culture on chip by  $^{19}\text{F}$  spectroscopy D. Kleimaier, M. Hoesl, A. Neubauer, **M. Malzacher**, C. Nies, E. Gottwald, and L. Schad *Proc. Int. Soc. Magn. Reson. Med., Paris, France, (2018) 26, p.3885*

Pushing Sodium Imaging Into Clinical Use - A Technical Feasibility Study **M. Malzacher**, J. Chacon-Caldera, A. Fischer and L. Schad *Proc. Int. Soc. Magn. Reson. Med., Honolulu, HI, USA, (2017) 25, p.2718*

A  $^{35}\text{Cl}$  ToRo Resonator System for Preclinical MRI/MRS at 9.4T **M. Malzacher**, R. Hu, J. Chacon-Caldera, A. Neubauer and L. Schad *Proc. Int. Soc. Magn. Reson. Med., Honolulu, HI, USA, (2017) 25, p.5622*

An SNR Optimized Quadrature Reception Posterior Array for Prostate Imaging at 3 Tesla J. Chacon-Caldera, A. Fischer, **M. Malzacher**, and L. Schad *Proc. Int. Soc. Magn. Reson. Med., Honolulu, HI, USA, (2017) 25, p.2670*

Exploring New Possibilities in Array Design Using Partially Orthogonal RF Resonators (Parti-Coils): A Numerical Simulation Study at 3 Tesla J. Chacon-Caldera, **M.**

**Malzacher**, A. Fischer, and L. Schad *Proc. Int. Soc. Magn. Reson. Med., Honolulu, HI, USA, (2017) 25, p.2705*

Spatial Resolution Analysis Comparing Density-Adapted and Conventional Projection Reconstruction in Chlorine-35 MRI at 9.4 T R. Hu, **M. Malzacher**, M. Davids, A. Neubauer, S. Konstandin, and L. Schad *Proc. Int. Soc. Magn. Reson. Med., Honolulu, HI, USA, (2017) 25, p.5219*

Density-Adapted K-Space Sampling Technique for Fast Relaxing Chlorine-35 Nuclei at 9.4 T R. Hu, A. Neubauer, **M. Malzacher**, S. Konstandin, and L. Schad *Proc. Int. Soc. Magn. Reson. Med., Honolulu, HI, USA, (2017) 25, p.2949*

Investigation of Strophanthin Induced Na-/K-ATPase Blockage by Means of  $^{23}\text{Na}$  Multi Quantum Spectroscopy in a High Density Cell Culture on Chip A. Neubauer, **M. Malzacher**, V. Schepkin, J. Chacon-Caldera, R. Hu, E. Gottwald, C. Nies, D. Thiele, and L. Schad *Proc. Int. Soc. Magn. Reson. Med., Honolulu, HI, USA, (2017) 25, p.5630*

SNR simulations including coupled preamplifier noise **M. Malzacher**, M. Vester, R. Rehner, C. Stumpf and P. Korf *Proc. Int. Soc. Magn. Reson. Med., Singapur, Singapur, (2016) 24, p.2157*

$^{23}\text{Na}/^1\text{H}$  In-Vivo Renal MRI of Rodent Kidney at 3T by Using a Double-Tuned Transceiver Resonator System R. Kalayciyan, **M. Malzacher**, S. Neudecker, N. Gretz, and L. Schad *Proc. Int. Soc. Magn. Reson. Med., Salt Lake City, USA, (2013) 21, p.4355*

$^{23}\text{Na}$  sodium MRI of whole-spine at 3 Tesla: Feasibility and first results **M. Malzacher**, R. Kalayciyan, D. Hausmann, S. Haneder, and L. Schad *Magn Reson Mater Phy, European Society for Magnetic Resonance in Medicine and Biology (ESMRMB), 29th Annual Meeting, Lisbon, Portugal, (2012) 25 (1), p.436*



# Curriculum Vitae

Name Matthias Malzacher  
Address Kleine Riedstraße 17  
68169 Mannheim  
Date of Birth 21.09.1987  
Place of birth Karlsruhe, Germany

## Education

---

- Since 2015 **Ruprecht-Karls-Universität Heidelberg**, Germany  
Doctoral candidate (Dr. sc. hum.)  
Computer Assisted Clinical Medicine  
Topic: Simulation and development of RF resonators  
for preclinical and clinical  $^1\text{H}$  and X-nuclei MRI  
Supervisor: Prof. Dr. rer. nat. Lothar R. Schad
- 2013 - 2015 **University Erlangen-Nuremberg**, Germany  
MSc biomedical engineering, GPA: 1.3 (1=best, 4=lowest)  
Masters Thesis: Validation of predictive SNR calculations  
by means of simulations and measurements of  
local coils for MRI
- MSc electrical engineering, GPA: 1.5 (1=best, 4=lowest)  
Masters Thesis: Validation of predictive SNR calculations  
by means of simulations and measurements of  
local coils for MRI
- 2010 - 2013 **University of Applied Science Mannheim**, Germany  
B.Sc. biomedical engineering GPA: 1.4 (1=best, 4=lowest)
- 2008 - 2010 **Heidelberg University**, Heidelberg, Germany  
aborted due to personal interests
- 2007 - 2008 **Mannheim University**, Mannheim, Germany  
aborted and proceeded at Heidelberg University
- 1998 - 2007 **Schönborn Gymnasium**, Bruchsal, Germany  
A-Levels, GPA: 1.9 (1 = best, 6 = lowest)

## Additional work experience

---

Summerterm     **University of Applied Science Mannheim**, Germany  
2018

Teaching assignment  
Course: Magnetic Resonance Imaging



## Acknowledgements

I thank all of my colleagues, my family and my friends, who supported me throughout the last three years of my PhD. Special thanks goes to:

Prof. Dr. Lothar Schad, who supported me for almost 6 years - with a short interruption for my master program - in any aspect and without any hesitation.

Dr. Jorge Chacon-Caldera for reading almost everything I ever wrote at CKM, for many insightful discussions about RF coils and "lasers", for risking his live as volunteer for my coils and for having sometimes one or more "Feierabendbier".

Sebastian Thomas for being the best office partner one could ever think of and for leaving everything immediately aside to answer me any question I had.

Dr. Jorge Chacon-Caldera, Sebastian Thomas, Simon Hubertus, Dr. Marco Bertleff, Nadia Paschke, Ruomin Hu, Tanja Uhrig and Dr. Mathias Davids for reading and correcting my dissertation.

Dr. Mathias Davids for many interesting discussions about EM simulations and the contact to the Boston group.

Dr. Nadja Meßner, Dr. Mathias Davids and Tanja Uhrig for the great teaching experience we had by giving the MRI lecture at the Hochschule Mannheim.

The whole CKM team the excellent working atmosphere, for all the friends I found there and the great parties in Singapore, Hawaii and Paris.

My roommates of the second floor of the CSH student residence hall where I spent two exciting years of my PhD time.

Last but not least, I thank my family who supported me throughout all my life and my girlfriend who supported me during my PhD.